

Ludwig-Maximilians-Universität München

PARTICLE ACCELERATION
IN
PULSAR WIND NEBULAE



Dissertation
an der Fakultät für Physik
der Ludwig-Maximilians-Universität
München

vorgelegt von
Christoph Nodes
aus Starnberg

München, 16. Dezember 2007

1. Gutachter: Prof. Dr. Harald Lesch
2. Gutachter: Prof. Dr. Hartmut Zohm

Tag der mündlichen Prüfung: 12.02.2008

Für meine Tochter Mathilda.

Zusammenfassung

Pulsar-Wind-Nebel oder Plerionen sind ausgedehnte astrophysikalische Objekte, die Synchrotron-Strahlung in weiten Bereichen des Spektrums abgeben. Sie werden von einer expandierenden Hülle begrenzt, die als Überrest einer vorangegangenen Supernova-Explosion verstanden werden kann. Im Inneren befindet sich ein aus relativistischem Plasma bestehender Nebel, der von einem schnell rotierenden Neutronenstern, einem zentralen Pulsar, energetisch versorgt wird. Dieser gibt enorme Mengen an Energie in Form von starken Plasmawinden ab, die Poynting-Fluss und hochrelativistische Teilchen nach außen transportieren. In einer Schicht, in der der Plasmawind auf das umgebende Medium des Nebels trifft, bildet sich eine stehende Schockfront, an der die radial gerichtete Plasmabewegung aufgelöst wird. Diese Schockfront ist Schauplatz gewaltiger energetischer Ausbrüche, welche als zeitlich veränderliche filament-artige Strukturen beobachtet werden. Als Erklärung hierfür werden hochrelativistische Teilchen herangezogen, die sich entlang magnetischer Strukturen bewegen und dabei Synchrotron-Strahlung abgeben. Die Schockfront grenzt den Plasmawind des Pulsars vom umgebenden Nebel ab. Plerionen zeigen ein erstaunlich flaches Synchrotron-Spektrum im Radio-Bereich, das einen Spektralindex zwischen $\alpha = 0.0$ und $\alpha = -0.3$ aufweist. Bisherige, auf diffusive Fermi-Beschleunigung der Elektronen beruhende Modelle sagen Potenzgesetze der Art $N(\gamma) \sim \gamma^{-s}$ mit einem Spektralindex $s = 2$ für deren Energiespektren voraus. Elektronenpopulationen mit solchen Energiespektren produzieren unter vereinfachten Annahmen ein Synchrotron-Spektrum, das einem Potenzgesetz mit einem Spektralindex $\alpha = (s - 1)/2 = 0.5$ folgt. Somit reichen diese Modelle alleine nicht aus, um die flachen Synchrotron-Spektren von Plerionen zu erklären und es müssen zusätzliche alternative physikalische Prozesse für die Beschleunigung der Elektronen verantwortlich sein.

Die vorliegende Arbeit behandelt die magnetohydrodynamischen Vorgänge in plerionischen Nebeln und insbesondere die Nachbeschleunigung von Elektronen aufgrund von magnetischer Rekonnektion im Nebel selbst. In Kapitel 4 wird ein Modell zur Erklärung der flachen Synchrotron-Spektren vorgestellt. Es beruht im wesentlichen darauf, dass die Schockfront als die großskalige Quellstruktur von rekonnektiver magnetohydrodynamischer Turbulenz interpretiert wird. Die an der Schock-

front akkumulierte Energie wird durch turbulente Plasma-Strömungen von großen räumlichen Skalen auf immer kleinere Skalen umverteilt, bis schließlich im dissipativen Bereich magnetische Rekonnektion aufgrund von einsetzender mikroturbulenter Resistivität ermöglicht wird. Magnetische Rekonnektion stellt hierbei einen effizienten Prozess zur Teilchenbeschleunigung dar. Dieser Prozess wird in unserer Arbeit anhand von dreidimensionalen hybriden Simulationen kompressibler resistiver magnetohydrodynamischer Turbulenz untersucht. Dabei dienen die Ergebnisse von MHD-Simulationen als elektromagnetische Konfiguration für Testteilchen-Simulation. Für die Teilchenenergien ergeben sich dabei Potenzgesetze $N(\gamma) \propto \gamma^{-s}$ mit Spektralindizes s zwischen 1.2 und 1.6. Somit ist unser Modell in der Lage, die flachen Spektren der Radiostrahlung von Plerionen durch die Nachbeschleunigung von Elektronen im Nebel zu erklären.

In Kapitel 5 wird der Elementarprozess der Teilchenbeschleunigung in rekonnektiven magnetischen Strukturen in einer Simulationsstudie im Detail behandelt. Dabei untersuchen wir die resistive Tearing-Instabilität anhand von hybriden Simulationen einer dreidimensionalen Stromschicht. Bei der Auswertung der voll entwickelten Tearing-Instabilität wird auf die Teilchendynamik und insbesondere auf die Energie- und Strahlungsspektren der Teilchen eingegangen. Unsere Rechnungen zeigen, dass solche Konfigurationen sehr effektiv Teilchen beschleunigen können, und sie sind nicht nur auf Plerionen anwendbar, sondern von generellem Interesse im Zusammenhang mit astrophysikalischen Objekten, u.a. in Sonneneruptionen und aktiven galaktischen Kernen.

Contents

Zusammenfassung	i
1 Introduction	1
1.1 Supernova remnants	2
1.2 The Crab Nebula	7
2 Models for Pulsar Wind Nebulae	15
2.1 Hydrodynamics of supernova explosions	15
2.2 Magnetohydrodynamics of pulsars	18
2.3 The σ problem	21
2.4 Particle acceleration and synchrotron emission in PWNe	24
3 Processes in turbulent plasma flows	27
3.1 Synchrotron emission	28
3.1.1 Radiation power	28
3.1.2 Spectrum	29
3.2 Magnetic reconnection	31
3.2.1 The tearing instability	32
3.3 Turbulence	33
3.3.1 Incompressible turbulent hydrodynamic flows	33
3.3.2 Kolmogorov theory	35
3.3.3 MHD turbulence	37
4 Radio emission and particle acceleration in plerionic supernova remnants¹	41
4.1 Introduction	41
4.2 Reconnective MHD turbulence	43
4.3 Relativistic particle simulations	44
4.4 Conclusions	53

CONTENTS

5	Particle acceleration in three-dimensional tearing configurations²	55
5.1	Introduction	55
5.2	The MHD initial configuration	57
5.3	Simulations on particle acceleration	58
5.3.1	Non-relativistic particle acceleration	61
5.3.2	Relativistic particle acceleration	68
5.4	Discussion	71
6	Discussion	79
	Bibliography	81
	Danksagung	89

Chapter 1

Introduction

When a massive star has used up all fuel for nuclear burning, it reaches a state where the gravitational pressure can no longer be sustained by the radiation pressure. In the successive collapse protons and electrons are transformed into neutrons and neutrinos by means of electron capture reactions. Within only a few seconds the core consisting of neutrons collapses to a rapidly rotating neutron star and releases an enormous amount of potential energy in form of neutrinos (about 10^{57}). The resulting shock wave causes fusion reactions to occur in the outer layers of the star and when the shock front reaches the surface, the star explodes with about 20000 km/s.

The rapidly expanding shell compresses the surrounding interstellar medium and builds up a shock front. At this stage the medium in the shock front is hot and pressure forces are important which makes the shock front observable as an expanding shell. More and more interstellar medium is swept up and with increasing radius of the shell, the density of the shell material drops and radiative cooling becomes effective. Finally, when the velocity of the shell reaches comparable values to the random motions of the surrounding medium, the shell material merges with its environment and the shell loses its identity.

Supernovae (SNe) are very important events with regard to the chemical composition of the interstellar medium and evolution of a galaxy. After the Big Bang the universe was basically composed of hydrogen, helium and traces of lithium yielded by the primordial nucleosynthesis. Elements heavier than lithium are produced by nuclear fusion reactions inside of stars. Red Giants, the late phase in the evolution of low or intermediate mass stars, are capable of creating iron nuclei by nuclear fusion, but elements with higher atomic numbers are generated during SN explosions. Thus, SNe are the key source of heavy elements in the universe. Moreover, SNe not only produce heavy elements but they are also responsible for the dispersal and mixing of the elements. The expanding shell transports the created elements into the interstellar medium where they mix and disperse throughout the Galaxy.

Furthermore, SNe play a key role for the galactic ecosystem as they provide a continuous source of mechanical energy. The shock waves transmitted from SNe are

supposed to trigger star formation in nearby molecular clouds by compression of material. On galactic time and spatial scales SNe are regarded to drive “galactic fountains”, i.e. galactic flows of hot ionized gas into galactic halos, which have been widely observed in other galaxies. These “galactic fountains” provide a potential mechanism to power high velocity clouds in galactic halos before they fall back onto the galaxy plane as “galactic rain”. Thus, SNe play an important role in the galactic life-cycle of gas and dust. They represent the death of a star but can also cause the birth of a new star.

1.1 Supernova remnants

The first identification of a Supernova Remnant (SNR) was published by Bolton, Stanley & Slee (1949). They associated the Crab Nebula, which has been known since its discovery in 1731 by John Bevis, with the radio source Taurus A. This was the first radio source to be identified with an optical object outside the Solar System. In subsequent various radio surveys many more SNRs have been identified and studied in great detail. Recent observations in the X-ray band with *ROSAT*, *Chandra* and *XMM* extended the available information on SNRs. This combination of observations in various different bands revealed interesting details.

So far, 231 Galactic SNRs have been cataloged by Green (2004) and very recently Brogan *et al.* (2006) discovered up to 35 new SNRs in the inner Galaxy from a 90 cm multiconfiguration Very Large Array survey. However, there still exists great discrepancy between the *expected* number of Galactic SNRs ($\gtrsim 1000$) and the significantly smaller number of currently *known* SNRs. This likely results from selection effects acting against the detection of old, faint and large remnants as well as very young and small ones. Diffuse Galactic plane synchrotron emission and thermal H II regions towards the center of the Galaxy are the cause of great confusion and make it difficult to detect SNRs in this part of the Galaxy. The number of expected SNRs is usually derived from statistical studies of Supernova (SN) rates, based on OB star counts, pulsar birth rates, Fe abundance, and the SN rates in other local group galaxies (Li *et al.*, 1991).

SNRs can be divided into three morphological classes (Weiler 1983): Shell-like SNR, plerionic SNR and combination or composite SNR. All SNRs show extended structure and are strong sources of non-thermal radio emission. Their radio spectra can be well described by a power law $S_\nu \sim \nu^{-\alpha}$, with S_ν being the observed flux density at the frequency ν with a constant spectral index α . However, shell-like SNRs have a shell or partial shell form with a mean spectral index of $\alpha \sim 0.45$ whereas plerions offer much flatter indices of $\alpha \sim 0.0$ to 0.3 and their form is a filled center or blob-like appearance, which is brightest in the center and decreases gradually in all directions towards the edges. Also, the grade of polarization differs: plerions show a much stronger integrated linear polarization at high ν than shell-like remnants. Combination-type SNRs still show the shell-like morphology but offer a central region with enhanced radio emission and a flatter spectrum.

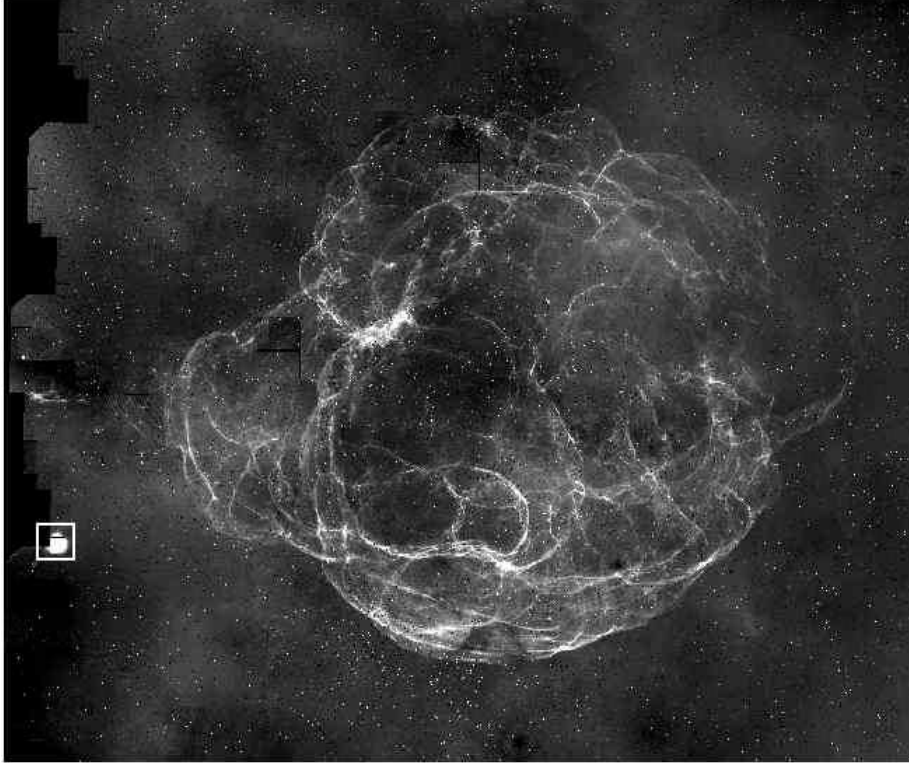


Figure 1.1: The continuum-subtracted $H\alpha$ image mosaic of the SNR S147.

More than $\gtrsim 3/4$ of the identified SNRs are of shell like morphology. Therefore many members of this class have been studied in great detail. Their distinctive feature is the shell form, which can be seen in the radio, optical and sometimes in the X-ray band.

Fig. 1.1 shows the well studied SNR S147 which is located towards the Galactic anti-center. It is an optically faint, highly filamentary galactic SNR of age $\sim 10^5$ years with a distance of ~ 800 pc. It has a shell-like structure and is one of the most evolved SNRs. The optical filaments are thought to represent portions of a radiative blast wave, which expands with a velocity of about 100 km s^{-1} . The remnant harbors a pulsar which is without much doubt the associated neutron star.

Many shell-like Galactic SNRs exhibit a distinctive feature: Their appearance is of bilateral symmetry, in some cases almost of mirror symmetry with a clear symmetry axis, i.e. parts of their opposing shell sides with respect to the symmetry axis, show brighter radio emission. This feature is often explained with the SNR's three dimensional form being cylindric or barrel-shaped. Thus, the brighter parts of the shell represent the walls of the barrel while the darker parts the bottom and the top. Fig. 1.2 shows the radio images of two SNRs of this kind. The solid lines represent a constant Galactic latitude and the broken lines the bilateral symmetry

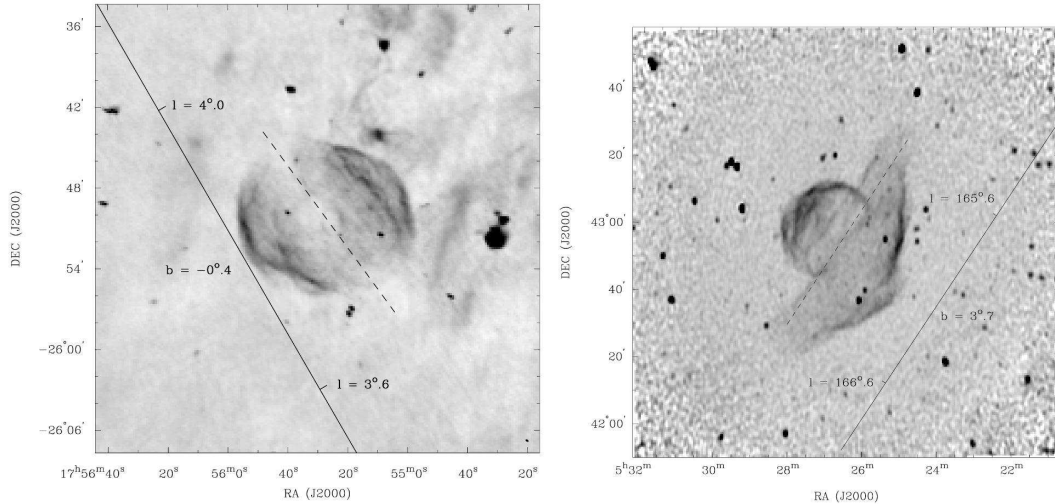


Figure 1.2: Radio images of the Galactic barrel shaped SNRs G003.8-0.3 and G166.0+4.3. The solid lines represent a constant Galactic latitude and the broken lines represent the SNRs' symmetry axis, which closely align with the Galactic Plane.

axis of the SNRs. The striking fact here is that the symmetry axes closely align with the Galactic Plane. This not only holds for the examples presented here, but for almost *all* observed Galactic barrel-shaped SNRs. The probability of this distribution occurring by chance is 0.0007 (Gaensler 2000).

A natural explanation for the alignment of barrel-shaped SNRs would be that the Galactic magnetic field, which generally runs parallel to the Galactic Plane, is somehow responsible for the orientation of the SNR. The most obvious mechanism is the compression of the Galactic magnetic field where it is perpendicular to the shock normal of the shell (the walls of the barrel) compared to no amplification where it is parallel (the top and bottom). This could explain the enhanced synchrotron emission observed from regions, where the magnetic field is amplified, and also the elongated shape of the SNRs, since expansion preferably takes place along magnetic field lines. Fulbright & Reynolds (1990) have considered such models including magnetic field evolution and diffuse shock acceleration. Their model in which the particle acceleration efficiency is highest where the shock normal is perpendicular to the magnetic field, produced radio maps that are qualitative similar to the ones observed. However, the quantitative results disagreed with the observations. The idea of field-geometry-dependent particle acceleration efficiency was confirmed by subsequent two-dimensional magnetohydrodynamical simulations with explicit relativistic electron transport (Jun & Jones, 1999).

Although it is assumed that pulsars are formed in SN explosions, observable associations of pulsars with SNRs are still very rare. Part of the problem in finding SNR-pulsar associations lies in distinguishing between what is a real association and what is merely a chance alignment on the sky. As in many other fields of astron-

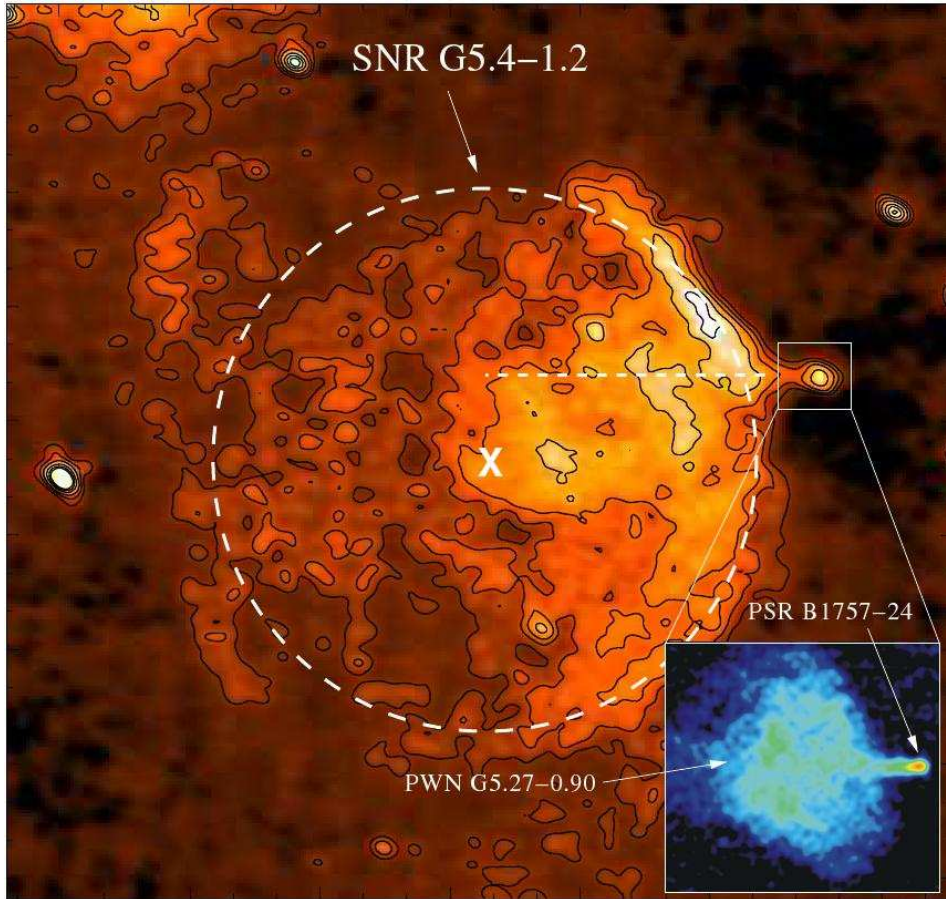


Figure 1.3: The radio SNR G5.4-1.2 and the 125-ms pulsar B1757-24. The dotted circle depicts the outline of the SNR. It seems as if the pulsar has moved along the dotted line to its current location, outside of the SNR. The small image in the lower right corner shows the pulsar and its wind nebula.

omy the proper determination of distances is very difficult. Additionally, intrinsic properties of SNR and pulsars complicate their association: The pulsars beam is not required to sweep across the view of an observer here on earth, which would obviously be the case for most pulsars. Another problem concerns the different “detectability” lifetimes: pulsars are 100 times longer detectable than SNRs. Consequently, the associated SNR of many pulsars might already be too faint for detection. Also, it simply might be a matter of deeper searches towards distant SNRs to uncover more associations.

The SN explosion of a moving massive star can result in a significant offset of the neutron star’s birth place from the geometrical center of the SNR. Furthermore, in most cases SN explosions are not radial symmetric but universally asymmetric (Wheeler *et al.* 2004). This can result in a change of the star’s momentum, i.e. the remnant’s velocity and direction of motion can significantly differ from the val-

ues of the progenitor star. The change in the remnant's momentum becomes even more complicated and unpredictable if the progenitor star has been part of a binary system, as is the case for most stars. The system could get dissolved during the explosion and the core-collapsed remnant could completely change its motion in relation to the binary system prior the explosion.

Fig. 1.3 shows a remarkable example of such a SNR-pulsar displacement. This complex of SNR, pulsar wind nebula and pulsar is a very controversial issue. Several authors (Manchester *et al.* 1991, Gaensler & Frail 2000) have argued that the SNR and the pulsar are associated, which implies that the pulsar was born with such a high velocity that it has overtaken the SNR shell and now lies outside the shell. The region around the pulsar along the western edge of the SNR is much brighter and exhibits a significantly flatter spectrum than the other parts. The pulsar is surrounded by a radio nebula, whose properties are consistent with it being powered by the pulsar's relativistic wind. It has a cometary morphology with its tail pointing back towards the center of the SNR. This strongly suggests that the pulsar is travelling away from the center at high velocity.

1.2 The Crab Nebula

The most prominent but also most unusual plerion is the Crab Nebula, which represents the prototype of its kind (depicted in Fig. 1.4). It is the closest, and consequently the most observed of all known plerions. Weiler & Panagia (1978) proposed the name plerion for all Crab-like SNRs, derived from the ancient Greek word pleres, which means “full”. Nowadays, the name Pulsar Wind Nebula (PWN) is much more common throughout the community as it describes these objects more accurately. Throughout this work, we will use both names interchangeably. The Crab Nebula is a remnant of a supernova explosion that occurred in the year 1054. It was eye-witnessed and reported by the Chinese astronomer Wang Yei-te and was visible during daylight for three weeks and at night for 22 months. The nebula itself was discovered by John Bevis in 1731 and rediscovered by Charles Messier in 1758, who made it the first object in his catalog.

At the center of the nebula resides the Crab pulsar, which produces a powerful wind of highly relativistic particles. This wind supplies the surrounding nebula with energy that is converted into synchrotron radiation at wavelengths reaching from radio emission up to γ -rays. The nebula offers a very flat spectral index with an almost homogeneous spatial distribution and a high degree of linear polarization (see Fig. 1.5). The origin of the radio synchrotron radiation will be covered by this work.



Figure 1.4: The Crab Nebula.

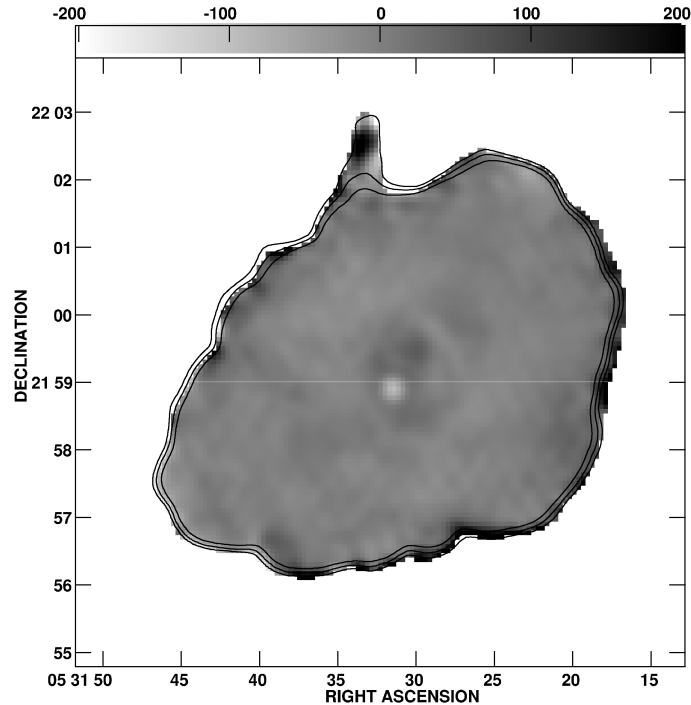


Figure 1.5: The spatial distribution of the Crab Nebula’s relative spectral index between 324 MHz and 1.5 GHz in units of 0.001. The map shows the difference of the spectral index to the mean spectral index of $\alpha = -0.27 \pm 0.04$.

A striking feature of PWNe are the distinctive filamentary structures, which can be seen in the radio band and also at optical wavelengths as line emission. Trimble (1968) has measured the proper motions of the Crab Nebula’s filaments and found that the expansion of the nebula has been somewhat accelerated. The motions are largely radial, with each filament moving at a velocity approximately proportional to its distance from the expansion center. She finds the filaments to be distributed throughout the nebula rather than being confined to a thin outer envelope.

Later investigations by Clark *et al.* (1983) on newer observational data revealed a more detailed picture of the Crab Nebula’s structure, confirming and extending the accepted model by Trimble. They modelled the Crab Nebula as a prolate spheroid, which consists of a thick, hollow shell with synchrotron emission from within. The thick shell is composed of bright inner and faint outer components surrounded by a high velocity halo. The filaments are concentrated in two concentric thin shells at the inner and outer boundary of the thick shell with linking filaments inbetween. There is a sharp discontinuity in brightness at the inner shell that divides the thick shell from the inner main region. They depicted the structure of the filaments to be like a tangled net, loosely bundled around a hollow ball (Fig. 1.6). In contrast to most other SNRs the Crab Nebula shows no extended radio shell, that is supposed to represent the interaction of the remnant material with the interstellar medium.

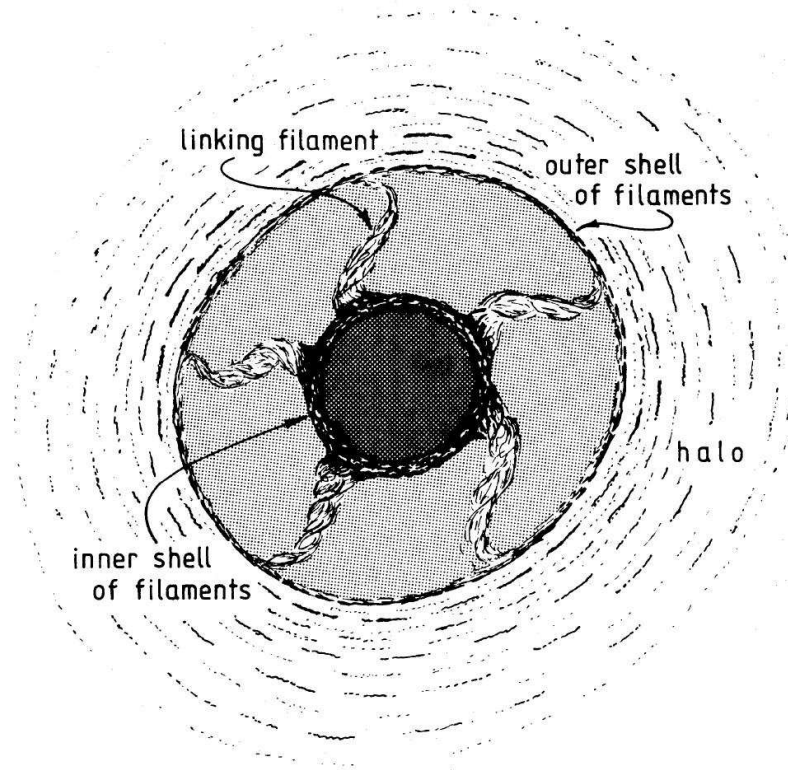


Figure 1.6: A cross-section through the Crab Nebula given by Clark *et al.* (1983). The shaded areas represent regions of synchrotron emission. Higher emission is observed from within the inner shell (dark shading) and weaker emission from inbetween the shells (light shading).

It might be possible that the outer thin shell represents the expanding remnant envelope ejected by the SN explosion, while the radio emission from the inner thin shell is due to synchrotron radiation from relativistic electrons generated by the pulsar. Differences in the spectral index of the two shells provide support for this interpretation.

Several authors have attempted to model the formation process of the filaments. Simon & Axford (1967) considered a thermal instability governed by energy losses of a relativistic electron gas due to synchrotron radiation and the inverse Compton effect, to be capable for the creation of the thermal filaments. For this they assumed a two component, highly conducting medium and a uniform, frozen-in magnetic field. One of the components is cold with negligible internal energy but providing most of the inertia of the system. The other component constitutes a hot gas with most of the internal energy and negligible inertia, comprised of the relativistic electrons originating from the pulsar. Thermal conduction is only associated with the relativistic electrons, which move along the magnetic field lines. It is very large parallel to the magnetic field and very small perpendicular to it. This leads to

a thermal instability propagating perpendicular to the magnetic field and to the formation of field-aligned filamentary condensations, acting on the synchrotron-loss time scale.

Other authors (Chevalier & Gull, 1975; Reynolds, 1988) considered the Rayleigh-Taylor instability at the interface between the dense expanding shell and the thin ambient medium to be the most reasonable explanation for the formation of the filaments. Reynolds investigated the Rayleigh-Taylor instability, operating on thermal gas accelerated by the pulsar, that interacts with non-thermal filaments, which result from the interaction of the pulsar-generated magnetic flux and relativistic particles with the thermal structures. Hester *et al.* (1996) considered the outer filaments to be the result of a magnetic Rayleigh-Taylor instability between the synchrotron plasma and the pressured, much denser swept-up material. Hence, they find the filamentary layer to be considered a skin on the surface of the nebula.

In contrast to the radio synchrotron emission, an enhancement of the optical synchrotron emission is not observed in the filaments. Weiler (1980) offered a possible explanation for the spatial correlation of optical thermal filaments and enhanced radio synchrotron emission that also explains the lack of optical enhancement. He proposed a mechanism, by which the compression of the interstellar magnetic field and acceleration of Galactic background synchrotron electrons by the expanding SNR leads to the enhanced synchrotron radio emission. Consequently, the radio synchrotron emission should have a steeper spectral index of $\alpha \sim 0.4$ equal to that of the Galactic background radiation. Later that year Swinbank (1980) ruled out this hypothesis since she did not detect variations in the spectral index greater than ± 0.3 . She concluded that the relativistic electrons in the filaments and the surrounding material producing the radio emission at 2.7, 5 and 23 GHz have the same origin, namely the pulsar. In addition, Velusamy, Roshi & Venugopal (1992) also argued that the magnetic field cannot be of galactic origin and therefore Weiler's hypothesis might be incorrect. For this they analyzed the linear polarization data and found that the magnetic field is aligned parallel to the filamentary and loop structures. The field along the outer loops and arches is connected with the field in the inner bright filaments and knots. This clearly argues against the hypothesis that the relativistic electrons and the magnetic field in the filaments is of Galactic origin.

Recent observations by Bandiera, Neri & Cesaroni (2002) at millimeter wavelengths confirmed the steepening of the spectral index in some elongated regions, whose positions match those of the radio filaments. They conclude that the magnetic fields in the synchrotron filaments are stronger than the average nebular field. Furthermore, they found the spectral index to get flatter towards the center of the nebular. This fact can hardly be explained just in terms of the evolution of a single population of relativistic electrons. Hence, they proposed the emergence of a second synchrotron component producing the enhanced radiation with flatter spectral index towards the center.

Velusamy, Roshi & Venugopal (1992) also produced high-resolution radio maps of the filamentary structure of the Crab Nebula, which confirmed the proper mo-

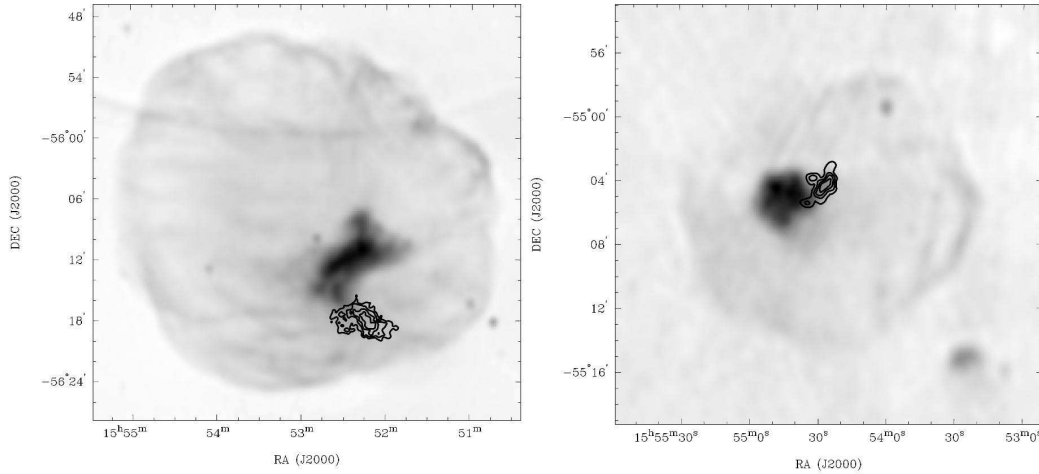


Figure 1.7: Two examples of composite SNRs: MSH 15-56 (left) and G327.1-1.1 (right). The grayscale shows the radio emission at 843 MHz and the black contour lines illustrate the X-ray emission.

tion measurements of the filaments of Trimble (1968). Additionally, they found a correlation between the spectral index of the filament’s radio spectra and their position: the spectrum steepens away from the center, with $\alpha \sim 0.3$ in the inner and $\alpha \sim 0.4$ in the outer regions. This corresponds to the steepening observed at millimeter wavelengths and in the X-ray regime. Recent spatially resolved spectra of PWNe done with *Chandra* and *XMM* reveals spectral steepening towards the edges, with the hardest spectrum at the center having an index around $\alpha_X \sim 0.6$. The most obvious explanation for the steepening inside the filaments as well as the steepening towards the edges would be the increasing synchrotron energy loss. Within the filaments the higher energy loss is caused by an increased magnetic field. The steepening towards the edges naturally occurs while the relativistic electrons diffuse outwards from the center, permanently experiencing synchrotron losses.

In the X-ray regime PWNe show a hard, nonthermal power-law spectrum. For the Crab Nebula Toor & Seward (1974) found a best-fit power-law index $\alpha_X = 1.1$ in the energy distribution $F_\nu \propto \nu^{-\alpha}$. The X-ray emission generally is of much smaller extent than the radio emission which is assumed to be the result of the shorter lifetimes of the synchrotron-emitting electrons at the higher energies. More detailed observations at sufficient spatial resolution reveal that the X-ray structures seem to have axially-symmetric form such as tori or jets (Fig. 1.7). The spectrum at these wavelengths shows a much steeper spectral index $\alpha \sim 1$ than in the radio wavelength, which also is explained by lifetime arguments.

In addition to the spatial variations of the spectral index at various wavelengths, it has long been known that the Crab Nebula exhibits remarkable temporal variations in its central region (Lampland, 1921). These variations consist of fluctuations in brightness and changes in form and position of several small-scale structures close to

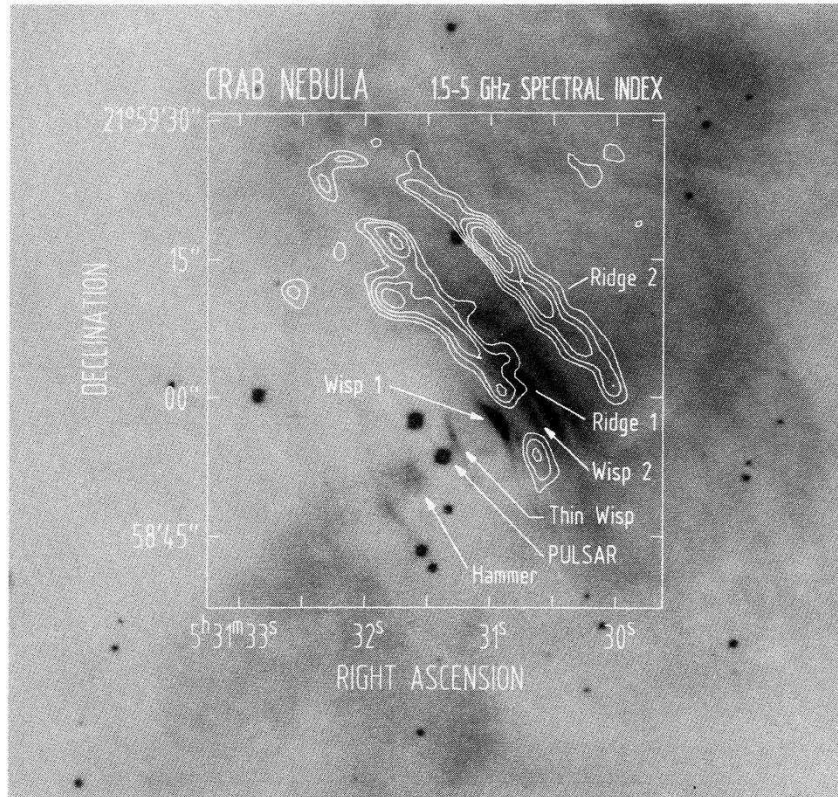


Figure 1.8: Contours of the radio spectral index overlaid on an optical image of the central region of the Crab Nebula.

the center. The structures are wisp-like in shape and show variations on timescales of weeks or even days. They are observed to be moving away from the pulsar at apparent velocities of up to $\sim 0.7 c$. These wisps were first detected in the optical continuum and later observations (Bietenholz & Kronberg, 1992) revealed that the optical structures seem to be associated with radio features at the same position. Bietenholz & Kronberg also detected a significantly *flatter* spectral index within the radio wisps which points to violent activities close to the pulsar (Fig. 1.8). The location of the wisps is generally assumed to coincide with the region where the pulsar wind terminates in a standing shock – the inner edge of the nebula.

Observations revealed that SNRs appear in a variety of different morphologies. There are pure shell-like SNRs which are supposed to be a result from a massive SN explosion. The shell, composed of several filaments resulting from the interaction of the initial shock wave with the interstellar medium, represents the remnant of the explosion. The main feature of this type is, that no activity in form of a synchrotron nebula can be observed. Either there is no central energy source supporting a nebula since the explosion completely disrupted the progenitor star, or the remnant is old and the pulsar has already exhausted its rotational energy. In that sense, shell-like

remnants represent the afterglow of the SN explosion before they are finally fading slowly into the Galactic background.

PWNe and combined SNRs, in contrast, still offer various activities all powered by their central energy source – a fast rotating, rapidly slowing pulsar. The pulsar produces a powerful stream of energy flux, partly in the form of a relativistic wind containing a toroidal magnetic field, and partly in the form of electromagnetic waves, i.e. the energy flow mainly consists of Poynting flux. The magnetic field and relativistic particles accumulate at the expected shock discontinuity where the wind meets the surrounding nebula. The magnetic energy builds up more rapidly than the particle energy content and small-scale outbreak-like events occur that are observed as wisp-like structures with increased velocity and radiation. Inside the nebula the injected energy is converted into kinetic energy of relativistic particles and eventually into the synchrotron radiation of the nebula.

Chapter 2

Models for Pulsar Wind Nebulae

Pulsar Wind Nebulae (PWNe) are synchrotron nebulae powered by a central pulsar, which has emerged from an earlier supernova explosion. The pulsar, a fast rotating neutron star offering a dipolar magnetic field, releases enormous amounts of energy in terms of a strong plasma wind consisting of Poynting flux and relativistic particles. At a distance where the confining pressure of the surrounding medium balances the momentum flux of the wind, a standing shock arises, in which the directed radial plasma motion gets randomized. This region is a site of violent outbreak phenomena, which are observed as synchrotron radiation of relativistic charged particles moving in distinctive wispy-like magnetic structures. The termination shock also marks the inner edge of the plerionic nebula, which emits synchrotron radiation over a wide range of frequencies. In the following sections we will review several hydro- and magnetohydrodynamical models for the formation and development of PWNe. We start off with an hydrodynamic description of Supernova explosions in section 2.1 which provides a rough sketch of the initial event possibly leading to the formation of a PWN. Section 2.2 covers aspects of the evolution and inner magnetohydrodynamical structure of PWNe and outlines several existing models. Observations impose a certain value for the ratio of magnetic to kinetic energy flux σ at the inner edge of the nebula in order to be consistent with current models. The arising problem will be discussed in section 2.3.

2.1 Hydrodynamics of supernova explosions

A supernova can be thought of a sudden explosion within a local region of gas, just like a bomb exploding in air. Such explosions give rise to an expanding blast wave propagating through the surrounding medium, sweeping up more and more material in the process. As a first approximation the front of the blast can be treated as a

hydrodynamic shock wave, across which the Rankine-Hugoniot conditions

$$\frac{\rho_1}{\rho_0} = \frac{(\gamma + 1)\mathcal{M}^2}{2 + (\gamma - 1)\mathcal{M}^2} \quad (2.1)$$

$$\frac{p_1}{p_0} = \frac{2\gamma\mathcal{M}^2 - (\gamma - 1)}{\gamma + 1} \quad (2.2)$$

must hold. Here, the subscripts 1 and 0 denote the quantities inside and outside the expanding shell in a reference frame where the shock front is at rest, respectively. Accordingly, v is the velocity of the gas, ρ the density, p the pressure, γ the adiabatic index and $\mathcal{M} = v_0/\sqrt{\gamma p_0/\rho_0}$ denotes the Mach number.

The problem is described hydrodynamically by the spherically symmetric continuity equation, the Euler equation and the adiabatic equation

$$\frac{\partial \rho}{\partial t} + \frac{1}{r^2} \frac{\partial}{\partial r}(r^2 \rho v) = 0, \quad (2.3)$$

$$\frac{\partial v}{\partial t} + v \frac{\partial v}{\partial r} = -\frac{1}{\rho} \frac{\partial p}{\partial r}, \quad (2.4)$$

$$\left(\frac{\partial}{\partial t} + v \frac{\partial}{\partial r}\right) \log \frac{p}{\rho^\gamma} = 0. \quad (2.5)$$

These equations qualify the evolution of macroscopic quantities like the density ρ and the velocity field v . Here, we assume that the initial explosion is spherical symmetric and that the ambient medium has a uniform distribution.

In order to find a solution Sedov (1946) and Taylor (1950) introduced a further simplification. They showed independently¹ that this problem can be solved under the assumption that the blast wave evolves in a self-similar way, i.e. the initial configuration expands uniformly. They realized that the initial energy ϵ_i , the density ρ_0 , the pressure p_0 of the surrounding medium, the radius r_S of the blast wave and the time t are the only parameters characterizing the problem. Since the energy of the explosion is enormous, the pressure p_0 can be neglected. This leaves 4 parameters, which can be combined to the single dimensionless constant number $\epsilon_i t^2 / \rho_0 r_S^5$. Therefore any later configuration will be an enlargement of the initial configuration scaling with the length $\lambda(t) = (\epsilon_i t^2 / \rho_0)^{1/5}$. The assumption of self-similarity demands the radius $r(t)$ of a shell inside the spherical blast to evolve the same way as $\lambda(t)$. Accordingly, we can introduce the dimensionless distance parameter

$$\xi = \frac{r}{\lambda} = r \left(\frac{\rho_0}{\epsilon_i t^2} \right)^{1/5} \quad (2.6)$$

which is constant for a particular shell. If ξ_S corresponds to the shock front, we can give expressions for the radius of the spherical blast

$$r_S(t) = \xi_S \left(\frac{\epsilon_i t^2}{\rho_0} \right)^{1/5} \approx 0.3 t^{2/5} \text{ pc} \quad (2.7)$$

¹Taylor's work was initially classified because it was part of research on atomic bomb explosions. It was then published a few years after the second world war.

and its velocity

$$v_S(t) = \frac{dr_S}{dt} = \frac{2}{5}\xi_S \left(\frac{\epsilon_i}{\rho_0 t^3} \right)^{1/5} \approx 10^5 t^{-3/5} \text{ km/s.} \quad (2.8)$$

The numerical values result from typical values of $\rho_0 \approx 2 \times 10^{-24} \text{ g/cm}^3$ and $\epsilon_i \approx 10^{51} \text{ erg}$ (time t has to be put in years). The kinetic energy of the initial blast $\epsilon_i = M_i v_i^2 / 2 = 1 M_\odot \cdot 10^4 \text{ km/s} \approx 10^{51} \text{ erg}$ is assumed to be conserved inside the spherical blast, which cannot be correct, since energy is continuously radiated away from the system. This effect, however, is only important after an appreciable amount of time when radiative cooling becomes effective. We further note that (2.8) gives values larger than our given initial velocity of 10^4 km/s for times $t < 100$ years. This certainly makes no sense and expression (2.8) cannot provide the correct values for v_S for the first 100 years. As a result, Woltjer (1972) distinguishes between 4 different phases of SNR evolution.

Free expansion: In this phase the blast wave expands with its initial velocity and the radius increases linearly with time. This continues until the mass of swept up material $(4\pi/3)\rho_0 r(t)^3$ becomes comparable to that of the material of the explosion M_i , i.e. until $1 - 10 M_\odot$ has been swept up.

Adiabatic expansion (Sedov-Taylor phase): This is the phase when equations (2.7) and (2.8) hold. The expanding shock front heats up the material inside the spherical blast but radiative losses, compared to the initial energy release are negligible, i.e. $\int (d\epsilon/dt)_{rad} \ll \epsilon_i$. and the energy is conserved. In order to give an estimate of the macroscopic quantities inside the sphere we assume that the ambient gas is cold and has a adiabatic index of $\gamma = 5/3$. From (2.1) in the limit of strong shock ($\mathcal{M} \rightarrow \infty$) we obtain an upper limit for the pressure behind the shock of

$$\rho_1 = \frac{\gamma + 1}{\gamma - 1} \rho_0 = 4\rho_0. \quad (2.9)$$

Of course, this only is valid directly behind the shock as the density further inside the sphere actually decreases, but for our successive estimates it should be sufficient enough. From (2.2) we can follow an expression for the pressure just behind the shock

$$p_1 = \frac{2}{\gamma + 1} \rho_0 v_S^2 = \frac{3}{4} \rho_0 v_S^2. \quad (2.10)$$

Given that we are considering an ideal gas, this leads to an estimate for the temperature behind the shock

$$T_1 = \frac{\bar{m}}{\rho_1 k_B} p_1 = \frac{3}{16} \frac{\bar{m}}{k_B} v_S^2, \quad (2.11)$$

where \bar{m} denotes a mean mass per particle behind the shock front.

Radiative Phase: The cooling time of the material behind the expanding shell has become comparable to the expansion time t . As a result, the material cools quickly through bremsstrahlung, recombination radiation and line emission. Consequently, the temperature drops and the pressure of the material behind the shock on the shell is negligible. The effect of the surrounding medium on the motion of the shell can still be neglected. Hence, the shell moves with constant momentum and the radius in this phase is given by

$$R_S = R_{rad} \left(\frac{8}{5} \frac{t}{t_{rad}} - \frac{3}{5} \right)^{1/4}. \quad (2.12)$$

The subscript *rad* denotes the constant values of the quantities at the beginning of this phase.

Cold Phase: Finally the velocity of the shell becomes comparable to the random velocities of the interstellar medium (~ 10 km/sec). The shell loses its identity and merges into the interstellar medium.

The above, however, is a pure hydrodynamic description of the explosion that only provides a rough sketch of the long term evolution of SNRs. In order to clarify further details of SNRs and PWNe one surely has to incorporate magnetic fields as they add a further constraint on the motion of the fluid. Magnetic fields are inherently present throughout the universe and, in particular, with regard to the fact that pulsars provide a strong source of magnetic energy, they will play a key role in the grasp of PWNe.

2.2 Magnetohydrodynamics of pulsars

Assuming that the Crab nebula's radio, optical and X-ray continuum radiation is of synchrotron type, and that the magnetic field inside the nebula is not far away from its equipartition strength, one can conclude that the Crab nebula contains a magnetic field of strength $10^{-3} - 10^{-4}$ G and a total energy of $\sim 10^{49}$ erg in form of relativistic leptons. Most of the observed synchrotron energy emission is in the ultra-violet and X-ray band. For these values of particle energy and magnetic field strength the particles' synchrotron lifetimes are less than the age of the nebula. This implies that there is a continuous injection of highly relativistic leptons with Lorentz factors of up to $\gamma \simeq 10^8$ in order to retain the synchrotron output. Also, the observed magnetic field inside the nebula cannot be a pure relic of the original explosion since adiabatic losses would have transformed it almost completely into the expansion of the nebula. Thus, the magnetic energy content of the nebula must also be provided by an external source.

In the last section we addressed the hydrodynamical evolution of a stellar explosion. We did not take into account that the explosion might leave a further source of energy: the remaining fast rotating neutron star in the center of the remnant. This pulsar has great influence on the nebula and represents the source of relativistic

particles and magnetic field due to its powerful magnetized plasma wind. Weiler & Panagia (1978) proposed that a rapidly rotating, rapidly slowing pulsar is necessary to create and maintain a PWNe. They concluded that PWNe therefore are relatively short-lived with respect to shell like remnants and fade away quickly since the pulsar very quickly releases large amounts of energy into the surrounding nebula.

In a basic approximation a star is usually considered as a rotating spherical object with a dipolar magnetic field. In general, the dipolar axis does not need to be aligned with the rotational axis, so that there is an angle Θ between these two axes. We now consider the collapse of a massive star to a very compact neutron star with a much smaller radius R_N (~ 10 km) than the progenitor star. Due to conservation of angular momentum and magnetic flux during the collapse, the neutron star will obtain extraordinarily high values for the angular frequency of rotation Ω and the magnetic field strength at the pole B_0 ($\Omega \sim 30$ Hz and $B_0 \sim 10^8$ T in the case of the Crab pulsar). A magnetic dipole of this kind, rotating *in vacuum*, will emit electromagnetic radiation with an energy loss rate given by (Landau & Lifshitz, 1951)

$$L = \frac{2m^2}{3c^3} \Omega^4 \sin^2 \Theta, \quad (2.13)$$

where the dipole moment m is defined by

$$m = \frac{\Phi R}{2\pi} = \frac{B_0 R_N^3}{2}. \quad (2.14)$$

Here, Φ is the magnetic flux through the half sphere about the pole. This energy loss leads to a decrease of angular momentum of $\dot{J} = L/\Omega$ and, consequently, to a decrease of the angular frequency at a rate of $\dot{\Omega} = \dot{J}/I$, with I being the moment of inertia. Finally, the energy flux provided by a pulsar due to its loss of angular momentum, can be written as the spin down luminosity

$$L = -I\Omega\dot{\Omega}. \quad (2.15)$$

This represents all the power residing in the pulsar's wind. In the case of the Crab nebula the decrease of the pulsar's angular frequency can indeed be observed and the spin down luminosity has a value of $L \approx 5 \times 10^{38}$ erg/s. This value exceeds the total nebular synchrotron luminosity by a factor of ~ 10 . Thus, the pulsar has an efficiency of $\sim 10\%$ in converting its rotational energy into the kinetic energy of relativistic particles and, finally, into synchrotron radiation.

At a closer look the foregoing assumption of the pulsar rotating in vacuum turns out to be quite unrealistic. Goldreich & Julian (1969) considered the aligned rotator – a fast rotating neutron star with a dipolar magnetic field whose dipolar axis is aligned with the rotational axis ($\Theta = 0$). If the neutron star was surrounded by vacuum, the resulting charge density on the star's surface would induce a very strong quadrupolar electric field which has a large parallel component to the magnetic field

$$\mathbf{E} \cdot \mathbf{B} = - \left(\frac{\Omega R_N}{c} \right) \left(\frac{R_N}{r} \right)^7 B_0^2 \cos^3 \theta, \quad (2.16)$$

where r and θ are the spherical positional coordinates. The value of the electric field strength at the surface exceeds the gravitational pull by a factor of 10^{12} . This allows for charged particles to be ripped out of the surface at the polar caps and be accelerated to highly relativistic energies. As a consequence, the assumption of a surrounding vacuum cannot hold. The charge density that shields the induced electric field is the so-called Goldreich-Julian density

$$\rho_{GJ} = \frac{\nabla \cdot \mathbf{E}}{4\pi} = -\frac{\Omega \cdot \mathbf{B}}{2\pi c} \frac{1}{1 - (\Omega r/c)^2 \sin^2 \theta}, \quad (2.17)$$

which gives us an estimate of the plasma density in the pulsar's magnetosphere. In effect, the plasma acts as an extension of the star's conducting surface and is corotating with the same angular frequency Ω . However, corotation must break down at a distance from the axis of rotation where the plasma reaches the speed of light. This radius defines the light cylinder $R_L = c/\Omega$. Inside R_L the motion of charged particles can be thought of as sliding along the frozen-in poloidal magnetic field lines.

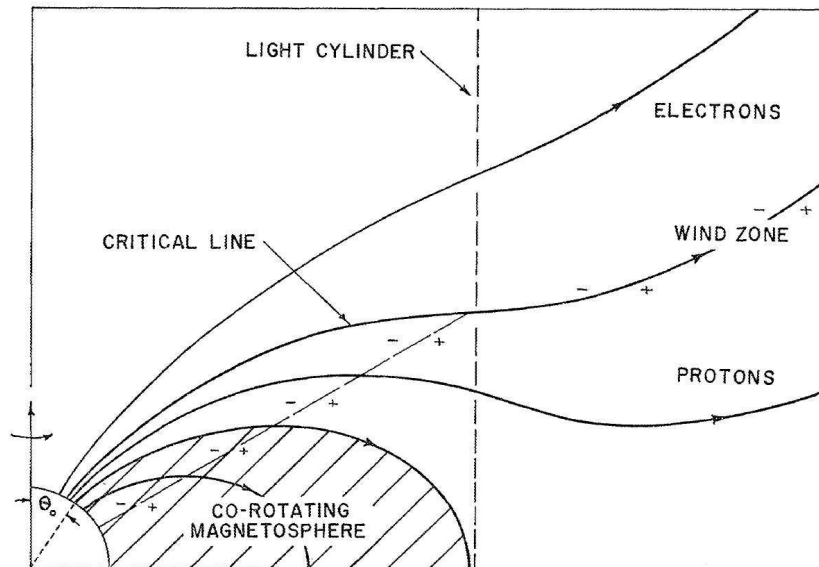


Figure 2.1: The pulsar's corotating magnetosphere and the transition into the wind region at the light cylinder at R_L . Θ denotes the angle between the neutron star's axis of rotation and magnetic axis.

Outside the light cylinder the open field lines of the rotating dipolar magnetic field are bent backwards and build up a toroidal component, which becomes increasingly dominant with added distance from the pulsar. The magnetic field is determined everywhere by the current distribution of the moving charges, inside R_L essentially by the current in the star, and outside by the current of the escaping particles. These particles and the toroidal magnetic field provide a strong relativistic magnetized wind which streams outwards towards the ambient interstellar medium.

In their classical paper on the origin of magnetic field and relativistic particles in the Crab nebula Rees & Gunn (1974) divided the energy flow surrounding the pulsar into three components. One carried by low frequency electromagnetic waves of type (2.13) which result from the assumption that the angle Θ between rotation and magnetic axis is $\neq 0$. These waves provide the energy flux L_{wave} . The second component L_{wind} results from the wind of relativistic particles and forms the kinetic energy flux. The third component L_{mag} is the non-time varying part of the Poynting flux, integrated over a sphere centered on the pulsar, which represents the wound up toroidal magnetic field carried outwards by the wind. They argued that L_{wave} will be completely absorbed at $R = R_S$ by either synchrotron absorption or statistical acceleration, and hence the associated power will be transferred to the relativistic electrons. Furthermore, they pointed out that L_{wind} and L_{wave} together account for $\gtrsim 90$ percent of the total pulsar luminosity and gave an estimate of $R_S \approx 10^9 R_L$.

The magnetosphere's as well as the wind's magnetic energy density in the vicinity of the pulsar greatly exceeds the particle energy density. This follows from the extraordinary high magnetic field close to the pulsar and estimates of the number of pairs emitted by the neutron star (Kennel & Coroniti, 1984a). Accordingly, the energy flux carried by the wind while close to the star is dominated by Poynting flux. Magnetohydrodynamical models of pulsar winds assume that the wind terminates in a standing shock at a radius R_S , which is defined by the condition that the confining pressure balances the momentum flux of the wind. At the inner edge of the Crab Nebula, where the wind passes through the termination shock, the wind must have a very low magnetization, if it is to match the observed expansion speed of the Nebula. Thus, unless the structure of the termination shock is very different from that of a hydrodynamic shock, dissipation of the magnetic field in the flow must occur before the flow reaches this radius.

2.3 The σ problem

The pulsar's spin-down luminosity due to a radially outflowing relativistic plasma wind transporting magnetic and kinetic energy reads as

$$L = 4\pi\rho\gamma c^3 R^2(1 + \sigma), \quad (2.18)$$

where the ratio of Poynting flux to kinetic energy flux in the wind is given by

$$\sigma = \frac{B^2}{4\pi\rho\gamma c^2}. \quad (2.19)$$

By considering the preceding remarks on the pulsars magnetosphere, one gets to the conclusion that $\sigma \gg 1$ at R_L where the wind is "launched". In the outer magnetosphere and inner wind the energy is tied up in electromagnetic fields and plasma flow. There is no direct observable evidence of the energy in form of electromagnetic radiation. Early observations of the central region of the Crab nebula revealed a "central hole", i.e. a region with lower brightness (Scargle, 1969). This fact led

Arons (1992) to the statement “the dog doesn’t bark in the night”. Thus, the pulsars luminosity gets transported far outwards by the wind, up to the termination shock at R_S without being diminished substantially by radiative losses.

On the other hand, most PWN models impose $\sigma_1 \ll 1$, where the subscript 1 denotes the value of σ upstream right at the termination shock. By observational measurements of the shell’s expansion velocity, from radiation modelling of the expanding bubble or from the kinetic theory of the termination shock, the models estimate σ_1 to be less than 0.01. Hence, somehow between the light cylinder at R_L , where the electromagnetic field carries most of the pulsar’s rotational energy, and the termination shock at R_S the magnetic energy must be converted into kinetic energy of relativistic particles, as there is no observable emission coming from this region. This puzzle is known as “the σ problem”.

Values for σ_1 are estimated from several observational facts. With regards to the PWN expansion velocities Kennel & Coroniti (1984a) investigated the Rankine-Hugoniot conditions of ideal MHD at the termination shock. They concluded that only for $\sigma_1 \ll 1$ most of the upstream particle energy density can be converted into downstream thermal energy density. This suggests that low- σ shocks can most efficiently convert wind luminosity into synchrotron radiation of the nebula. They find that a value of $\sigma_1 \approx 0.003$ upstream of the shock satisfies the confinement boundary conditions imposed upon the pulsar wind best.

For the downstream region of the shock, the actual nebula, the models of Rees & Gunn (1974) and Kennel & Coroniti (1984a) suppose a decelerating radial flow with $v(R) \sim R_S/R$ until a radius $R_{eq} = (2/9\sigma)^{1/2}R_S$, where the magnetized flow reaches equipartition and the deceleration stops. This in turn leads to an linearly increasing magnetic field in the nebula up to R_{eq} . By matching the observed expansion speed of the nebula with the asymptotic flow velocity they concluded the low value for σ_1 . An overview of the model is sketched in Fig. 2.2.

A different approach for the estimation of σ_1 is to conclude it’s value from the nebula’s synchrotron radiation. In a sense, this inverts causality as one asks what the observed nebular radiation reveals about the pulsar’s wind. This, however, is necessary since a model for the nebula cannot be constructed from the initial conditions at the pulsar due to the lack of information about this region. By going this way Kennel & Coroniti (1984b) found a value for σ_1 which is consistent with the value obtained by their dynamical arguments. They assumed that the flow energy is converted into kinetic energy of power law distributed pairs right at the shock via “shock acceleration”, i.e. diffusive Fermi acceleration. However, they only took the spectral index α of the high energy photon spectrum into account, i.e. the optical up to the X-ray range. For $\alpha = 0.6$ they found $\sigma_1 = 0.003$, exactly as in their previous work.

In order to simplify their models, theorists mainly consider unstructured winds in ideal MHD. An often discussed approach to the σ problem, which incorporates the consideration of a structured wind, is the striped pulsar wind as suggested by Michel (1969) and further developed by Coroniti (1990). For an oblique rotator the wind magnetic field near the rotational equator should consist of stripes of alternating

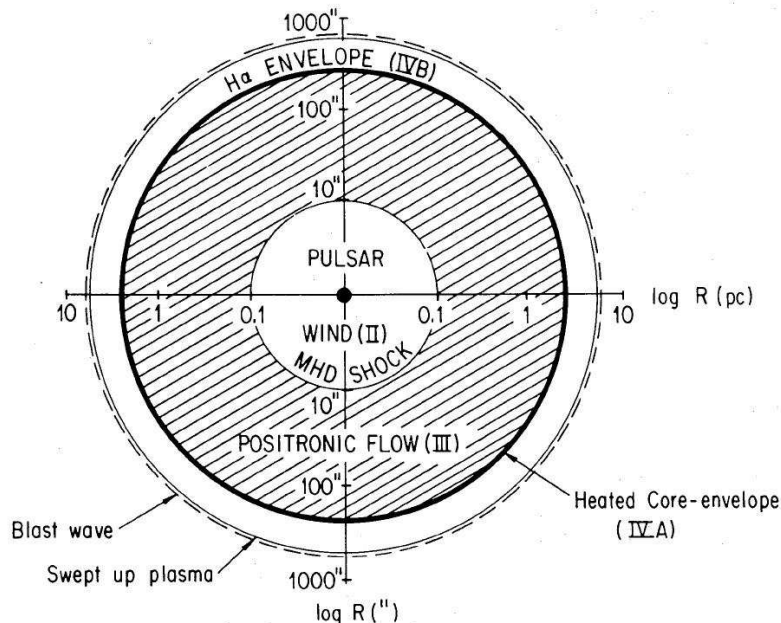


Figure 2.2: A schematic sketch of the Crab nebula. The image shows the different Regions of the nebula and important radii as proposed by Kennel & Coroniti (1984a). The dot in the center represents the pulsar whose relativistic positronic plasma wind streams until it terminates in a MHD shock at $R_S = 0.1$ pc. The hatched region represents the actual nebula, a region of decelerated positronic flow between the shock and the inner edge of the expanding SNR at $R_N = 2$ pc.

toroidal field. In the regions where the magnetic field's polarity changes, the dominating magnetic energy can be converted into particle thermal and directed kinetic energy by magnetic reconnection. Coroniti (1990) found that this conversion is fast enough to reduce σ to the value needed, well within the inner standing shock that terminates the wind. A later reexamination of this process by Lyubarsky & Kirk (2001) showed that the wind accelerates significantly in the course of reconnection which dilates the timescale over which the reconnection process operates, so that the wind requires a much larger distance than was previously thought in order to convert the Poynting flux to particle flux. For the Crab pulsar they found that the wind is still Poynting-dominated at the radius at which the termination shock is inferred from observations. However, Lyubarsky (2003) found that the alternating magnetic field completely annihilates at the termination shock so that the downstream parameters of the flow are the same as if the field has already annihilated upstream of the shock. Moreover, this results in particle acceleration by driven reconnection at the pulsar wind termination shock, producing a particle population with flat power law energy distribution that could provide a source for the radio emission.

The injection rate of the electron-positron pairs originating at the pulsar's surface is an important parameter for the striped wind models. Kirk & Skjæraasen (2003)

have investigated the dissipation of magnetic field in Poynting-flux-dominated flows by magnetic reconnection, with regard to the Crab pulsar wind, and showed that the reconnection rate critically depends on the pair injection rate. For injection rates $\dot{N}_{\pm} > 10^{40} \text{ s}^{-1}$ they found that the Poynting flux can be dissipated before the wind reaches the termination shock, thus providing a possible solution to the σ problem.

2.4 Particle acceleration and synchrotron emission in PWNe

Most investigations consider the acceleration of synchrotron particles at the termination shock. The favored acceleration mechanism is the diffusive first-order Fermi acceleration, which delineates the acceleration of charged particles by the reflection at magnetic mirrors that move towards each other at high velocity. In the shock region magnetic irregularities are expected on both sides of the shock. It is then possible that charged particles are trapped inside the shock region and are reflected repeatedly from the magnetic irregularities on both sides. In the non-relativistic regime the resulting particle energy spectrum in the shock is of the form $N(\gamma) \sim \gamma^{-p}$, with $p \gtrsim 2$. In relativistic shocks this mechanism is most efficient if the magnetic field is parallel to the flow, i.e. the magnetic field is parallel to the normal of the shock front (Ellison, Jones & Reynolds, 1990). The magnetic field in the shock structure in PWNe, however, is supposed to be almost perpendicular to the flow in the wind, at least in the equatorial plane. This suggests that the Fermi mechanism might be too little efficient for providing a substantial part of the high-energy particles. Therefore, some other mechanism different to shock acceleration must apply.

The composition of the wind plasma has important effects on the downstream particle energy distributions of the shock. A pure electron-positron plasma gets completely thermalized in the plane perpendicular to the magnetic field direction, with electron and positron energy distribution being very close to relativistic Maxwellian at the temperature expected from the jump condition, despite the complete absence of Coulomb collisions. This has been shown by means of Particle-in-Cell simulation techniques as well as analytic theory (Gallant *et al.*, 1992). Consequently, a perpendicular shock as assumed for the termination shock in PWNe is not capable of producing downstream particle populations with power law energy distributions. If, on the other hand, the upstream plasma contains ions as well, which are a minority constituent by number but which carry most of the energy density, the downstream energy distribution of the pairs will contain a non-thermal part with a power law spectrum of $N\gamma \sim \gamma^{-2}$. This is due to resonant absorption of ion cyclotron waves collectively emitted at the shock front. Here, the shock structure starts with a thin transition in which the pairs are heated to a downstream thermal distribution. The heavy ions penetrate this hot magnetized pair plasma, and begin gyrating in the shock compressed magnetic field. Such gyration is electromagnetically unstable and gives rise to low frequency electromagnetic waves in the pair plasma emitted by

the coherently gyrating ions. Resonant cyclotron absorption of these waves by the pairs leads to an acceleration of the pairs as they flow away from the shock front. This model is supported by hybrid (MHD and Particle-in-Cell) simulations of the shock region, showing features that are very similar to the observed X-ray rings and arcs seen in the Crab nebula (Hoshino *et al.*, 1992). Arons & Tavani, (1994) find the resonant ion cyclotron wave acceleration mechanism to be responsible for the production of the non-thermal *and* thermal pair populations.

The origin of the high-energy emission from the shock region can be well explained by current models but the flat spectrum of the radio emission is still unclear. Observations of the wisps in the radio range suggest that the electrons responsible for the radio emission are accelerated in the same region as those responsible for the higher energy emission. Lyubarsky (2003) already pointed out a possible mechanism for the creation of radio electrons at the shock by driven magnetic reconnection. However, if the radio emission is produced by low energy electrons, their origin is unclear, since it is difficult to produce them in sufficient quantity from a high- γ pulsar wind (Atoyan 1999). Most recently, Fleishman & Bietenholz (2007) modelled the diffuse synchrotron radiation from PWNe by electrons as the random walk in a stochastic magnetic field. The synchrotron spectrum of such a particle population differs substantially from those of standard synchrotron emission as the particles do not experience a regular field. Therefore, the concept of a quasi-circular gyration at the Larmor radius no longer applies and the particle trajectories become highly chaotic. Such stochastic fields are generated by turbulent magnetized flows, which are likely present in PWNe.

Our model as presented in chapter 4 considers the *in situ* particle acceleration everywhere inside the nebula due to reconnection of highly turbulent magnetic fields. The fast rotating pulsar creates a strong plasma wind which acts as the external force that permanently powers the surrounding nebula. At the termination shock, the region where the plasma wind encounters the surrounding medium the plasma becomes decelerated very rapidly. In this region strong Alfvén waves are created, which are expected to excite strong MHD turbulence throughout the nebula. MHD turbulence causes the system to redistribute magnetic energy from larger to smaller spatial scales until the resistive term in Ohm’s generalized law becomes important and magnetic reconnection sets in. The process of magnetic reconnection allows the conversion of magnetic energy into other forms, in particular, in situ energization of relativistic particles. In the next chapter we will go into detail on the physical processes that are relevant to this scenario.

Chapter 3

Processes in turbulent plasma flows

Electromagnetic radiation can be classified into two major groups depending on the energy distribution of the light emitting particles: thermal and nonthermal radiation. Thermal light sources are basically in thermodynamical equilibrium so the light emitting particles show a Maxwellian distribution. The radiation is emitted due to energy transitions of bound electrons and for multiple transitions this results in the Blackbody spectrum. This process is well understood and almost all the radiation emitted is of thermal origin.

Nonthermal radiation is produced by charged particles interacting with electromagnetic fields, i.e. by the synchrotron and inverse Compton process. In the case of the synchrotron process relativistic leptons interact with magnetic fields, which force them onto a helical trajectory. The resulting accelerated motion causes the leptons to release part of their kinetic energy in form of electromagnetic radiation. In the Inverse Compton case the leptons interact with photons: whenever the lepton has sufficient kinetic energy compared to the photon, energy can be transferred from the lepton to the photon. Eventually, both processes can be understood as the interaction of electrons with external magnetic fields. In the case of synchrotron radiation a more or less static magnetic field provides the external field whereas in the case of the Compton process the electron interacts with an high-frequency electromagnetic wave. For ultrarelativistic astrophysical plasmas the Synchro self-comptonization process is often considered. Here, electrons interact with the synchrotron radiation of electrons in the same plasma. The inverse Compton process allows for an extensive energy gain of $\epsilon \sim \gamma^2$, where γ is the Lorentz factor of the electrons. In both cases the spectrum of the radiation strongly depends on the energy distribution of the electron population. Therefore, the spectrum provides a fundamental analysis tool that allows to obtain information about the energetic state of the plasma.

The astrophysical systems that produce nonthermal radiation are far away from thermodynamical equilibrium. They typically consist of relativistic plasma which naturally is accompanied by magnetic fields. In order to maintain the non-equilibrium

state some externally driven forces, like differential rotation, explosive flows or winds are required, which continuously feed energy into the system. These external forces are assumed to provide the source of turbulence, where the supplied energy is redistributed to smaller spatial scales, and eventually dissipates.

The continuous energy input by externally driven forces causes the magnetic energy to increase locally until the onset of magnetic reconnection is possible due to some non-ideality. Therefore magnetic reconnection can be regarded as a supercritical phenomenon that opens a dissipative channel through which the system can release its accumulated magnetic energy very rapidly. The released energy is converted into heat, plasma bulk motion and high-energy particle acceleration.

In the next sections we will outline the elementary physical processes that are relevant for our investigation. The order in that we address the processes is reverse to causality. First, we will outline the basics of the formation of synchrotron radiation in section 3.1 and address the issue of how the energy distribution of an electron population is related to the radiation spectrum. Then, we will cover the physical process responsible for the acceleration of electrons in our model, i.e. magnetic reconnection, in section 3.2. Eventually, in section 3.3 we will show how turbulence can be accounted for the onset of magnetic reconnection.

3.1 Synchrotron emission

The spectrum of radiation we observe from nonthermal astrophysical objects is an important source of information as it allows to draw conclusions about the energy distribution of the light emitting particles. The energy distribution in turn is a result of the underlying acceleration process which is the key point in our investigation. Nonthermal radiation from PWNe is produced by relativistic leptons moving in magnetic fields as the fraction of the protons can be neglected.

3.1.1 Radiation power

Every charged particle exhibits an electric field and as it is moving also creates a magnetic field. If the motion is accelerated the particle loses part of its energy in form of electromagnetic radiation. The total radiation power of a relativistic particle can be determined by integrating the Poynting vector over all solid angles and one arrives at

$$P = \frac{2q^2}{3c} \gamma^6 \left[\dot{\boldsymbol{\beta}}^2 - (\boldsymbol{\beta} \times \dot{\boldsymbol{\beta}})^2 \right], \quad (3.1)$$

where q is the particles' charge, c is the speed of light, γ is the Lorentz factor and $\boldsymbol{\beta} = \mathbf{v}/c$ the standardized velocity of the particle. Interestingly, the power does not depend on the particles kinetic energy for $\boldsymbol{\beta} \parallel \dot{\boldsymbol{\beta}}$ as it is the case in linear accelerators. The motion of an electron in a plasma is determined by the Lorentz force caused by the magnetic field \mathbf{B} which acts perpendicular to the velocity vector and forces the electron on a helical trajectory along the field lines. As a result, the radiation power

for ultrarelativistic electrons is essentially determined by the electron's energy and is given by

$$P = \frac{2}{3} r_e^2 c \beta^2 \gamma^2 B^2 \sin^2 \theta, \quad (3.2)$$

with the classical electron radius $r_e = e^2/m_e c^2$ and the pitch angle θ , which represents the angle between the velocity vector and the vector of the magnetic field at the electron's position.

The knowledge of the total radiation power allows for an estimation of the characteristic time at which the electron loses half of its kinetic energy. This is expressed by the cooling time

$$t_{cool} = \frac{3}{2} \frac{m_e^3 c^5}{e^4 \gamma B^2}. \quad (3.3)$$

Application to the Crab nebula with a magnetic field strength of 10^{-3} to 10^{-4} and an age of ~ 1000 years results in the conclusion that synchrotron lifetimes become less than the age of the nebula for electrons with Lorentz factors $\gamma \gtrsim 10^8$. This implies that these electrons cannot be a result of the initial explosion but must be continuously injected by the pulsar or accelerated inside the nebula.

3.1.2 Spectrum

In order to find the frequency dependency of the radiation the proper motion and the radiation characteristic of the electron must be taken into account. The former is described by the electron's relativistic equation of motion in an electromagnetic field

$$\frac{d(\gamma m \mathbf{v})}{dt} = \mathbf{F}_L = e \left(\mathbf{E} + \frac{1}{c} \mathbf{v} \times \mathbf{B} \right) \quad (3.4)$$

which is determined by the Lorentz force \mathbf{F}_L . In absence of an electric field and in a sufficiently homogeneous magnetic field, the electron moves along a helical trajectory that wraps around magnetic field lines, i.e. in a plane perpendicular to the magnetic field the electron moves along a circular path. The rotational frequency of this motion is given by the gyration frequency

$$\omega_G = \frac{eB}{\gamma m_e c}. \quad (3.5)$$

If we take an external electric field into account, the electric field component E_\perp perpendicular to the magnetic field leads to a drift motion of the gyration center with velocity $\mathbf{v}_D = c \mathbf{E} \times \mathbf{B} / B^2$, whereas the parallel component E_\parallel gives rise to an acceleration of the electron in direction of the magnetic field. Therefore, E_\parallel is the only way for the electron to gain energy in this simplified electromagnetic environment.

The radiation characteristic of a single electron in such a configuration is like that of a dipole but deformed in a way, that more radiation is emitted in the direction of motion. For ultrarelativistic electrons the emission is confined into a cone with an

axis orientated along the velocity vector. The opening angle ϑ of this cone is inversely proportional to the electron's Lorentz factor, i.e. $\vartheta \sim 1/\gamma$. Thus, the emission cone passes the observer with the gyration frequency ω_G , whereas the observed radiation pulse

$$\Delta t = \frac{2}{\gamma\omega_G} \left(1 - \frac{v}{c}\right) \approx \frac{1}{\gamma^3\omega_G} \quad (3.6)$$

is considerably shorter. This allows to define a critical radiation frequency

$$\nu_c = \frac{3}{2}\gamma^3\omega_G \sin\theta = \frac{3}{2}\frac{eB}{m_e c}\gamma^2 \sin\theta \quad (3.7)$$

at which the emission strongly declines. The additional factors $2/3$ and $\sin\theta$ result from the fact that the actual motion is not circular but helical.

Eventually, an accurate calculation (Rybicki & Lightman, 1979) results in the synchrotron spectrum of a *single* relativistic electron given by the total emissivity

$$J_{single}(\nu, \gamma, \theta)d\nu = \frac{\sqrt{3}e^3B}{m_e c^2} \sin\theta \frac{\nu d\nu}{\nu_c(\gamma, \theta)} \int_{\nu/\nu_c(\gamma, \theta)}^{\infty} K_{5/3}(\xi)d\xi, \quad (3.8)$$

where $K_{5/3}$ denotes the modified Bessel function of order $5/3$, which describes the frequency dependency. Integration over all frequencies results in the already known total radiation power given by equation (3.2).

In order to derive the spectrum J of an electron population one has to integrate $J_{single}(\nu, \gamma, \theta)$ over the Lorentz factor γ and the pitch angle θ with the corresponding distributions $N(\gamma)$ and $N(\theta)$:

$$J(\nu) = \int_{\gamma} \int_{\theta} J_{single}(\nu, \gamma, \theta) N(\gamma) d\gamma N(\theta) d\theta. \quad (3.9)$$

Let's assume a power law for the energy distribution $N(\gamma)d\gamma = \gamma^{-s}d\gamma$. Furthermore, in equation (3.2) we substitute the integration variable of the integral over the Bessel function with $x := \nu/\nu_c$, i.e. $\gamma \sim \sqrt{\nu/x}$ and $d\gamma \sim -\frac{1}{2}\nu^{1/2}x^{-3/2}$. In result we receive the total spectrum in form of

$$J(\nu) \sim \nu^{-\frac{s-1}{2}} \int_{x_2}^{x_1} x^{\frac{s-1}{2}} \int_x^{\infty} K_{\frac{5}{3}}(\xi)d\xi dx, \quad (3.10)$$

where the integration limits x_1 and x_2 correspond to the limits of the energy spectrum of the electrons γ_1 and γ_2 . In this estimation the pitch angle distribution was neglected as it does not depend on ν . The integrand of the x -integral declines rapidly for high values of x and ν . If the energy range $[\gamma_1, \gamma_2]$ is sufficiently wide, we therefore can consider the whole integral as constant and approximate the frequency dependency of the synchrotron spectrum with

$$J(\nu) \sim \nu^{-\frac{s-1}{2}}. \quad (3.11)$$

Thus, an electron population with energies characterized by a power law $N(\gamma)d\gamma = \gamma^{-s}d\gamma$ across a sufficiently large energy range, i.e. $\gamma_1 < \gamma < \gamma_2$ with $\gamma_1 \ll \gamma_2$, produces a power law synchrotron spectrum with spectral index

$$\alpha = \frac{s-1}{2}. \quad (3.12)$$

3.2 Magnetic reconnection

One of the fundamental properties of most large scale astrophysical plasmas is that they are collisionless and therefore have an extremely high conductivity. As a result, the magnetic field lines can be considered as frozen inside the plasma, i.e. the conditions for ideal MHD hold. Every plasma fluid element is connected to a certain field line and remains connected with that field line. The topology of the magnetic field is frozen into the plasma.

However, plasma bulk motions imply motions of magnetic field lines and that locally permits the increase of magnetic energy through shear and compression flows. The resulting strong local magnetic field gradients cause elementary electric currents to arise. The conditions for ideal MHD are locally violated due to the onset of a finite resistivity η , i.e. the non-ideal term in the context of the generalized Ohm's law

$$\mathbf{E} + \frac{1}{c}\mathbf{v} \times \mathbf{B} = \eta \frac{c}{4\pi} \nabla \times \mathbf{B} = \eta \mathbf{j} \neq 0 \quad (3.13)$$

becomes important. Metaphorically speaking, magnetic field lines detach from a fluid element and reconnect to another inside a localized reconnection zone, in which the ideal Ohm's law is violated according to equation (3.13). Magnetic reconnection can virtually be understood as a very fast diffusion of the magnetic field.

Fig. 3.1 illustrates the formation of a reconnection zone. The initial configuration consists of two regions, which are separated by a boundary layer at $x = 0$. The orientation of the magnetic field in one region is antiparallel to the other. Some external force causes plasma in both regions to flow towards the boundary layer within a certain volume of width L . Through the collisionless nature of the plasma, magnetic field lines are transported with this flow towards the boundary layer. Within a small localized region resistivity η arises. Resistivity is caused by increased Coulomb-collisions or, as in the case of anomalous resistivity, by momentum exchange of charged particles triggered by microturbulent electromagnetic fields resulting from plasma micro-instabilities. The onset of resistivity allows for the magnetic field to reconnect. The topology of the magnetic field changes and a separatrix is formed. Magnetic tension is then responsible for the pullout of plasma along the z-axis away from the reconnection zone, which in turn decreases the local pressure in that area. This causes more plasma to be pulled into the central region along the x-direction, resulting in a self-sustained cycle.

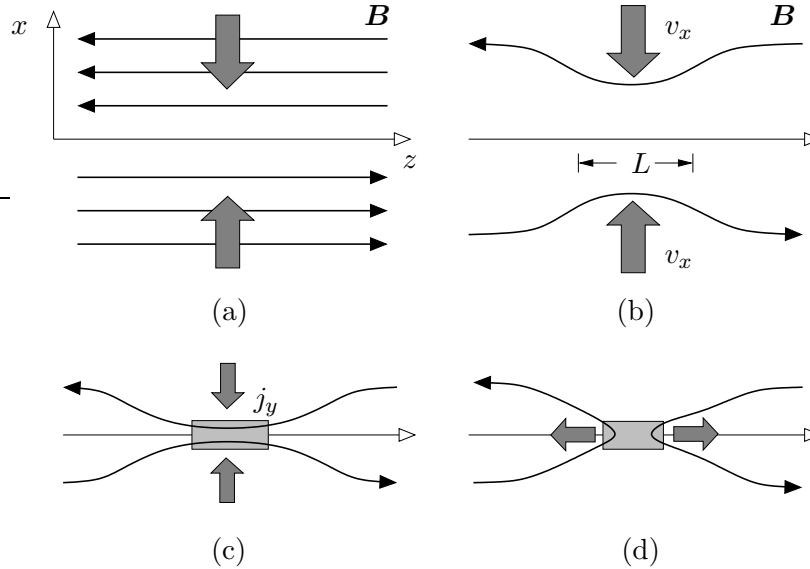


Figure 3.1: The formation of a reconnection zone: (a) Harris-sheet with contrarily orientated magnetic field lines in the x-y-plane at $x = 0$. (b) The plasma flows parallel to the x-axis and transports field lines into the boundary layer. (c) A diffusive region with $\eta \neq 0$ forms. (d) The topology of the magnetic field changes due to magnetic reconnection. Plasma is accelerated along the z-axis due to magnetic tension $(\mathbf{B} \cdot \nabla)\mathbf{B}$.

3.2.1 The tearing instability

A very prominent process in the treatment of magnetic reconnection is the tearing instability. It is very well investigated analytically (Furth, Killeen & Rosenbluth, 1963) and represents the prototype of spontaneous magnetic reconnection. Tearing modes also act as the perturbation to the Harris equilibrium in our numerical investigations, presented in chapter 5. Fig. 3.2 shows the initial and final magnetic configuration. The Harris-sheet is unstable against the tearing instability and evolves towards a configuration which consists of magnetic islands (O-points) and separatrices (X-points) along the current sheet. The current sheet tears up in X-points which are the site of magnetic reconnection and O-points which represent electric current carrying filaments.

As described in Section 3.1.2 an effective possibility for electrons to gain energy is the free fall through an electric potential caused by E_{\parallel} , the component of the electric field parallel to the magnetic field. The electrons then get accelerated along the magnetic field lines. By looking at the generalized Ohm's law (3.13) it becomes clear, that only in presence of resistivity η the electric field can have a parallel component. This holds true for the reconnection zones, which we consider to be the main sites of particle acceleration. In chapter 5 we address the mechanism of particle acceleration in fully evolved tearing configurations in greater detail and present the results of several numerical test particle runs. Our calculations show that such configurations are, in principle, capable to efficiently accelerate electrons.

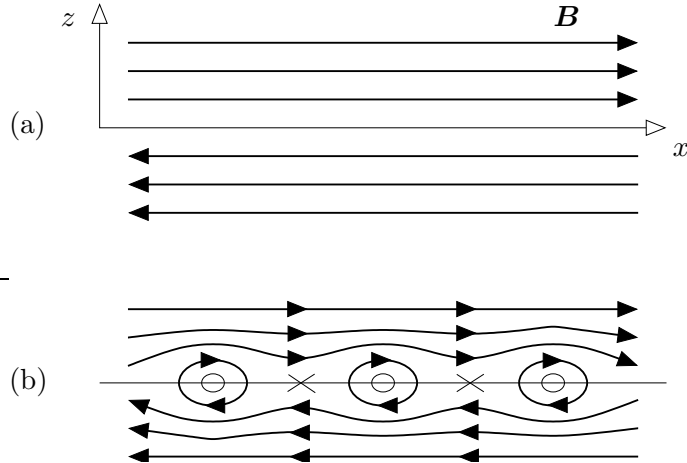


Figure 3.2: Tearing instability: (a) Harris-sheet. (b) Field topology of the fully evolved tearing mode.

Magnetic reconnection is presumed to occur in turbulent plasma flows because turbulent motions are capable of bringing magnetic fields of oppositely directed polarity into contact. Our contribution (Chapter 4) supports this idea as we observe the formation of regions with a substantial electric field component E_{\parallel} in a fully developed resistive MHD turbulence. These fields are associated with the local onset of resistivity and magnetic reconnection. We will address the issue of turbulence in the next section.

3.3 Turbulence

The problem of turbulence has occupied the attention of scientists for centuries. In a often quoted citation, turbulence is considered “the last great unsolved problem of classical physics”, variously attributed to one of the great modern physicists. There is a vital scientific and commercial interest of a greater understanding of turbulence since it plays a major role in several modern problems such weather forecasts, global climate modelling and magnetic confinement fusion research. Furthermore, turbulence can be considered the most common state of astrophysical flows, i.e. in systems like stellar winds, accretion disks, the interstellar medium, the intercluster medium and eventually in cosmology and the formation of galaxies. Hence, turbulence can be regarded as an universal phenomenon in fluid-like media on all length scales.

3.3.1 Incompressible turbulent hydrodynamic flows

Non-magnetized fluid-like systems are described by the velocity field \mathbf{v} , the mass density ρ and the pressure P , which are governed by the equations of mass and

momentum conservation

$$\frac{\partial \rho}{\partial t} + \nabla \cdot (\rho \mathbf{v}) = 0 \quad (3.14)$$

$$\frac{\partial \mathbf{v}}{\partial t} + (\mathbf{v} \cdot \nabla) \mathbf{v} = \mathbf{F} - \frac{1}{\rho} \nabla P + \nu \nabla^2 \mathbf{v}, \quad (3.15)$$

known as the continuity equation and Navier-Stokes equation, respectively. Here, \mathbf{F} is some unspecified external force and ν is the constant kinematic viscosity. Equations (3.14) and (3.15) provide, in principle, an adequate model for the behavior of an incompressible Newtonian fluid. The Navier-Stokes equation is deterministic and for sufficiently small velocities a solution can be found by perturbation analysis. However, if the flow involves high velocities, hydrodynamic turbulence arises because the non-linear advection operator $(\mathbf{v} \cdot \nabla) \mathbf{v}$ generates severe distortions of the velocity field by stretching, folding, and dilating fluid elements. In incompressible fluids these distortions can be damped, if the viscosity is sufficiently high, i.e. the advective term in the Navier-Stokes equation is balanced by the viscous term $\nu \nabla^2 \mathbf{v}$. By transferring equation (3.15) into a dimensionless form, one finds that the measure of this balance is given by the Reynolds number

$$Re = \frac{LV}{\nu}, \quad (3.16)$$

introducing the characteristic velocity V and length L of the flow. Thus, the Reynolds number represents the ratio of the advective term to the viscous term, or expressed in a more physical manner, the ratio of the viscous drag time (L^2/ν) to the eddy turnover time of a fluid element (L/V). Consequently, a hydrodynamic flow with a sufficiently large Reynolds number ($> 10^3$) can be regarded as turbulent.

The Navier-Stokes equation is in fact deterministic but the growth of perturbations lead to a loss of our predictive capability. Therefore one wishes to develop a statistical theory based on the average properties of turbulence, just as it can be done in thermodynamical systems. The traditional approach for incompressible turbulence is to derive equations for two- and three-point correlations together with various other ensemble averages. An obvious two-point correlation is the velocity correlation tensor $R_{ij} = \langle v'_i(\mathbf{x}) v'_j(\mathbf{x} + \mathbf{r}) \rangle$ which describes the correlation between velocity fluctuations \mathbf{v}' at different positions, separated by \mathbf{r} . Velocity fluctuations are defined as the difference to the ensemble averaged velocity $\langle \mathbf{v} \rangle$, i.e. $\mathbf{v} = \langle \mathbf{v} \rangle + \mathbf{v}'$. For $\mathbf{r} = 0$ it is reduced to the kinetic energy of the turbulence $v^2(\mathbf{x})$, whereas for $\mathbf{r} \rightarrow \infty$ the separated velocities will clearly have no correlation. The essential feature of turbulent flows confirms the presence of little, or in case of fully developed turbulence, no correlation between the various components of the density and velocity fields. Likewise, one can introduce correlation tensors of higher order for the purpose of reaching a general theory. However, this leads to a classical closure problem as equations for three-point correlations generate terms involving four-point correlations, and so forth.

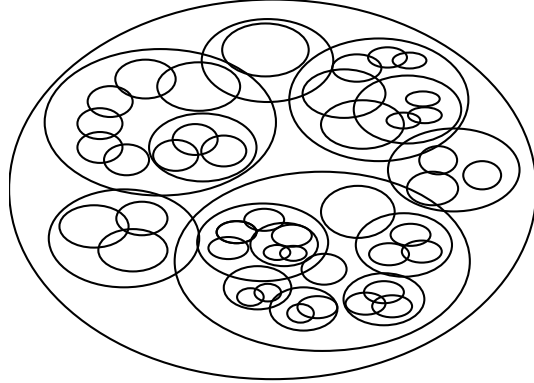


Figure 3.3: Schematic sketch of the hierarchical eddy cascade where large eddies contain smaller ones, and so on.

3.3.2 Kolmogorov theory

In thermodynamics one attempts to calculate the equilibrium energy distribution by assuming that the most probable distribution corresponds to the equilibrium. In contrast, turbulence can certainly not have an equilibrium distribution because turbulence inherently is a dissipative process. The total kinetic energy of an isolated turbulent system decreases with time due to viscous dissipation. Hence, a turbulent system can only be maintained in a steady state if energy is continuously fed into the system at the same rate as loss occurs due to dissipation. Such a system may then provide a close analogy to gases in a thermodynamical equilibrium. In the case of PWNe this energy is provided by the relativistic plasma wind generated by the fast rotating pulsar.

Kolmogorov (1941) proposed a theory to calculate the energy spectrum of such a homogeneous and isotropic turbulent system, maintained in a steady state by continuous energy input. He developed his phenomenological theory by introducing the hypothesis of self-similarity of the turbulent structures. Such a turbulent system can be thought of as consisting of many eddies of different sizes L and different velocities V . The largest eddies are generated by some external force \mathbf{F} , which give rise to a substantial advective part in the Navier-Stokes equation (3.15). The largest eddies generate smaller eddies which in turn create yet smaller eddies, and so forth. This idea corresponds to an energy cascade in wave number space, where the kinetic energy fed by external forces is redistributed from small wave number structures, represented by large eddies, to increasingly and larger wave number components, or smaller and smaller eddies. Eventually, the energy dissipates at a sufficient small length scale. The wave number range in which the energy is transported to smaller eddies is called *inertial range* because the advective term in the Navier-Stokes equation dominates what corresponds to inertia in the equation of motion.

Each eddy in the inertial range has a different size l and velocity v , corresponding

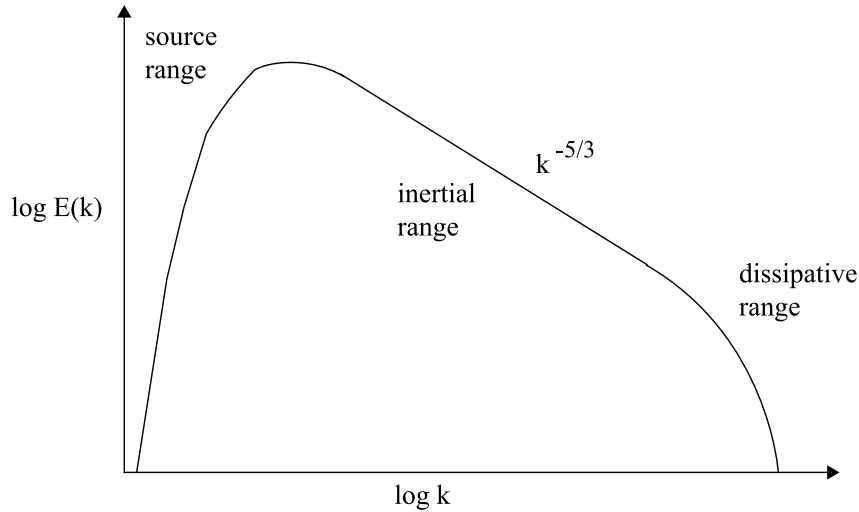


Figure 3.4: A typical Kolmogorov spectrum.

to a certain Reynolds number lv/ν , which is very high in the inertial range and of the order of unity in the dissipative range. The energy is fed into the system at an energy rate ϵ , which is transmitted from the largest to the smallest eddies. Kolmogorov's idea was that ϵ is only characterized by l and v . A dimensional analysis results in the proportionality $\epsilon \sim v^3/l$, which results in Kolmogorov's scaling law

$$v \sim (\epsilon l)^{1/3}. \quad (3.17)$$

This gives the velocity of the eddies at a certain length in the turbulent cascade. The dissipative range is defined by the fact that the Reynolds number is of order of unity, hence the size and the velocity of the smallest eddies are characterized by the viscosity: $l_d v_d \sim \nu$. Consequently, the Reynolds number Re associated with the largest eddies of size L and velocity V determines the size and velocity of the smallest eddies:

$$\frac{L}{l_d} \sim Re^{3/4}, \quad \frac{V}{v_d} \sim Re^{1/4}. \quad (3.18)$$

Kolmogorov's crucial assumption in the cascade theory was that the energy spectrum $E(k)$ does not depend on the properties of the medium, as turbulence spectra seem to appear universally. In particular, the spectrum should not depend on the viscosity, which can be regarded as a hidden parameter of the velocity field. On dimensional grounds again, the energy spectrum can only be of the form

$$E(k) = C\epsilon^{2/3}k^{-5/3}, \quad (3.19)$$

with a dimensionless constant C (experiments showed that this is of the order of unity). This expression is the famous turbulence energy spectrum that specifies the energy contained in eddies with $k \sim 1/l$.

Kolmogorov's analysis was kept purely hydrodynamical. Astrophysical flows however, are magnetized and the magnetic field has an important impact on the eddy motions and consequently on the energy spectrum. Interestingly, several astrophysical measurements are consistent with a Kolmogorov spectrum. For instance, Lazarian, Pogosyan & Esquivel (2002) found a Kolmogorov-type spectrum for the velocity fluctuations in HI regions in the Small Magellanic Cloud across pc and kpc scales.

3.3.3 MHD turbulence

An adequate description of a magnetized fluid must take the evolution of magnetic fields into account. Primarily, the force of the magnetic field on fluid elements has to be included, i.e. in equation (3.15) the magnetic body force must be added. Furthermore, an equation for the temporal evolution of the magnetic field is required. It can be accomplished using the induction equation, which is derived by substituting \mathbf{E} in the Maxwell equation $\partial\mathbf{B}/\partial t = -c\nabla \times \mathbf{E}$ from Ohm's law (3.13). As a result one obtains the hydromagnetic equations

$$\frac{\partial\mathbf{v}}{\partial t} + (\mathbf{v} \cdot \nabla)\mathbf{v} = \mathbf{F} - \frac{1}{\rho}\nabla P + \frac{1}{4\pi\rho}(\nabla \times \mathbf{B}) \times \mathbf{B} + \nu\nabla^2\mathbf{v} \quad (3.20)$$

$$\frac{\partial\mathbf{B}}{\partial t} = \nabla \times (\mathbf{v} \times \mathbf{B}) + \lambda\nabla^2\mathbf{B}, \quad (3.21)$$

where $\lambda = \eta\frac{c^2}{4\pi}$ represents the magnetic diffusion.

With regard to a theory of turbulence for magnetized fluids, it is helpful to point out that the induction equation (3.21) is an exact analogon of the vorticity equation

$$\frac{\partial\boldsymbol{\omega}}{\partial t} = \nabla \times (\mathbf{v} \times \boldsymbol{\omega}) + \nu\nabla^2\boldsymbol{\omega} \quad (3.22)$$

for incompressible fluids, which is obtained by taking the curl of the Navier-Stokes equation (3.15) and applying the substitution $\boldsymbol{\omega} = \nabla \times \mathbf{v}$. The vorticity equation and the definition of the vorticity $\boldsymbol{\omega}$, together with the assumption of incompressibility which states that the divergence of the velocity field $\nabla \cdot \mathbf{v} = 0$, provide an alternative complete dynamical theory of incompressible hydrodynamic fluids.

A further approach to illustrate the symmetry between the velocity and the magnetic field is Elsasser's (1950) form of the hydromagnetic equations

$$\begin{aligned} \left(\frac{\partial}{\partial t} + \mathbf{z} \cdot \nabla\right)\mathbf{w} &= \nu_+\nabla^2\mathbf{w} + \nu_-\nabla^2\mathbf{z} - \nabla p, & \nabla \cdot \mathbf{w} &= 0 \\ \left(\frac{\partial}{\partial t} + \mathbf{w} \cdot \nabla\right)\mathbf{z} &= \nu_+\nabla^2\mathbf{z} + \nu_-\nabla^2\mathbf{w} - \nabla p, & \nabla \cdot \mathbf{z} &= 0, \end{aligned} \quad (3.23)$$

where $\mathbf{w} = \mathbf{v} + \mathbf{b}$, $\mathbf{z} = \mathbf{v} - \mathbf{b}$, $\nu_+ = \frac{1}{2}(\nu + 1/4\pi\rho)$, $\nu_- = \frac{1}{2}(\nu - \lambda)$, $\mathbf{b} = \mathbf{B}/\sqrt{4\pi\rho}$ and $p = P/\rho$. These equations will no doubt give rise to a turbulent magnetic field

coupled with the mechanical motion. Thus, there is a similar dimensionless number for the magnetic aspect of plasmas called the magnetic Reynolds number

$$Rm = \frac{LV}{\lambda}, \quad (3.24)$$

which can be understood as the ratio of the magnetic field decay time (L^2/λ) to the eddy turnover time (L/V). The magnetic decay time represents the time scale on which the magnetic field would decay by Ohmic dissipation in absence of the source term. Again, the magnetic Reynolds number can be regarded as the ratio of the source term to the dissipative term in the induction equation. It measures the tendency of magnetic turbulence.

Iroshnikov (1963) and Kraichnan (1965) made attempts to describe magnetic turbulence statistics in a similar manner as Kolmogorov. In their model they assume a homogeneous isotropic configuration with a uniform external magnetic field B_0 . The magnetic counterparts to velocity fluctuations are Alfvén waves which travel along the magnetic field lines at the Alfvén speed $v_A = B_0/\sqrt{4\pi\rho}$. The essential difference between velocity fluctuations in hydrodynamic flows and magnetic fluctuations in plasmas is, that the magnetic fluctuations can only propagate along the field lines. In order to initiate turbulence there must be wave packets that travel in opposite directions. A magnetic energy cascade occurs when such wave packets collide. The Iroshnikov-Kraichnan turbulence theory gives an estimation of the energy that is transferred to smaller scales:

$$\epsilon \sim \frac{v^3}{v_A}, \quad (3.25)$$

where v represents the velocity fluctuation. A dimensional analysis then yields

$$E(k) = A\sqrt{\epsilon v_A} k^{-2/3}, \quad (3.26)$$

where A is a numerical constant. Thus, in the Iroshnikov-Kraichnan theory turbulent magnetized fluids offer a considerably flatter energy spectrum than hydrodynamical fluids in the Kolmogorov model.

More sophisticated theories have been developed, such as the direct interaction approximation (Kraichnan, 1959) for isotropic hydrodynamic turbulence, the eddy-damped quasinormal Markovian (EDQNM) approximation (Orszag, 1979), and the renormalization group technique (Verma, 1999). The Kolmogorov and Iroshnikov-Kraichnan theories, however, have the advantage of being very intuitive and vivid. By using similarity arguments, they give a rough estimate of the structure and energy spectrum of homogeneous, isotropic, incompressible unmagnetized and magnetized turbulent fluids. The Iroshnikov-Kraichnan theory fails for plasmas with clear anisotropy, i.e. elongated eddies that extend along magnetic field lines. Models for anisotropic plasmas usually consider three-wave interactions where the orientation of the magnetic field has to be incorporated. A further aspect, which is regarded by more recent investigations, is the intermittency of the dissipative structures, which refers to the non-uniform distribution of the structures. Intermittency has an important dynamical consequence as it affects the energy spectrum. While there exist

several theories that describe incompressible MHD turbulence well, no universally accepted theory exists for compressible MHD turbulence.

An interesting feature of turbulence has been found by laboratory studies on hydrodynamic turbulence as they revealed the existence of persistent structures within turbulent flows. Such a persistent structure represents a connected, large-scale turbulent fluid mass with a phase-correlated vorticity over its spatial extent (Hussain, 1983; 1986). These structures do not disappear into microscopic dissipative scales but persist and are advected by the flow, feeding turbulence far away from the source region. Persistent structures merge with others or tear apart. They are of particular interest with respect to astrophysical objects like extragalactic jets or PWNe, where similar structures can be observed.

In the next chapter we present the results of our investigation on particle acceleration in PWNe. The plasma nebula is modeled in a resistive, compressible way. The development of resistive regions is observed, which gives rise to the onset of magnetic reconnection. Successive relativistic test particle simulations in the electromagnetic environment resulting from the MHD simulations show a similar synchrotron spectrum to that observed in the Crab nebula.

Chapter 4

Radio emission and particle acceleration in plerionic supernova remnants¹

NODES, C., BIRK, G.T., GRITSCHNEDER, M. & LESCH, H.

Abstract: Plerionic supernova remnants exhibit radio emission with remarkably flat spectral indices ranging from $\alpha = 0.0$ to $\alpha = -0.3$. The origin of very hard particle energy distributions still awaits an explanation, since shock waves generate particle distributions with synchrotron spectra characterized by $\alpha \leq -0.5$. Acceleration of high energy leptons in magnetohydrodynamic turbulence instead may be responsible for the observed hard spectra. This process is studied by means of relativistic test particle calculations using electromagnetic fields produced by three-dimensional simulations of resistive magnetohydrodynamical turbulence. The particles receive power-law energy spectra $N(\gamma) \propto \gamma^{-s}$ with s ranging from 1.2 to 1.6, i.e. particle spectra that are required to explain the radio emission of plerions.

4.1 Introduction

Filled-center supernova remnants (SNR), or plerions exhibit flat radio spectra, with power-law indices $0 \leq \alpha \leq 0.3$ (for $S_\nu \propto \nu^{-\alpha}$) (Weiler & Panagia 1978; Weiler & Shaver 1978). Such spectra require energy distributions of the electrons $N(\gamma) \propto \gamma^{-s}$ with $s = 1 + 2\alpha$ be in the range $1 \leq s \leq 1.6$. The flatness of their radio spectra distinguishes plerions from a typical shell-type SNR with a mean $\alpha \sim 0.5$ implying $N(\gamma) \propto \gamma^{-2}$ (e.g. Green 1991). The origin of relativistic electrons responsible for these unusual radio spectra of plerions is not yet understood (e.g. Green 1992; Woltjer *et al.* 1997; Arons 1998).

¹Nodes *et al.* 2004

Although the many details of the nature and structure of plerions are still unclear (see Arons 1998; Salvati *et al.* 1998; Bandiera 2002 for reviews) there is a consensus on the following scenario: Plerions are expanding bubbles, filled with magnetic fields and relativistic leptons. Both components are continuously supplied to the nebula by some central source, i.e. by a rotating neutron star in form of a strongly magnetized wind whose energy is at least partially dissipated in termination shock waves (Kennel & Coroniti 1984a, 1984b; Galant & Arons 1994).

Arons (1998) discussed the difficulties of particle acceleration in plerions in great detail. With respect to prototypic Crab nebula he pointed out that the emission at high frequencies (from the optical towards X- and γ -rays) diagnoses the coupling physics *today* since the synchrotron loss times of the high energy particles are significantly smaller than the lifetime of the nebula. The radio emission instead measures the integral of the pulsars input over the entire history of the nebula - most of the stored relativistic energy is in magnetic fields and radio emitting particles (about 10^{50} ergs). Arons noted that averaged over the whole nebula, the radio emitting spectrum has the form $N(\gamma) \propto \gamma^{-1.5}$, $10^{2.5} \leq \gamma \leq 10^4$ based on the detailed spectral index maps by Bietenholz & Kronberg (1992) which show the particle distribution to be remarkably homogeneous. The origin for this energy distribution is not clear since the wind termination shock wave models do not yield power laws flatter than $N(\gamma) \propto \gamma^{-2}$ at energies small compared to $\gamma \sim 10^6$. Arons speculated that some additional acceleration physics by magnetohydrodynamic (MHD) waves may have to be included.

Bandiera *et al.* (2002) mapped the Crab Nebula at 230 GHz and compared it to the 1.4 GHz map. The spectral index in the inner region at 230 GHz is flatter (by ~ 0.05) than in the rest of the nebula. Furthermore they found a steepening of the spectrum at the places of radio emitting filaments, concluding that the magnetic field strengths in the filaments is higher than in the surrounding nebula. Some evidence for in-situ acceleration in the Crab nebula has been collected by the radio observations of Bietenholz, Frail & Hester (2001).

It is the aim of our contribution to show that resistive magnetohydrodynamical fluctuations excited to a highly turbulent level accelerate test particles to energy distributions with power law indices $1 \leq s \leq 1.6$ being in good agreement with the radio observations of plerions. We also show that an increase in particle density as can be expected for the filaments lead to a steepening of the particle spectrum. Given the fact, that central sources energize the nebula, thereby exciting strong MHD fluctuations we think that our simulations may shed some light on the probably necessary additional acceleration physics as speculated by Arons (1998).

In the next section we describe the MHD simulations. Section 4.3 contains the results of relativistic particle simulations including radiative synchrotron losses and finally we discuss our findings in Section 4

4.2 Reconnective MHD turbulence

Pulsars permanently power their environment by radiation and, in particular, pulsar plasma winds. In fact, in the case of the Crab nebula the permanent energy input by plasma flow is about 10^{38} erg/s. This plasma flow encounters the termination shock at radius $R_s \approx 10^{17}$ cm where it gets decelerated and leptons are accelerated to ultra-relativistic energies. Most of their synchrotron radiation is emitted in the optical to γ -ray band. The presence of this termination shock is accompanied by strong excitation of Alfvén waves which are expected to excite strong MHD turbulence in the pulsar's nebula (Kronberg *et al.* 1993). In this picture the size of the turbulence cells in the nebula is limited by R_s . The projected magnetic field within the Crab nebula was found to have a coherence length of about 10^{16} cm (Bietenholz & Kronberg 1992). Kronberg *et al.* (1993) suggested that the fact that this length scale is close to the inner shock radius R_s , may be more than coincidental. Laboratory studies of turbulent flows have revealed the existence of persistence structures, which are advected in the flow and exhibit sizes comparable to the source size (Hussain 1983, 1986). In other words, the source of turbulence within a supernova remnant is given by a shock wave, like in the Crab nebula, the spatial scale of the shock is the maximum length scale for turbulence within the nebula. To be precise, in the Crab nebula the characteristic size of the turbulence should be smaller than 10^{17} cm.

The associated MHD turbulence can be numerically generated by means of the so-called Orszag-Tang turbulence (Orszag & Tang 1979). The Orszag-Tang initial condition is a generic way to excite turbulence in a magnetized plasma and is given by the non-linear interaction of Alfvén waves which are MHD eigenmodes of a magnetized fluid e.g.,

$$B_x = -B_0 \sin [2\pi(y - y_{\min})/(y_{\max} - y_{\min})] \sin [2\pi(z - z_{\min})/(z_{\max} - z_{\min})] \quad (4.1)$$

$$B_y = B_0 \sin [4\pi(x - x_{\min})/(x_{\max} - x_{\min})] \sin [2\pi(z - z_{\min})/(z_{\max} - z_{\min})] \quad (4.2)$$

$$B_z = B_0 \sin [4\pi(x - x_{\min})/(x_{\max} - x_{\min})] \sin [2\pi(y - y_{\min})/(y_{\max} - y_{\min})] \quad (4.3)$$

$$v_x = -v_0 \sin [2\pi(y - y_{\min})/(y_{\max} - y_{\min})] \sin [2\pi(z - z_{\min})/(z_{\max} - z_{\min})] \quad (4.4)$$

$$v_y = v_0 \sin [2\pi(x - x_{\min})/(x_{\max} - x_{\min})] \sin [2\pi(z - z_{\min})/(z_{\max} - z_{\min})] \quad (4.5)$$

$$v_z = 0 \quad (4.6)$$

The amplitudes are chosen as $B_0 = 5.5 \times 10^{-3}$ G and $v_0 = 0.05, 0.016, 0.005, 0.0016, 0.0005, 0.00016$ c for the six different test particle runs discussed in section 4.3.

The nonlinear interaction of the Alfvénic perturbations result in almost homogeneous turbulence. We use periodic boundary conditions in all directions and a

numerical box given by $x_{\min}, y_{\min}, z_{\min} = -0.5 \times 10^{16}$ cm and $x_{\max}, y_{\max}, z_{\max} = 0.5 \times 10^{16}$ cm with a resolution of 101^3 grid points.

We model this kind of turbulence by means of a well approved resistive compressible 3D MHD code (Otto 1990). It integrates the balance equations that govern the macroscopic low-frequency dynamics which read

$$\frac{\partial \rho}{\partial t} + \nabla \cdot (\rho \mathbf{v}) = 0 \quad (4.7)$$

$$\frac{\partial \rho \mathbf{v}}{\partial t} + \nabla \cdot (\rho \mathbf{v} \mathbf{v}) = -\nabla p + \frac{1}{4\pi} (\nabla \times \mathbf{B}) \times \mathbf{B} \quad (4.8)$$

$$\frac{\partial p}{\partial t} = -\mathbf{v} \cdot \nabla p - \gamma p \nabla \cdot \mathbf{v} + (\gamma - 1) \eta (\nabla \times \mathbf{B})^2 \quad (4.9)$$

$$\frac{1}{c} \frac{\partial \mathbf{B}}{\partial t} = \nabla \times \frac{1}{c} (\mathbf{v} \times \mathbf{B}) - \frac{c}{4\pi} \nabla \times (\eta \nabla \times \mathbf{B}) \quad (4.10)$$

where ρ , \mathbf{v} , p , and \mathbf{B} denote the mass density, bulk velocity, thermal pressure, and the magnetic field. By η the resistivity is denoted.

Reconnection is allowed due to a microturbulent resistivity which is modeled in a current dependent way. The motivation for this kind of resistivity is the following: In the highly turbulent almost ideal plasma of the nebula collisional resistivity is negligible. Rather a wide variety of micro-instabilities driven by electric currents is responsible for localized dissipation. For strong turbulence the amplitude of the resistivity is given by $\eta \approx m_e \omega_e / ne^2$, where $\omega_e = \sqrt{4\pi ne^2 / m_e}$ is the electron plasma frequency (Vasyliunas 1975). This kind of resistivity is assumed for our simulations.

As a result of the resistive MHD calculations we get a turbulent field configuration which we use for the test particle simulations. Fig. 4.1 and 4.2 show the magnetic energy density and the magnetic field lines. These figures are to illustrate the turbulent structure of the magnetic field. Fig. 4.3 shows the reconnection regions, i.e. places where the parallel component of the electric field is appreciable high. These are the acceleration sites where we expect the particles to gain energy. They are also distributed in a very stochastic way clearly indicating the turbulent nature of our fields.

4.3 Relativistic particle simulations

The MHD calculations described in the previous section are used as the electromagnetic environment for the studies of electron acceleration by means of test particle simulations. We want to know how electric particles behave in the complex three-dimensional turbulent electro-magnetic field configuration, in particular how their energy distribution develops.

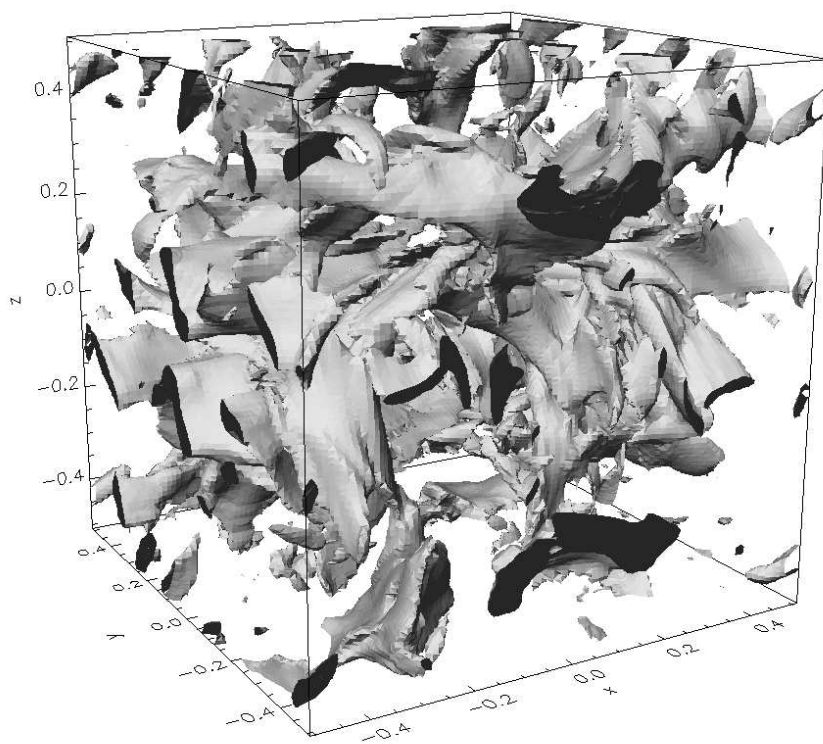


Figure 4.1: 3D Isosurface plot of the magnetic energy density. The shaded volume surface corresponds to a magnetic energy density of $u_{\text{magn}} \approx 2.5 \times 10^{-11}$ erg/cm³. The spatial extension is given in units of 10^{16} cm.

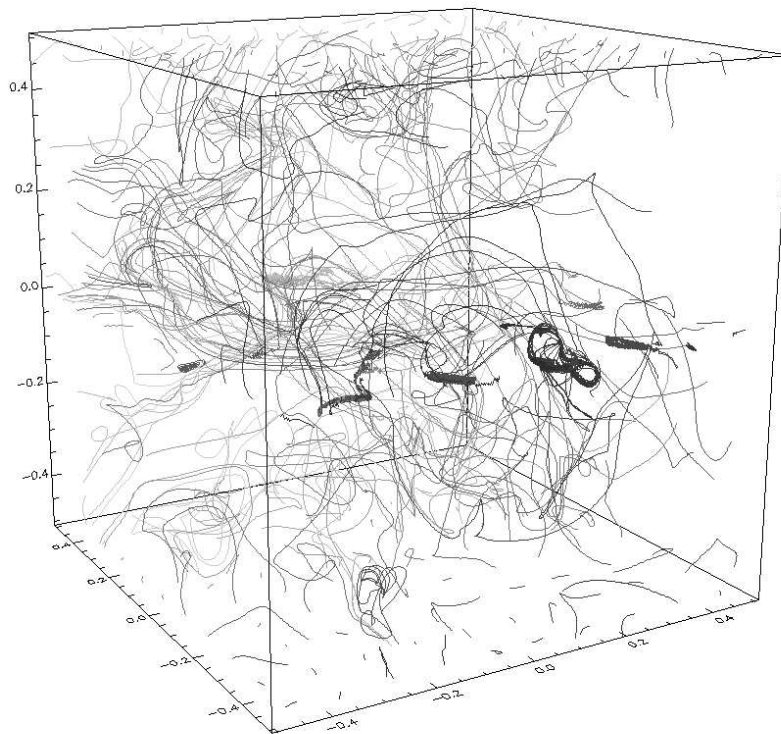


Figure 4.2: Magnetic field lines.

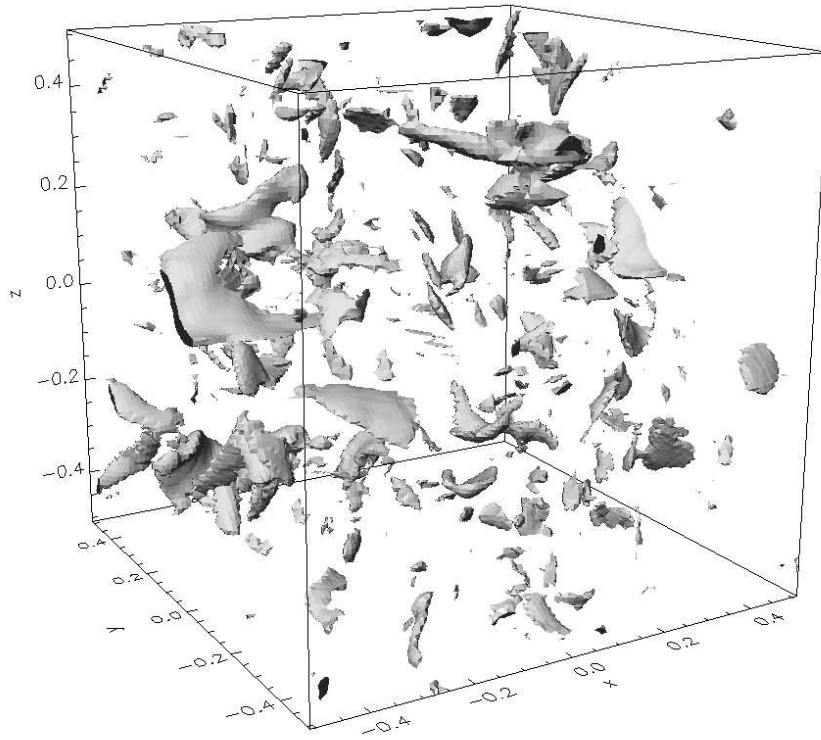


Figure 4.3: Reconnection regions, i.e. regions with appreciable value of E_{\parallel} . The shaded volume surface corresponds to a value of $E_{\parallel} \approx 1.3 \times 10^{-6}, 4 \times 10^{-7}, 1.3 \times 10^{-7}, 4 \times 10^{-8}, 1.3 \times 10^{-8}, 4 \times 10^{-9}$ statvolt/cm for the six different test particle runs.

The electric field is derived from the MHD quantities \mathbf{B} , \mathbf{v} and η by means of the normalized Ohm's law

$$\mathbf{E} = -\frac{1}{c}\mathbf{v} \times \mathbf{B} + \frac{c}{4\pi}\eta\nabla \times \mathbf{B}, \quad (4.11)$$

and gives for the mean value of of the electric field $\overline{E} \approx 0.02 \overline{B}$. Equation (4.11) states that a parallel component of the electric field E_{\parallel} only occurs for $\eta \neq 0$. Compared to the mean perpendicular component \overline{E}_{\perp} the mean parallel component in our simulations is found to be $\overline{E}_{\parallel} \approx 0.04 \overline{E}_{\perp}$.

The results of the MHD calculation are scaled to model different physical conditions, i.e. different mass densities inside the nebula, and are then used for the test particle simulations. Here we present the results of particle simulations for six different mean mass densities $\overline{\rho} = 10^n m_p/cm^3$, $n = -2, -1, 0, 1, 2, 3$ (corresponding to the initial v_0). The mean magnetic field strength for all runs was chosen to be $\overline{B} = 3 \times 10^{-4}$ G.

Since the data for the electric and magnetic field is only available on a discrete three-dimensional grid the test particle code uses linear interpolation to determine the field values for any location. We note that the term "test particle" means that the electromagnetic fields produced by the particles are not changing the global fields, though the effect of synchrotron radiation on the motion of the particles is taken into account, i.e. the relativistic equations of motion have the form

$$\frac{d\mathbf{p}}{dt} = q \left(\mathbf{E} + \frac{1}{\gamma mc} \mathbf{p} \times \mathbf{B} \right) + \mathbf{F}_{Rad}, \quad \frac{d\mathbf{r}}{dt} = \frac{\mathbf{p}}{\gamma m}, \quad (4.12)$$

where m and q denote the mass and charge of the particles, which are electrons in our case and

$$\gamma = \sqrt{1 + \left(\frac{p}{mc} \right)^2} \quad (4.13)$$

is the Lorentz factor.

The calculations are relativistic, including the energy losses via synchrotron radiation and inverse Compton scattering by (Landau & Lifshitz 1951)

$$\begin{aligned} \mathbf{F}_{Rad} \approx & \frac{2}{3} \frac{q^4}{m^2 c^4} \left\{ \mathbf{E} \times \mathbf{B} + \frac{1}{c} \mathbf{B} \times (\mathbf{B} \times \mathbf{v}) + \frac{1}{c} \mathbf{E} (\mathbf{E} \cdot \mathbf{v}) \right\} \\ & - \frac{2}{3} \frac{q^4}{m^2 c^5} \gamma^2 \mathbf{v} \left\{ \left(\mathbf{E} + \frac{1}{c} \mathbf{v} \times \mathbf{B} \right)^2 - \frac{1}{c^2} (\mathbf{E} \cdot \mathbf{v})^2 \right\} \end{aligned} \quad (4.14)$$

The equations are numerically integrated by a Runge-Kutta algorithm of fourth order with an adaptive stepsize control. As a result we get the momentum and location at certain times of each particle in the given ensemble. The codes has been used before to study high-energy particle acceleration (Nodes et al. 2003; Schopper *et al.* 1999).

The direction of the initial momentum vector is equally distributed in a cone of opening angle 80° at the bottom of the box. This initial condition corresponds to the

idea that the electrons enter the turbulent region moving in a well defined direction. The notion "final state" relates to a set of particles in which each individual particle has left the computational box.

The simulations start off with electrons injected into the computational box at $z = z_{\min}$. We use a powerlaw E_{kin}^{-2} ranging from 10^2 to $10^4 m_e c^2$ as the initial energy spectrum for all calculations. The choice of this injection spectrum was motivated by our synchrotron model for the infrared to X-ray emission of the Crab pulsar (Crusius-Wätzel, Kunzl & Lesch 2001). There we could show that the emission of the neutron star could be explained with a single energy distribution $N(E) \propto E_{\text{kin}}^{-2}$. We could also show that such an energy distribution is naturally produced in an efficient pair cascade. Given that plerions in general are powered by a pulsar like in the case of the Crab nebula, an energy distribution $\propto E_{\text{kin}}^{-2}$ seems a quite reasonable choice as a probable injection spectrum in turbulent plasmas of a plerionic supernova remnant.

Another series of simulations we performed showed clearly that the resulting energy spectrum is independent of the index of the initial energy distribution. Also the initial energy range does not play a crucial role for the final distribution. After the initial injection of the electrons they get accelerated very rapidly and their energy distribution reaches a stationary state. This happens within only a few days and then the distribution remains for several years until the final state is reached. For different initial distributions only this first acceleration phase gets shorter or longer but the final distribution is given by the energy offered by the MHD fields. Thus, even for a non-relativistic initial energy distribution we expect the final spectral index to be the same as the one found in the relativistic runs.

Fig. 4.4 shows the initial and the final energy spectra of the test particle runs for different values of the mean mass density $\bar{\rho}$. The calculations show that for all values of $\bar{\rho}$ the spectrum gets flatter than the initial spectrum which means that particles are accelerated. Compared to the initial spectrum the low energetic electrons get redistributed to higher energies, i.e. the low energy peak of the initial spectrum is reduced.

The cut-off energy in the spectrum is correlated with the maximum energy that the electrons can gain from the mean parallel component of the electric field $E_{\text{kin}}^{\text{max}} = el\bar{E}_{\parallel}$, where l is the length of the computational box.

The final energy spectra can be approximated by a broken power law consisting of two parts: a low energy part which has a relatively flat gradient and a steeper high energy part. Basically the latter part of the spectrum is responsible for the synchrotron radiation therefore we will only consider this part.

For the first run, the one with the lowest density $\bar{\rho}$ we get a spectral index of -1.19 for the high energy part above energies of $\gamma \approx 4.0 \cdot 10^3$. The spectral index s decreases with increasing $\bar{\rho}$ (approximately by a logarithmic relation), i.e. the spectrum gets steeper for denser regions. This result corresponds well with the observed steepening of the radio spectrum at places of magnetic filaments.

The resulting synchrotron spectrum can be calculated as the sum of total power per frequency emitted by each individual electron. The latter is given by Rybicki &

4.3 RELATIVISTIC PARTICLE SIMULATIONS

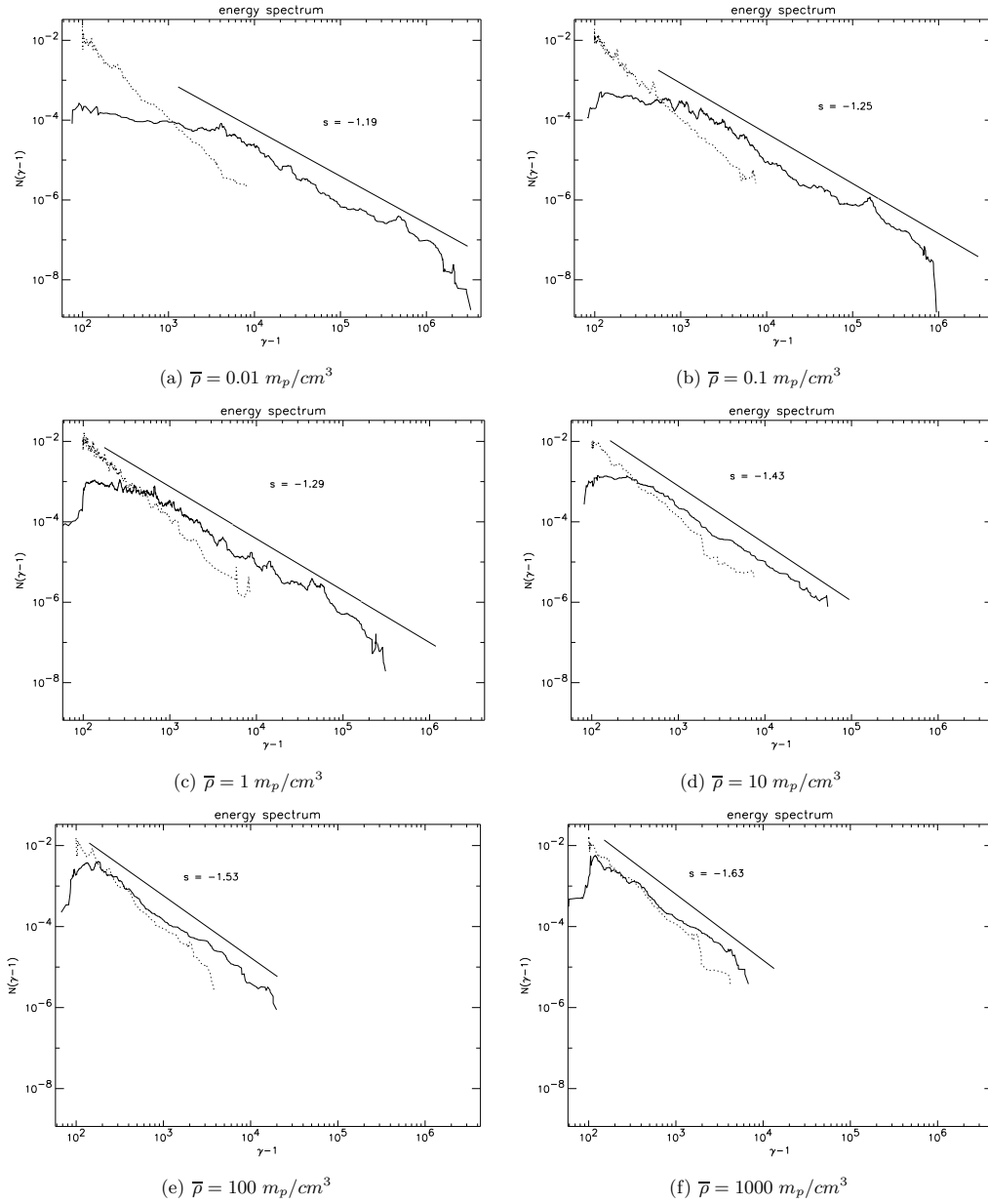


Figure 4.4: The initial (dotted line) and final (solid line) energy spectrum of the test particle simulations for different values of the mass density ($\bar{\rho} = 10^n m_p/cm^3$, $n = -2, -1, 0, 1, 2, 3$). A least squares fit of the spectrum in a certain energy range is plotted above the spectrum and is labeled with the spectral index s .

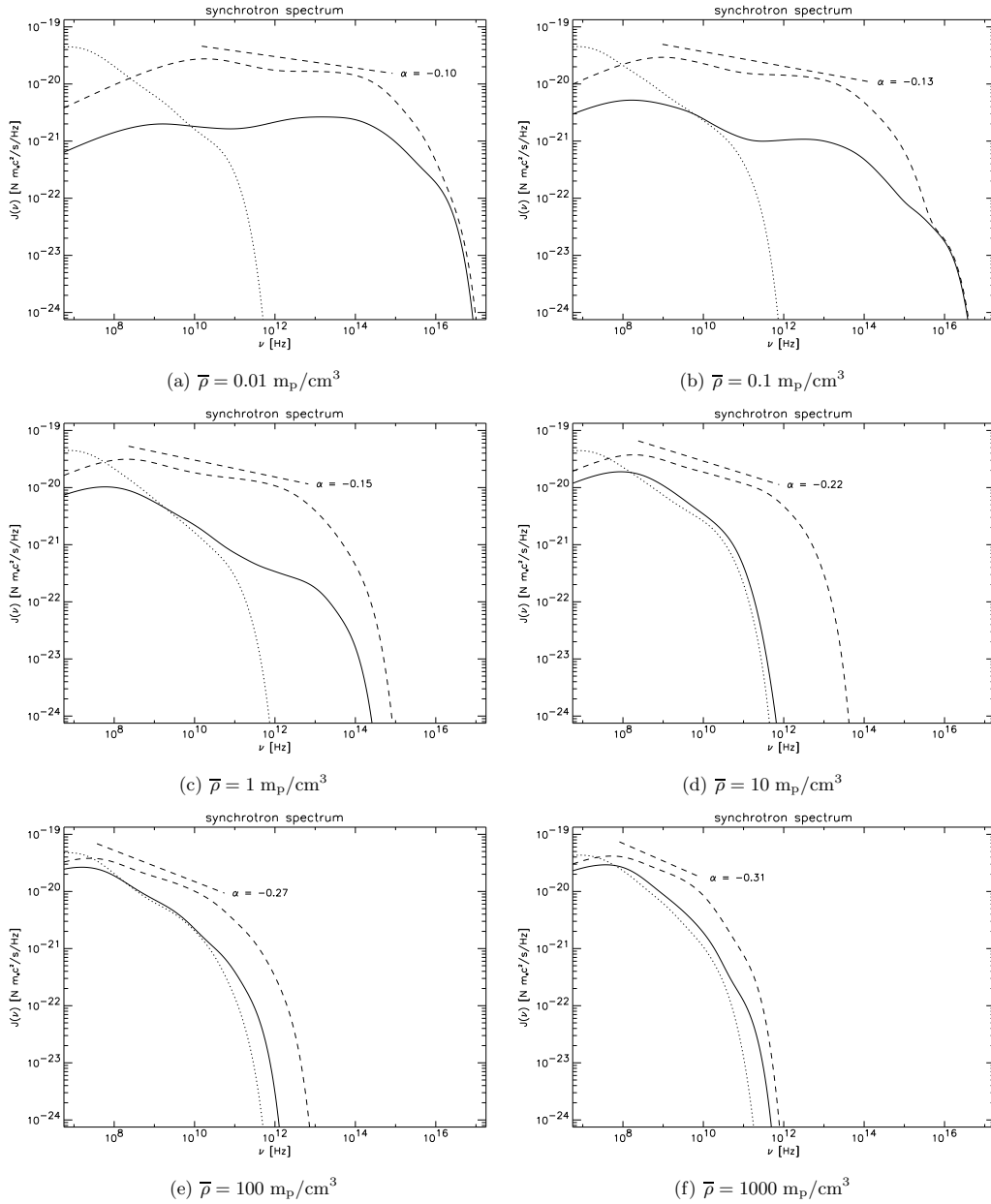


Figure 4.5: The initial (dotted line) and the final (solid line) synchrotron spectrum of all runs calculated as the sum of the individual synchrotron spectra of the corresponding electrons (equation (4.15)). The dashed line depicts the final synchrotron spectrum of a electron population with isotropic pitch angle distribution. The power per unit frequency $J(\nu)$ is normalized to the total rest mass energy $N mc^2$ of the set of electrons, where N is the number of all electrons.

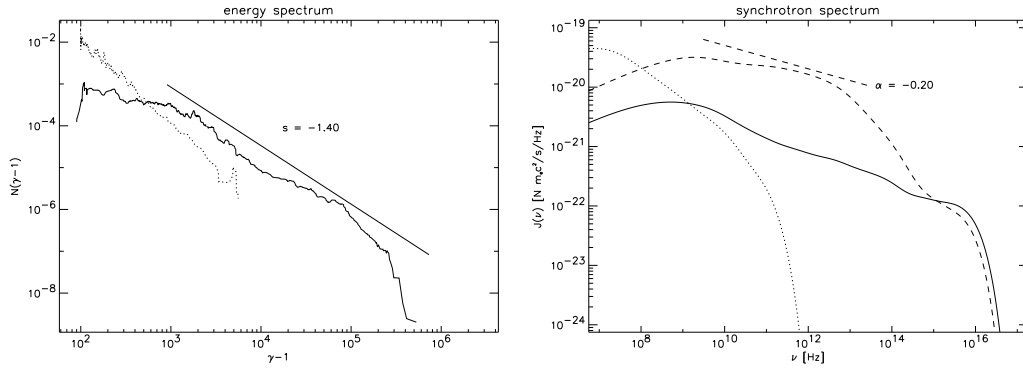


Figure 4.6: Particle energy and synchrotron spectra of a single run with $E_{\parallel} = 0$. The value for the mean density in this run is the same as in the first run in Fig. 4.4 and Fig. 4.5 ($\bar{\rho} = 10^{-2} m_p/cm^3$). Due to the lower mean electric field energy the achieved energy levels are lower.

Lightman 1979

$$J\left(\frac{\nu}{\nu_c}\right) = \frac{\sqrt{3}e^3}{mc^2} B \sin\theta \frac{\nu}{\nu_c} \int_{\nu/\nu_c}^{\infty} K_{5/3}(\xi) d\xi, \quad (4.15)$$

where $\nu_c = \frac{3}{4\pi} \frac{e}{mc} B \gamma^2 \sin\theta$ is the critical frequency, θ is the pitch angle and $K_{5/3}$ is the modified Bessel function of order 5/3. Fig. 4.5 shows the synchrotron spectra of the high energy particles calculated for the "real" pitch angle distribution taken from our simulation and a isotropic pitch angle distribution. The isotropic distribution leads to a synchrotron spectrum with spectral index $\alpha = (s - 1)/2$ where s is the index of the energy spectrum. This means that the steepening of the energy spectrum with increasing density results in a steepening of the synchrotron spectrum.

The actual final pitch angle distributions in our simulations are clearly anisotropic. In the low density runs the pitch angle distributions offer a peak at $\sin\theta \approx 0.01$. Since $J(\nu) \sim \sin\theta$ the total radiation power emitted is lower as compared to the isotropic case (Fig. 4.5). The pitch angle is also correlated with the gained energy, i.e. the highest energetic particles have the lowest pitch angles. This correlation results from the acceleration along the magnetic field lines for which the parallel component of the electric field $E_{\parallel} = (\eta \nabla \times \mathbf{B})_{\parallel}$ is responsible. E_{\parallel} can only be found at places with significant value of η . Contrary to second-order acceleration processes the acceleration due to magnetic reconnection is able to explain the observed spectra by particle acceleration in turbulence. To prove the efficiency of acceleration in presence of parallel electric fields we performed a test particle run without any E_{\parallel} .

Fig. 4.6 shows the results of a run that is similar to the first run in Fig. 4.4 and Fig. 4.5 with the modification $E_{\parallel} = 0$. The resulting spectra are considerably steeper, since the acceleration is less efficient as in the case with reconnection. Therefore the presence of parallel electric fields is crucial to explain the observed flat spectra. This result is also corroborated by particle simulations starting from

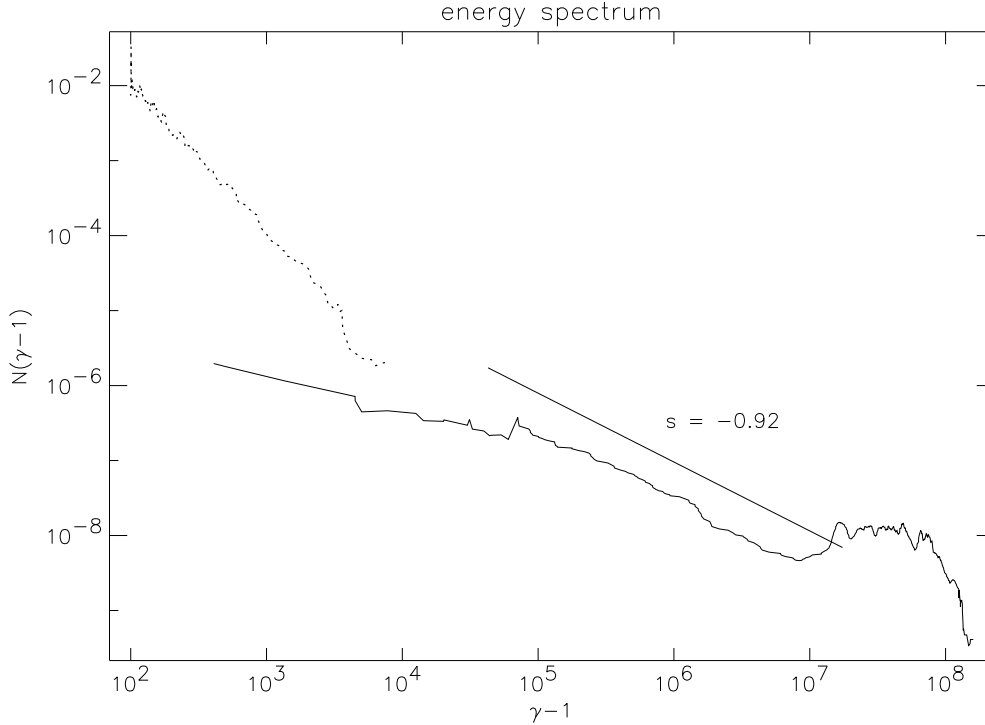


Figure 4.7: The initial (dotted line) and final (solid line) energy spectrum of a test particle run with larger box size of $l = 10^{17}$ cm. The density for this run was chosen to be $\hat{\rho} = 10^{-2} m_p/\text{cm}^3$.

an analytic Kraichnan type ideal MHD turbulence (these results will be published elsewhere).

4.4 Conclusions

We studied the acceleration of relativistic electron populations in three-dimensional reconnective turbulence with applications to the Crab nebula. By means of test particle simulations performed within non-linearly evolved electromagnetic fields modeled by resistive MHD simulations and including radiative losses via synchrotron emission we could show that particles are accelerated and form an energy distribution with powerlaw index s ranging from 1.2 to 1.6. We can give limits for the maximum size of the turbulent regions in the nebulae. If the volume is too large and the particle escape time is too long their spectra get significantly harder, i.e. the spectral index is flatter than 1 (see Fig. 4.7). For the case of the Crab nebula we can rule out turbulent cells larger than 10^{16} cm. This limit is in accordance with experimental results from turbulent fluids, in which the turbulence size is limited by the spatial scale of the turbulence source. Since the Crab nebula is powered by a pulsar wind

which is shocked at about 10^{17} cm the spatial scale of the turbulence should be smaller.

We like to suppose the following scenario for the radio emission of the Crab nebula: The nebula is permanently powered by the plasma wind originating from the pulsar. Consequently strong MHD Turbulence is excited in the nebula. In the turbulent regions the leptons experience in situ acceleration in the reconnective turbulent environment. Our simulations prove that the resulting energy spectra and synchrotron spectra are considerably flat and therefore can explain the observed hard radio spectra (Weiler & Shaver 1978). Whereas we concentrate on the Crab nebula, our findings should also be applicable to flat radio spectra of plerions in general. We note, that the efficiency of the acceleration within the test particle approach depends on the ratio of Alfvén speed to velocity of light which determines the effective electric field strength responsible for particle energization. If the Alfvén speed decreases since the magnetic field decreases the electric field will also be weaker, reducing the acceleration to higher energies. If a supernova remnant consists of region with significantly varying magnetic fields and densities the nonthermal particles may be a superposition of particles experiencing different efficiencies and electromagnetic fields.

We note that Atoyan (1999) considered the origin of radio emitting electrons in the Crab nebula in terms of intensive radiative and adiabatic cooling in the past. Whereas he argued that effective in situ acceleration in the nebula is not necessary to explain the radio spectra, our simulations prove the capability of magnetic reconnection to energize an electron population of a magnetized plasma under the influence of external electromagnetic fields onto which the accelerated leptons have no back reaction.

Chapter 5

Particle acceleration in three-dimensional tearing configurations¹

NODES, C., BIRK, G.T., LESCH, H. & SCHOPPER, R.

Abstract: In three-dimensional electromagnetic configurations that result from unstable resistive tearing modes particles can efficiently be accelerated to relativistic energies. To prove this resistive magnetohydrodynamic simulations are used as input configurations for successive test particle simulations. The simulations show the capability of three-dimensional non-linearly evolved tearing modes to accelerate particles perpendicular to the plane of the reconnecting magnetic field components. The simulations differ considerably from analytical approaches by involving a realistic three-dimensional electric field with a non-homogenous component parallel to the current direction. The resulting particle spectra exhibit strong pitch-angle anisotropies. Typically, about 5–8% of an initially Maxwellian distribution is accelerated to the maximum energy levels given by the macroscopic generalized electric potential structure. Results are shown for both, non-relativistic particle acceleration that is of interest, e.g., in the context of auroral arcs and solar flares, and relativistic particle energization that is relevant, e.g., in the context of active galactic nuclei.

5.1 Introduction

Magnetic reconnection is probably the most important mechanism of rapid conversion of magnetic field energy to plasma heating and particle acceleration (Bentley & Mariska 1996; Priest & Forbes 2000b; Biskamp 2000) in fully and partially ionized plasmas. Cosmic plasma phenomena as different as, e.g., flares in active galactic nuclei (AGN) (Lesch & Birk 1997), extragalactic jets (Blackman 1996; Lesch & Birk

¹Nodes *et al.* 2003

1998), solar flares (Priest & Forbes 2000a) and discrete auroral arcs (Otto & Birk 1993) probably show particle acceleration in reconnection regions.

The problem of particle acceleration is a long standing problem, since the acceleration process depends critically on the local properties of the reconnection region. The efficiency of the particle energization is a function of the effective electric field force that acts on the particle. In two-dimensional reconnection configurations particle acceleration has been extensively studied analytically (e.g., Wagner *et al.* 1981; Litvinenko 1996) and numerically within the framework of resistive (e.g., Bruhwiler & Zweibel 1992; Moses, Finn & Ling 1993; Kliem 1994) and collisionless (e.g., Horiuchi & Sato 1997; Vekstein & Browning 1997; Litvinenko 1997) reconnection. Test particle simulations have proven the efficiency of particle energization in turbulent reconnection (e.g., Ambrosiano *et al.* 1988). These studies have been performed for idealized electric and magnetic field configurations, in particular homogeneous electric fields in the invariant direction, which differ significantly from the three-dimensional configurations characterized by localized field-aligned electric fields.

Test particle simulations of electron injection in high-beta plasmas have shown that the investigation of more complex and therefore more realistic three-dimensional field configurations is crucial for the understanding of particle acceleration in reconnection regions (Birn *et al.* 1998). Three-dimensional test particle simulations of particle acceleration in reconnection regions that result from shear flows have proven the short-comings of idealized analytical two-dimensional treatments of the particle acceleration problem (Schopper, Birk & Lesch 1999).

In the present contribution we consider the resistive tearing mode instability, because it is considered as the generic spontaneous reconnection process (Furth, Killeen & Rosenbluth 1963; see also Priest & Forbes 2000b, Biskamp 2000 and references therein). We present test particle simulations that start from magnetohydrodynamic (MHD) configurations resulting from the non-linear dynamics of tearing modes in three dimensions.

Our studies are relevant for particle acceleration in plasmas that can be described as fluids. Processes that are of importance for particle acceleration in collisionless plasmas as resonant nonlinear wave particle interaction (Hoshino *et al.* 1992; Melrose 1994) are beyond the scope of our present approach.

The test particle simulations are carried out for different ratios of the asymptotic equilibrium sheared magnetic field component to the field component along the initial current direction. For the initial particle distribution a non-relativistic Maxwellian and a relativistic power law distribution are chosen, respectively. In the next section the initial non-linearly evolved MHD configuration is introduced. In 5.3 the results of the test particle simulations are presented for the non-relativistic and the relativistic cases. Eventually, we discuss our findings in 5.4.

5.2 The MHD initial configuration

The MHD balance equations that govern the non-relativistic macroscopic low-frequency dynamics read in a dimensionless form

$$\frac{\partial \rho}{\partial t} + \nabla \cdot (\rho \mathbf{v}) = 0 \quad (5.1)$$

$$\frac{\partial \rho \mathbf{v}}{\partial t} + \nabla \cdot (\rho \mathbf{v} \mathbf{v}) = -\nabla p + \nabla \times \mathbf{B} \times \mathbf{B} \quad (5.2)$$

$$\frac{\partial p}{\partial t} = -\mathbf{v} \cdot \nabla p - \gamma p \nabla \cdot \mathbf{v} + (\gamma - 1) \eta (\nabla \times \mathbf{B})^2 \quad (5.3)$$

$$\frac{\partial \mathbf{B}}{\partial t} = \nabla \times (\mathbf{v} \times \mathbf{B}) - \nabla \times (\eta \nabla \times \mathbf{B}) \quad (5.4)$$

where ρ , \mathbf{v} , p , and \mathbf{B} denote the mass density, bulk velocity, thermal pressure, and the magnetic field. By η the normalized diffusivity, i.e. the inverse magnetic Reynolds number, is denoted. All quantities are made dimensionless by a typical mass density ρ_0 , magnetic field strength B_0 , and length scale L , the Alfvén velocity $v_A = B_0/\sqrt{4\pi\rho}$ and Alfvénic transit time $t_A = L/v_A$. Other normalizing parameters follow in a generic way.

The balance equations are numerically integrated by means of a three-dimensional finite differences code (Otto 1990). The MHD simulations start from an initial configuration given by

$$\mathbf{B}^{eq} = B_s \tanh(y) \mathbf{e}_x + B_n \mathbf{e}_z \quad ; \quad \rho^{eq} = \rho_0 \cosh^{-2}(y) \quad (5.5)$$

which is known as a Harris sheet equilibrium (Harris 1962) with a leading magnetic field component added along the current direction. It is assumed that the ideal gas condition holds $p = nkT$ (where n , T , and k are the particle number density, temperature, and the Boltzmann constant). The resistivity is chosen to be localized around the midplane in the z -direction $\eta = \hat{\eta} \cosh^{-2}((z - 30)/3)$ with an amplitude of $\hat{\eta} = 0.005$. This equilibrium, which can be regarded as an idealized standard current sheet configuration, is perturbed by tearing eigenmodes

$$\begin{aligned} v_x &= \hat{v}_x \rho_0 \sin\left(\frac{\pi x}{x_{\max}}\right) \left(\left(1 - \frac{|y|}{y_{\max}}\right) \left(1 - \frac{|y|}{\eta^{1/4}}\right) - \frac{|y|}{y_{\max}} \right) e^{-\frac{|y|}{\eta^{1/4}}} \\ v_y &= -\hat{v}_y \rho_0 \cos\left(\frac{\pi x}{x_{\max}}\right) \frac{\pi y}{x_{\max}} \left(1 - \frac{|y|}{y_{\max}}\right) e^{-\frac{|y|}{\eta^{1/4}}}. \end{aligned} \quad (5.6)$$

The simulation runs were performed with the resolution of $77 \times 77 \times 63$ grid points in a numerical box given by $x \in [-25, 25]$, $y \in [-10, 10]$, and $z \in [0, 60]$ in normalized units. In the x - and z -direction an equidistant discretization was chosen. The highest resolution of the non-equidistant grid in the y -direction is 0.05. The non-linear dynamics of the resistive tearing mode results in a magnetic field configuration with

the tearing-like X- and O-point structure in the x - y -plane. The magnetic field used as initial configuration for the first particle test simulations (see 5.3) is shown in Fig. 5.1. The respective three-dimensional electric field is shown in Fig. 5.2. Obviously, a complex three-dimensional electromagnetic field configuration appears which, differs significantly from analytical configurations used to study particle acceleration. We emphasize that our simulations are characterized by non-homogenous magnetic and electric field components perpendicular to the reconnection flows, i.e. along the direction of the initial current sheet. They make an important difference to any analytical approach.

5.3 Simulations on particle acceleration

Since in many space and astrophysical circumstances unsaturated external shear flows (stellar winds, stellar explosions, jets from quasars, etc...) agitate magnetic fields and drive the resistive tearing modes our MHD calculations are used as the electromagnetic environment for the studies of electron acceleration by means of test particle simulations. We simply want to know how electric particles behave in the complex three-dimensional electro-magnetic field configuration and neglect any back reaction of the particles onto the field structure.

Thus, the electric field is derived only from the MHD quantities \mathbf{B} , \mathbf{v} and η by means of Ohm's law

$$\mathbf{E} = -\frac{1}{c}\mathbf{v} \times \mathbf{B} + \eta \nabla \times \mathbf{B}. \quad (5.7)$$

Since the data for the electric and magnetic field is only available on a discrete three-dimensional grid the test particle code uses linear interpolation to determine the field values for any location. We note that the term "test particle" simply means that the electromagnetic fields produced by the particles are not changing the global fields, though the effect of synchrotron radiation on the motion of the particles is taken into account, i.e. the relativistic equations of motion have the form

$$\frac{d\mathbf{p}}{dt} = q \left(\mathbf{E} + \frac{1}{\gamma mc} \mathbf{p} \times \mathbf{B} \right) + \mathbf{F}_{Rad}, \quad \frac{d\mathbf{r}}{dt} = \frac{\mathbf{p}}{\gamma m}, \quad (5.8)$$

where m and q denote the mass and charge of the particles, which are electrons in our case and

$$\gamma = \sqrt{1 + \left(\frac{p}{mc} \right)^2} \quad (5.9)$$

is the Lorentz factor.

The calculations are relativistic, including the energy losses via synchrotron radiation and inverse Compton scattering by the term \mathbf{F}_{Rad} , which we discuss in detail in 5.3.2. For the non-relativistic case of particle acceleration, as considered in the following sub-section, the radiative losses are negligible. The equations are numerically integrated by a Runge-Kutta algorithm of fourth order with an adaptive stepsize control. As a result we get the momentum and location at certain times of each particle in the given ensemble.

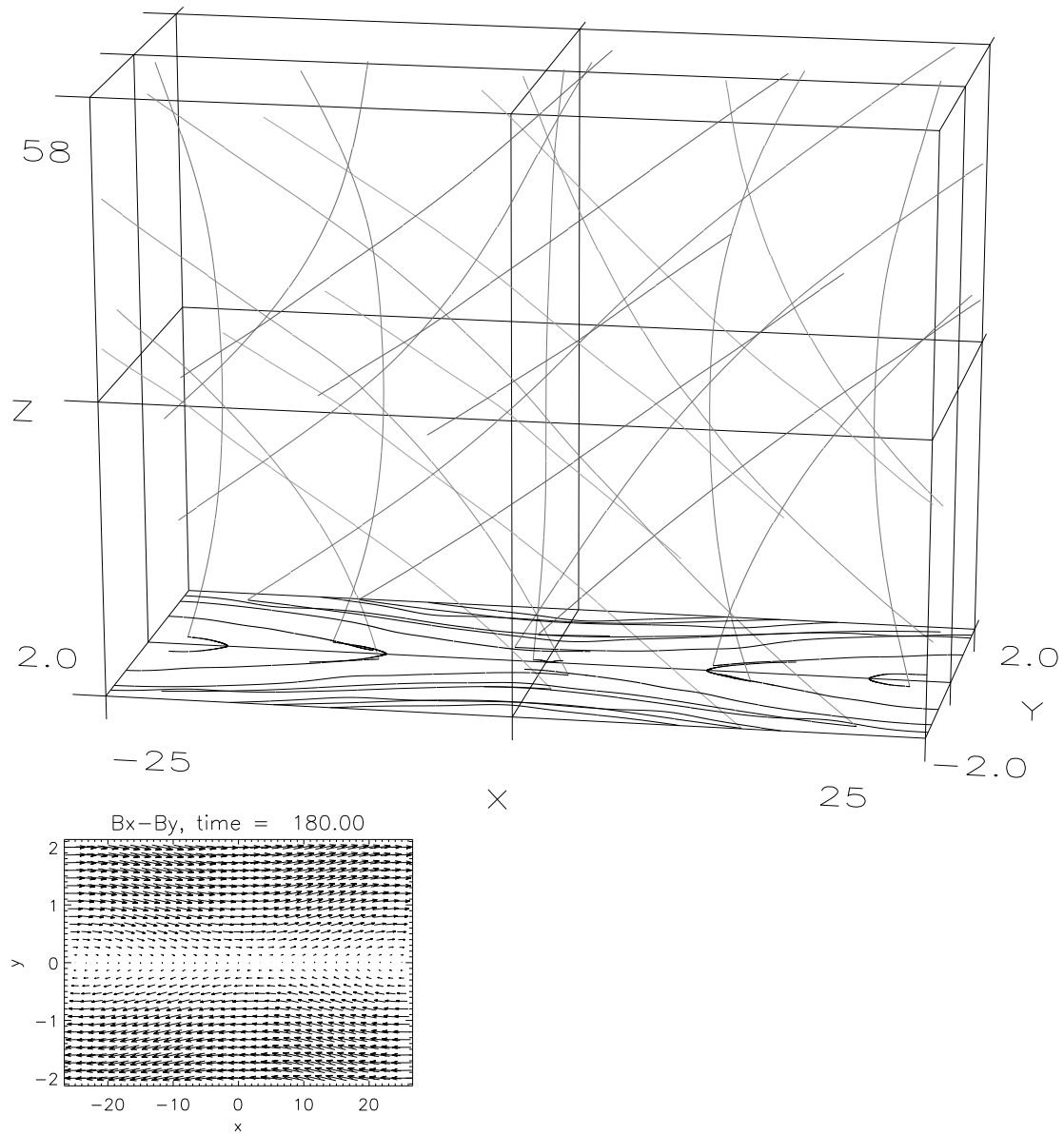


Figure 5.1: The magnetic field configuration that results from the MHD simulation after 180 Alfvén times. The upper plot shows magnetic field lines, the lower one shows an arrow plot of the x - and y -components of the magnetic field at $z = 30$.

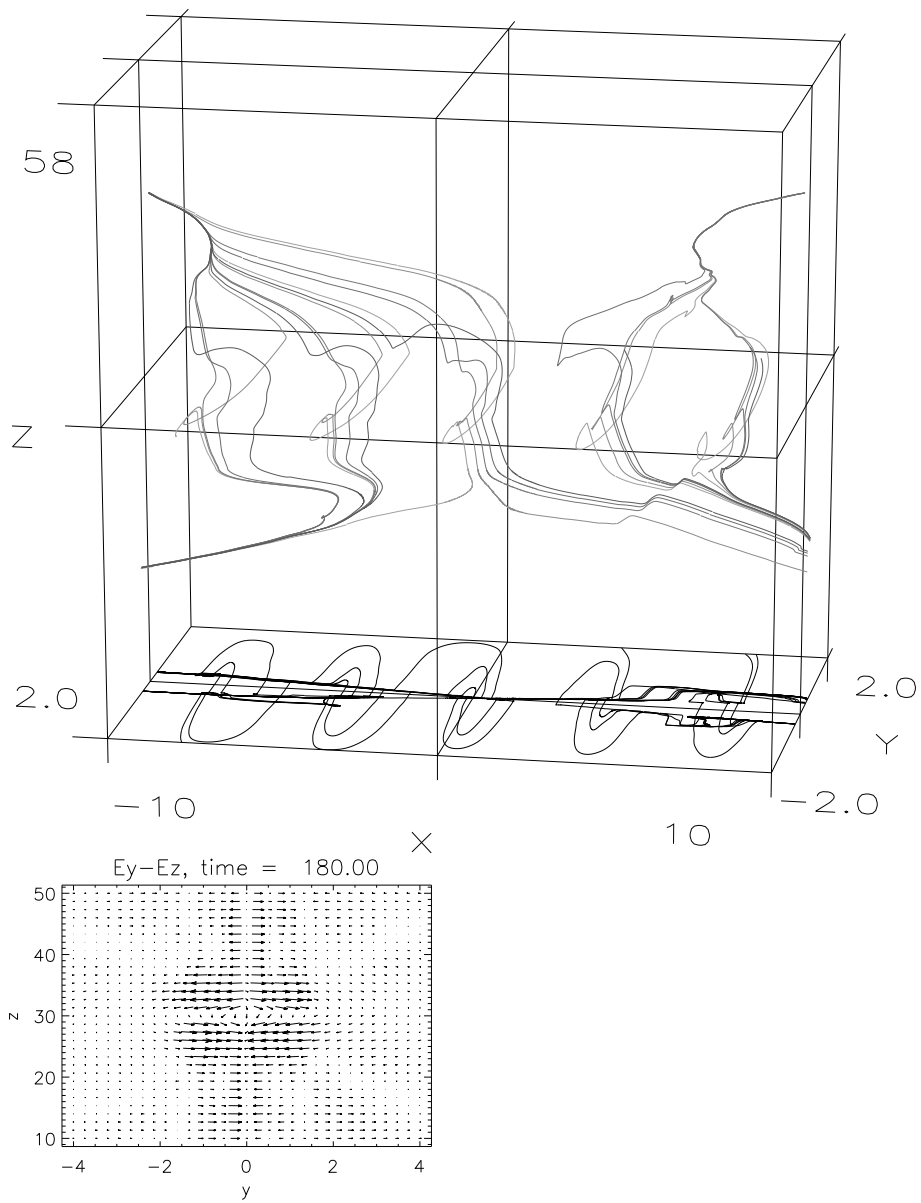


Figure 5.2: The electric field configuration after $t = 180\tau_A$. The upper plot shows electric field lines, the lower one shows an arrow plot of the y - and z -components of the electric field at $x = 3$.

5.3.1 Non-relativistic particle acceleration

The choice of parameters for our studies of non-relativistic particle acceleration is motivated by the phenomena of discrete auroral arcs for example. Reconnection may play an important role in the energization of auroral particles in Birkeland current sheets (Otto & Birk 1993; Birk & Otto 1997). Our results are, however, to be understood as rather general ones for particle acceleration in three-dimensional tearing configurations. Therefore, we present results from test particle simulation runs for three different ratios of B_n to B_s : $B_n/B_s = 1 : 1, 10 : 1$, and $100 : 1$. The strength of the main magnetic field component is chosen as $B_n^{1:1} \approx 10^{-3}$ Gauss. The electric field components are $E_x \approx 10^{-5} B_n$ and $E_y \approx E_z \approx 10^{-4} B_n$, respectively. It is a characteristic feature of 3D reconnection that the magnitude of the electric field component directed along the initial current sheet is of the order of the dominant convective electric field component. The spatial parameters for the first three runs were adjusted to those of auroral phenomena, i.e. the size of the box is $2000 \times 800 \times 2400$ km. The initial position of the particles is uniformly distributed in the $(x,y,0)$ -plane at the lower z end of the box. For the particle distribution we choose a Maxwellian distribution with a corresponding temperature of $k_B T \approx 1$ eV and a shift of the momentum in the z -direction of a few percent of the thermal energy, thus the distribution is in fact slightly anisotropic. We consider the state when all electrons have left the computational box as the final state.

The trajectories of all electrons for each run are shown in Fig. 5.3 - 5.5 as a projection on the y - z -plane. The gyration motions of the electrons occur on a much smaller scale so that this motion cannot be identified, but it is fully resolved in the simulation. The reconnection zone is placed between $z \approx 1000$ and $z \approx 1500$ where the $\mathbf{E} \times \mathbf{B}$ -drift forces the electrons to move towards the center of the region. Those electrons which start at coordinates with a y -value close to zero are most efficiently accelerated. They leave the box at high z -values while the others leave the box at the x and y boundaries following the magnetic field lines. The acceleration takes place on very short timescales of a few 10^{-1} seconds.

Fig. 5.6 - 5.8 present the initial and final energy spectra of the electrons. Obviously, most of the electrons keep their initial Maxwellian distribution. The injected test-particles are not noticeably heated. Some fraction of the electrons are accelerated and show a power law with an average index of 1.1 to 1.5. The main recognizable result is the pile-up of electrons at the high energy tail of the distribution, which shows up in all simulations. The heights of the peaks, i.e. the number of accelerated electrons, increase with decreasing B_n/B_s (Fig. 5.6 to 5.8), while the maximum energization is approximately constant.

In Fig. 5.9 - 5.12 the relative momentum distribution of the test particles of the first run is displayed. The $p_x - p_z$ cut of the phase space shows that the accelerated particles have comparable momentum gains in x - and z -direction (figures 5.9-5.10), whereas there is almost no momentum gain in the y -direction (5.11-5.12). For the cases with smaller ratios of B_n/B_s the acceleration is almost exclusively along the current sheet.

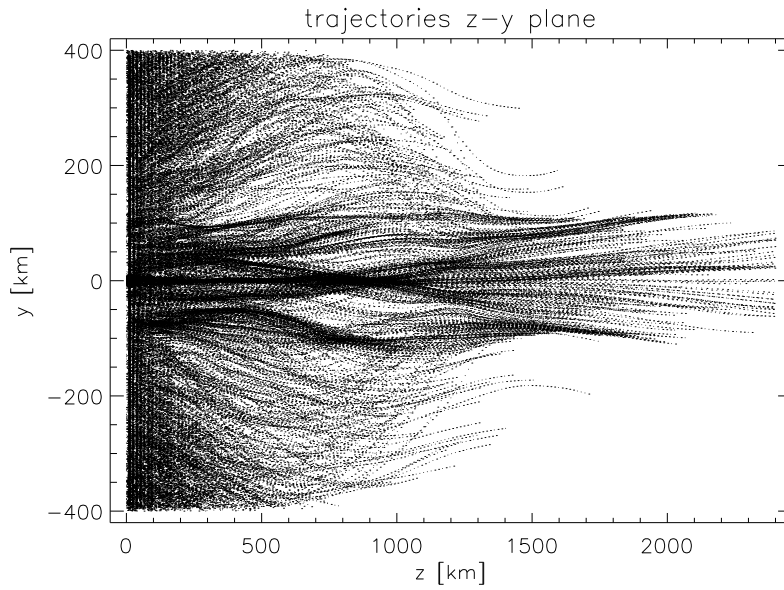


Figure 5.3: The trajectories of all electrons of the first run ($B_n/B_s = 1 : 1$) as a projection on the $y - z$ plane.

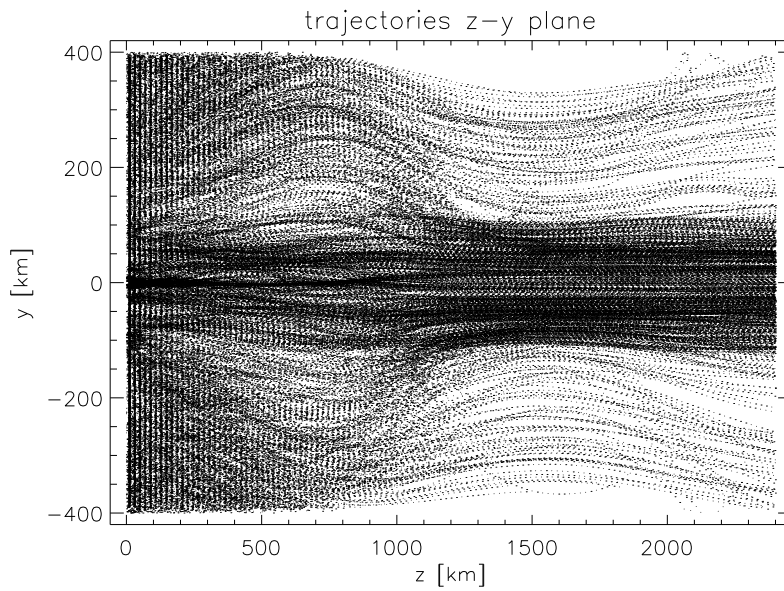


Figure 5.4: The trajectories of all electrons of the second run ($B_n/B_s = 10 : 1$) as a projection on the $y - z$ plane.

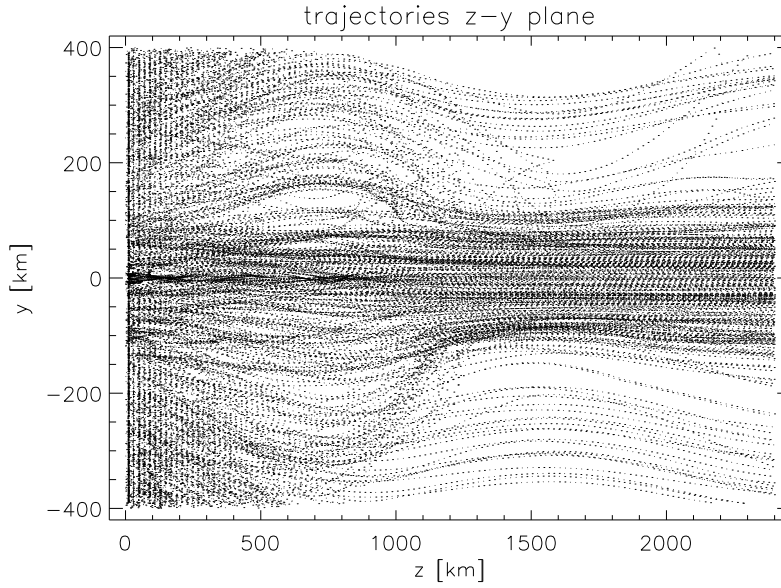


Figure 5.5: The trajectories of all electrons of the third run ($B_n/B_s = 100 : 1$) as a projection on the $y - z$ plane.

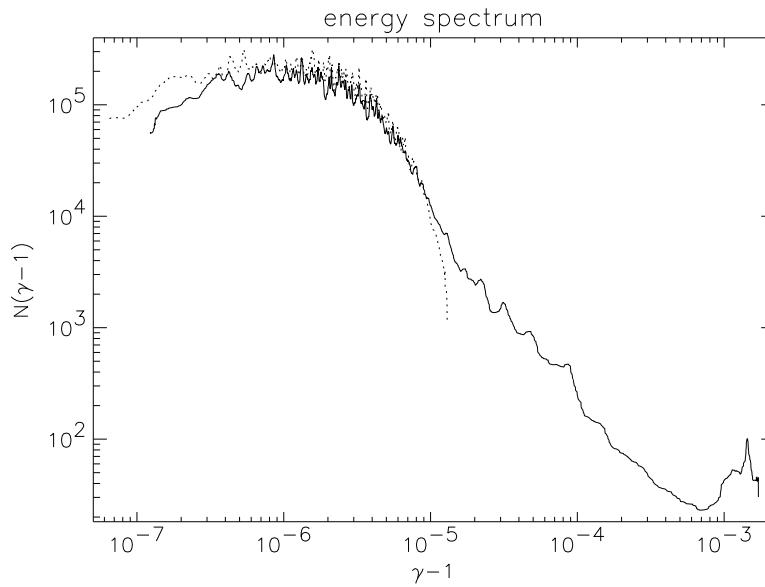


Figure 5.6: The spectrum of kinetic energy in the first run. The relative number frequency is plotted against the kinetic energy in units of mc^2 . The dotted line represents the initial distribution while the normal line is the final distribution.

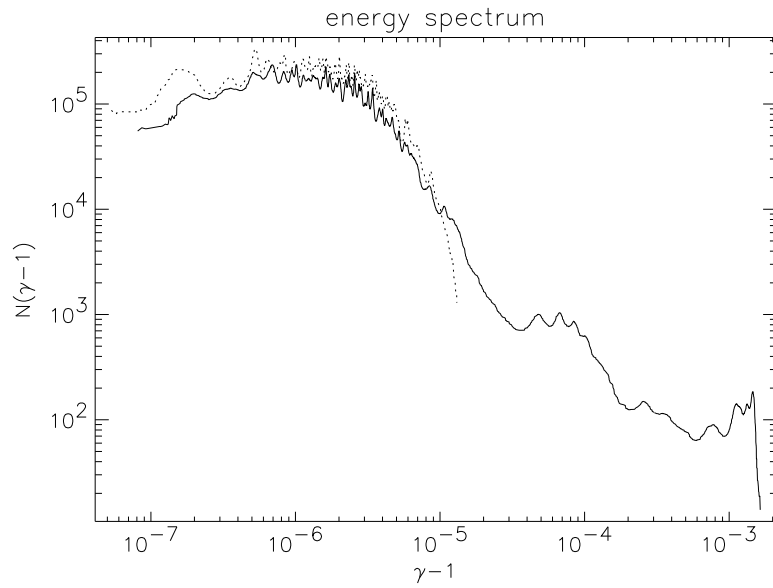


Figure 5.7: The spectrum of kinetic energy in the second run.

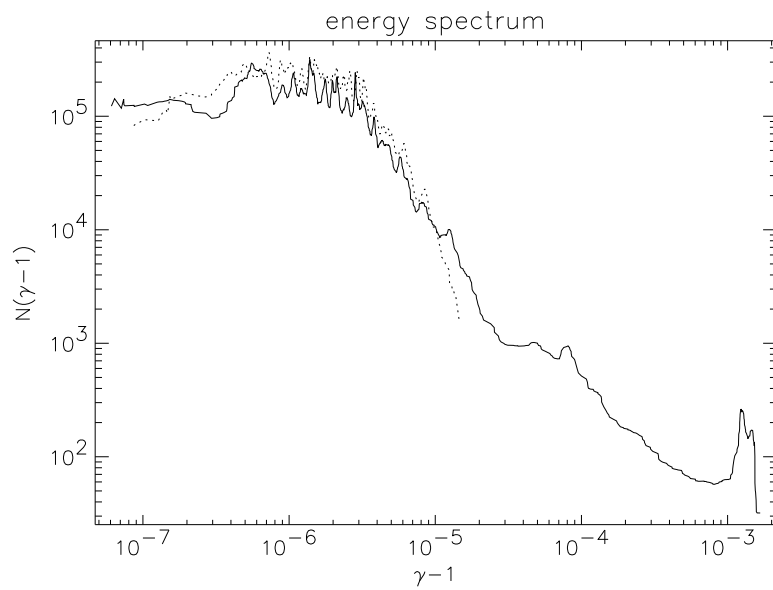


Figure 5.8: The spectrum of kinetic energy in the third run.

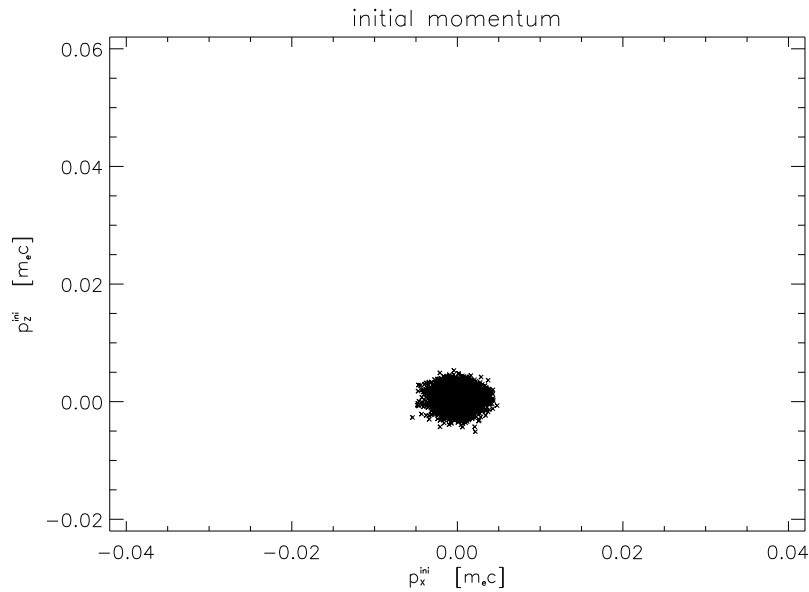


Figure 5.9: The initial momentum plotted in the $p_x - p_z$ plane of phase space of the first run ($B_n/B_s = 1 : 1$).

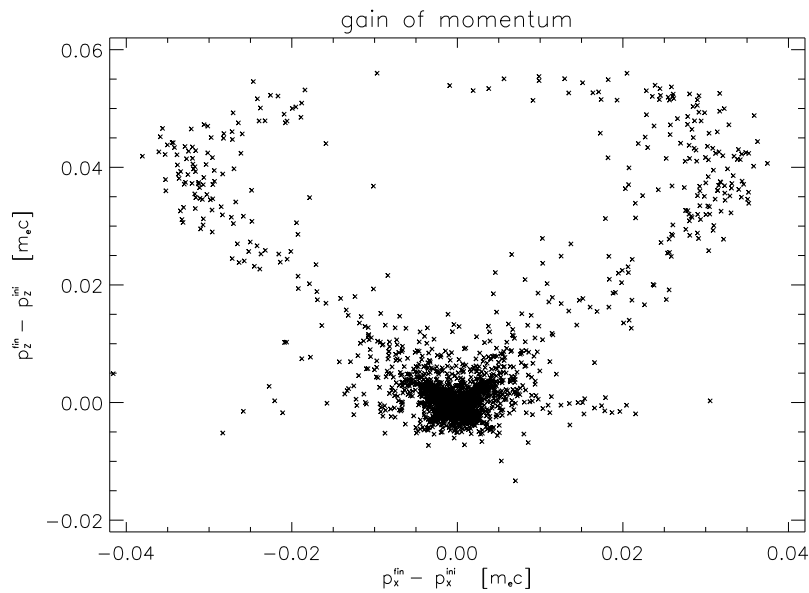


Figure 5.10: The gain of momentum in z direction compared to that in x direction. For most of the accelerated particles p_z is only slightly higher than p_x .

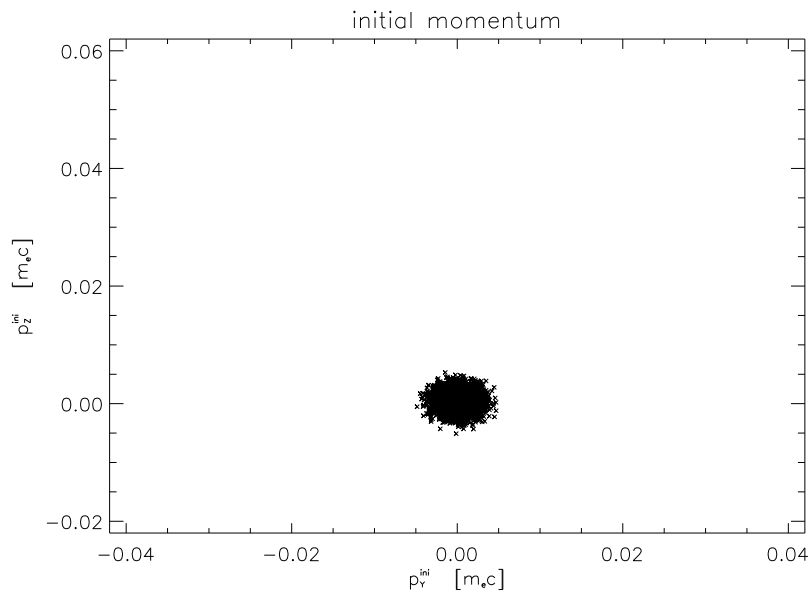


Figure 5.11: The initial momentum plotted in the $p_y - p_z$ plane of phase space of the first run ($B_n/B_s = 1 : 1$).

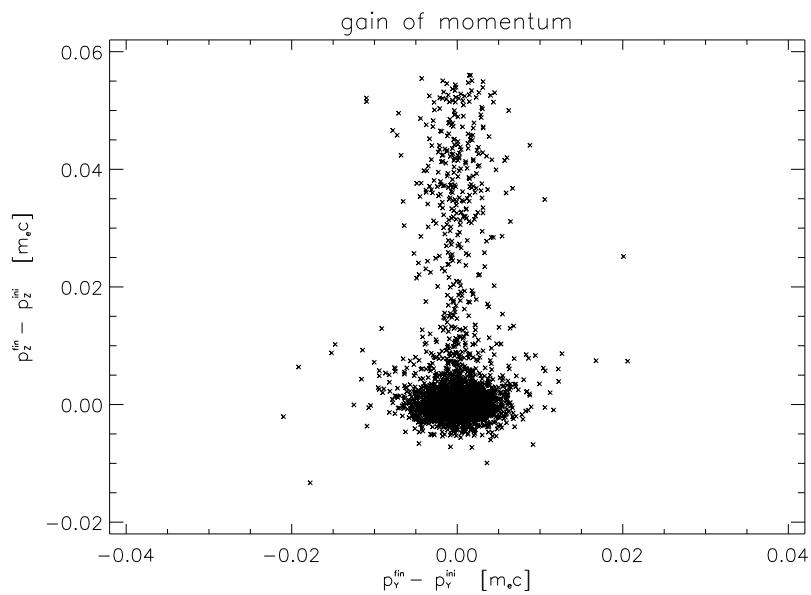


Figure 5.12: The gain of momentum in z direction compared to that in y direction. There is no noticeable gain in y direction.

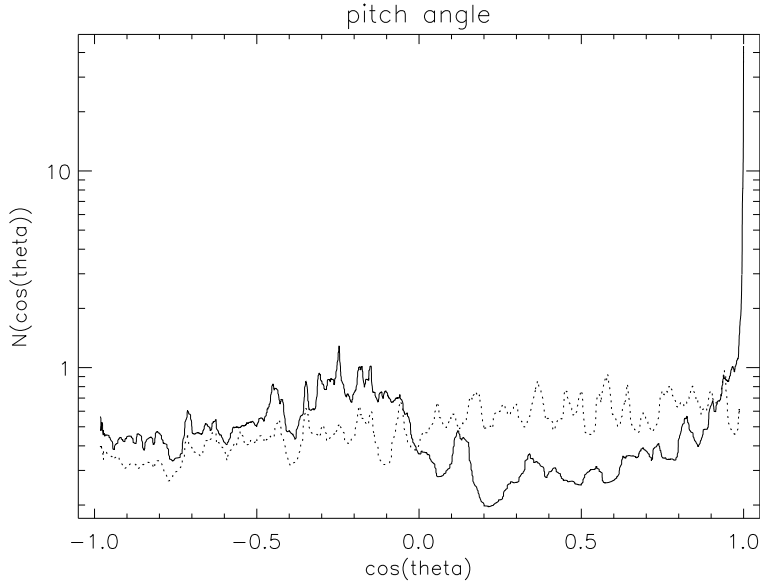


Figure 5.13: The pitch angle distribution at the beginning (dotted line) and at the end (normal line) of the first simulation ($B_n/B_s = 1 : 1$). The relative number frequency is plotted against $\cos(\theta)$.

The pitch angle distribution (Fig. 5.13) shows a clear anisotropy in the final state, i.e. there is a strong peak of the distribution function at $\cos(\theta) = 1$ along with a depression in between $0 < \cos(\theta) < 0.9$. This might be explained by the fact that the electrons get accelerated by the component of the electric field parallel to the magnetic field, E_{\parallel} . Thus, they only gain momentum parallel to the magnetic field while the perpendicular component p_{\perp} remains constant (just like in the homogeneous case). Consequently, the momentum vector is predominantly directed parallel to the magnetic field. We would like to emphasize that such a pitch angle anisotropy is characteristic for the so-called inverted V events detected by satellites below the main auroral acceleration regions (Lin & Hoffmann 1979). Thus, our results corroborate the current striation model for auroral acceleration in which the tearing instability plays a central role (Otto & Birk 1993).

Fig. 5.14 shows the initial and final pitch angle distribution for the most energetic particles of the first run with $B_n/B_s = 1 : 1$. This plot clearly indicates that the pitch angles of the most energized particles depend on their initial pitch angle as it is expected for a non stochastic acceleration process.

We emphasize that different from two-dimensional studies (Wagner, Kan & Akasofu 1979) a significant fraction of the particles is not trapped in the O-point regions and thus efficiently accelerated.

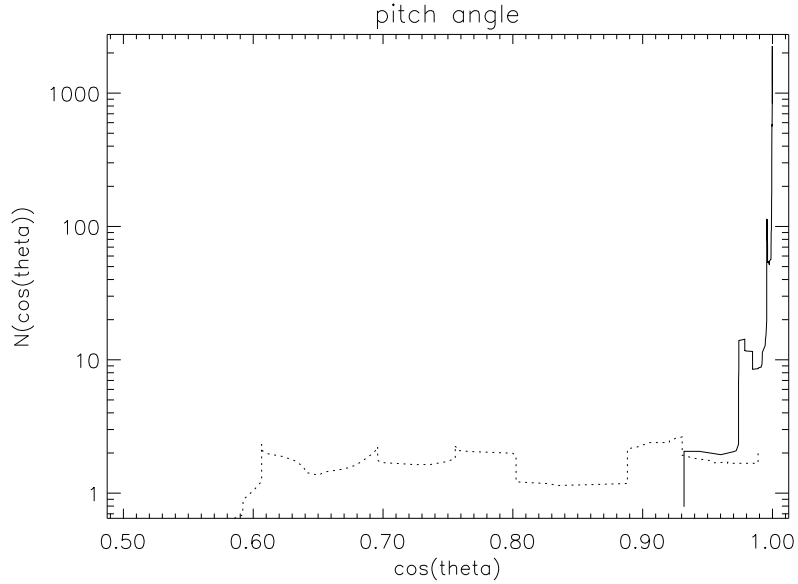


Figure 5.14: The pitch angle distribution of the electrons with the highest energy gain. These electrons already start with very small pitch angles.

5.3.2 Relativistic particle acceleration

In this section we discuss simulations in a parameter range which is typical for the central regions of active galactic nuclei. Such objects like quasars are accreting massive black holes surrounded by magnetized accretion disks from which relativistic plasma jets emanate. They exhibit very rapid flares in almost all bands of the electromagnetic spectrum, especially in the TeV-range (Gaidos *et al.* 1996). The spectra are power laws, i.e. the radiation is of nonthermal origin, for example synchrotron radiation and/or inverse Compton scattering. The time scales for some these flares are down to 30 min. In other words, within that short time scale a significant number of particles has to be accelerated very efficiently to provide the observed radiation fluxes. Since we know that these objects contain differentially rotating magnetized gas disks surrounded by magnetized coronae we think that magnetic reconnection may provide the required fast particle acceleration (Lesch 2000). As mentioned above the tearing mode is a generic configuration for reconnection, thus we consider acceleration under circumstances typical for the central light year of an active galactic nucleus. We note that our simulations do not consider an individual object or flare event but concentrate on the general mechanism for energization of relativistic particles in magnetized plasmas. Especially we do not consider the plasma at some specific distance from the central black hole, rather we simulate the part of a plasma volume with a magnetic field typical for the central 10^{18} cm above the magnetized accretion disk and close to the magnetized emanating jet. Accordingly, the size of the computational box was chosen as $(100 \times 40 \times 120) \times 10^{13}$ cm. The main com-

ponent of the magnetic field as well as the asymptotic shear component was scaled to $B_n \approx 0.1$ Gauss, i.e. the ratio for all relativistic runs was $B_n/B_s = 1 : 1$. The associated electric field reads $E_x \approx 10^{-3}$, $E_y \approx 10^{-2}$, and $E_z \approx 10^{-3}$ in units of B_n .

We show results of three different runs. One run starts with a relativistic Maxwellian distribution (with $kT/mc^2 = 50$) and in the other runs we use initial power law energy distributions for the injected electrons with Lorentz factors ranging from 10^4 up to $2 \cdot 10^6$ and 10^2 up to $2 \cdot 10^4$, respectively. A power law distribution mimics a pre-accelerated electron population in an active galactic nucleus.

In the considered high energy ranges (GeV to TeV) the losses due to synchrotron radiation and inverse Compton scattering certainly play a role, thus the term

$$\begin{aligned} \mathbf{F}_{Rad} \approx & \frac{2}{3} \frac{q^4}{m^2 c^4} \left\{ \mathbf{E} \times \mathbf{B} + \frac{1}{c} \mathbf{B} \times (\mathbf{B} \times \mathbf{v}) + \frac{1}{c} \mathbf{E} (\mathbf{E} \cdot \mathbf{v}) \right\} \\ & - \frac{2}{3} \frac{q^4}{m^2 c^5} \gamma^2 \mathbf{v} \left\{ \frac{16\pi}{3} U_{Ph} + \left(\mathbf{E} + \frac{1}{c} \mathbf{v} \times \mathbf{B} \right)^2 - \frac{1}{c^2} (\mathbf{E} \cdot \mathbf{v})^2 \right\} \quad (5.10) \end{aligned}$$

now becomes important for the motion of the electrons (see Eq.(8)). Expression (5.10) is an approximated form of the damping force due to radiation given by Landau and Lifshitz 1951 which we used in our code. U_{Ph} denotes the photon energy density, which has to be considered for inverse Compton scattering. For AGN coroneae a typical value is $U_{Ph} \approx 10^{-4}$ erg/cm³.

The resulting synchrotron spectra can be calculated as the sum of total power emitted by each individual electron. The latter is given by Rybicki & Lightman 1979

$$P \left(\frac{\omega}{\omega_c} \right) = \frac{\sqrt{3}}{2\pi} \frac{e^3 B}{mc^2} \sin \theta \frac{\omega}{\omega_c} \int_{\frac{\omega}{\omega_c}}^{\infty} K_{\frac{5}{3}}(\xi) d\xi, \quad (5.11)$$

where ω_c is the critical frequency, θ is the pitch angle and $K_{\frac{5}{3}}$ is the modified Bessel function.

Let us first discuss the case with an initial power law with an energy range from $\gamma = 10^4 - 2 \cdot 10^6$. The initial and final energy spectra are presented in Fig. 5.15. Quite a large fraction of the electrons get decelerated below $\gamma \sim 10^4$ whereas some reach energies up to $\gamma \sim 10^7$. The deceleration of particles is caused by the electromagnetic forces and associated radiation losses they experience along their trajectories. Different from the accelerated particles they do not enter the inner reconnection region where the dominant electric field component is directed parallel to their guiding center motion. Their enhanced perpendicular momentum gives rise to efficient radiative losses.

The distribution also shows this beam-like built-up of electrons at higher energies which was observed in the low energy simulations. Unlike the non-relativistic simulations, here the electrons get somewhat decelerated after leaving the reconnection region due to the radiation losses, but still have much higher energies in the end than before.

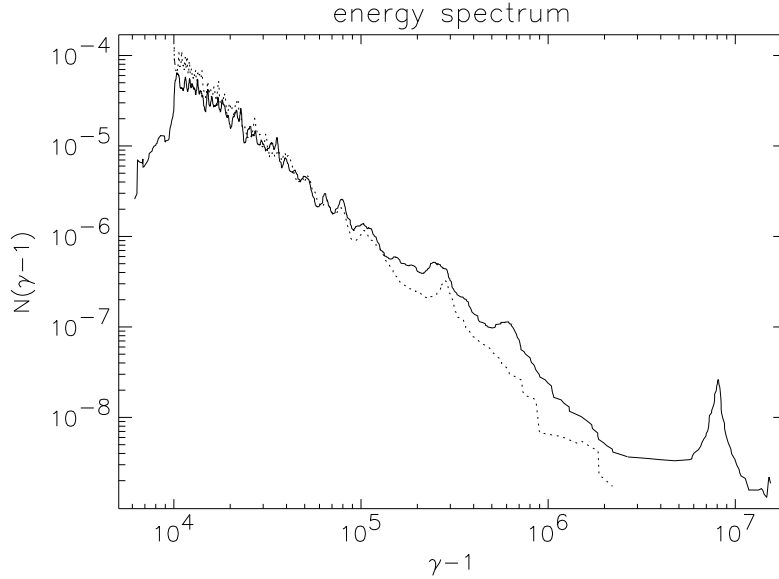


Figure 5.15: The energy spectrum of the first relativistic run. This simulation started with a power law (dotted line) of $N(\gamma - 1)d\gamma = (\gamma - 1)^{-2}d\gamma$. The final spectrum (normal line) shows a local maximum at $(\gamma - 1 \sim 8 \times 10^6)$.

The deceleration of electrons is also visible in the radiation spectrum of the synchrotron emission since the initial spectrum, or radiation power distribution, reaches up to higher frequencies than the final spectrum (Fig. 5.16). On the other hand, the accelerated particles ($\gamma > 10^6$) have a very small pitch angle and therefore do not significantly contribute to the synchrotron emission within our simulation volume. Interesting enough such an anisotropic particle distribution is able to transport energy to regions far away from the acceleration site, since the particles do not lose energy by synchrotron radiation. Such a behavior has been demanded by Ghisellini 1999 for the X-ray and gamma-ray bursting blazars. There must be some energy transport mechanism which is dissipationless up to large distances from the acceleration site, and the appearance of an anisotropic ultrahigh energy component would present such a mechanism (Crusius-Wätzel & Lesch 1998).

The selection which electrons are to be accelerated or decelerated is certainly due to a geometric effect, i.e. only those electrons which have an appropriate initial position experience a strong acceleration. This is visible in Fig. 5.17 - 5.21 in which the trajectories of these two classes of particles are presented. Obviously, only those electrons are most efficiently accelerated which are injected very close to the quasi-separatrix layers. The separatrix-like projection onto the x - y -plane does not necessarily indicate regions of different magnetic topology in the considered three-dimensional configuration. The trajectories of accelerated and decelerated particles are somehow complementary to each other. An interesting feature is the sickle-shaped form of the trajectories in the z - y -projection. It seems as if the recon-

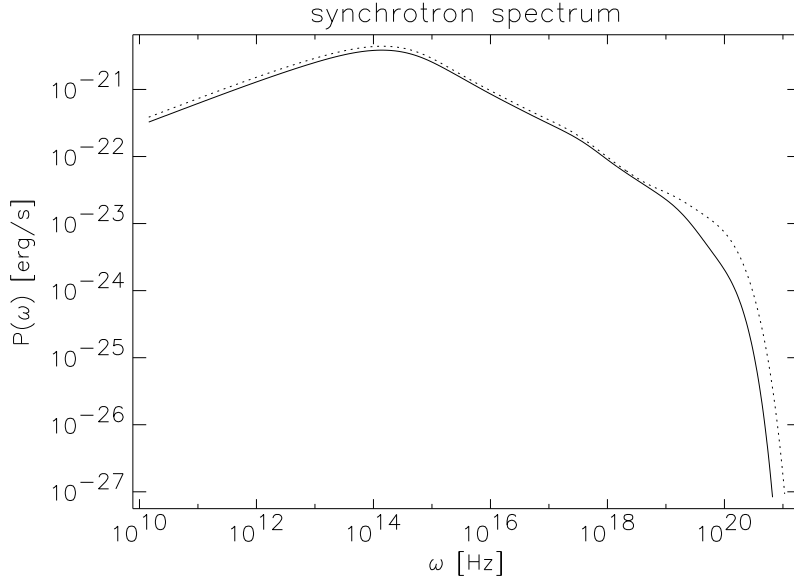


Figure 5.16: The synchrotron spectrum of the first relativistic run.

nection zone acts like a defocusing lens to the accelerated electrons. The decelerated electrons do not move along reconnecting magnetic field lines that cross the initial neutral layer.

In the second run, initialized with an energy range from $\gamma = 10^2 - 2 \cdot 10^4$, the energy and synchrotron spectra are shown in Fig. 5.22 and 5.23. The pile-up at $\gamma \sim 8 \cdot 10^6$ is less pronounced, but still present. The radiation spectrum clearly exhibits a broken power law. The low energy part of the power law is mainly due to the initially injected particles, whereas the high energy part is caused by the accelerated particle population. The particle trajectories are qualitatively similar to the previously discussed run. The same statement holds for the case of the initial relativistic Maxwellian particle distribution. For this case also efficient acceleration occurs (Fig. 5.24, 5.25) but there is no pile-up at high energies. The radiation exhibits a rather flat spectrum at higher energies. This is of particular interest in the context of observations indicating flat nonthermal spectra of blazars (Tosti 1998; Edwards *et al.* 2000) like Mrk 421 and Mrk 501.

5.4 Discussion

Particle acceleration in magnetized collisionless plasmas is a central issue of high energy astrophysics and space physics. A large number of observation in all bands of the electromagnetic spectrum demand for a fast and efficient production of accelerated particles within magnetized plasmas which are agitated by unsaturated external forces like differential rotation, jets, stellar winds and explosive events.

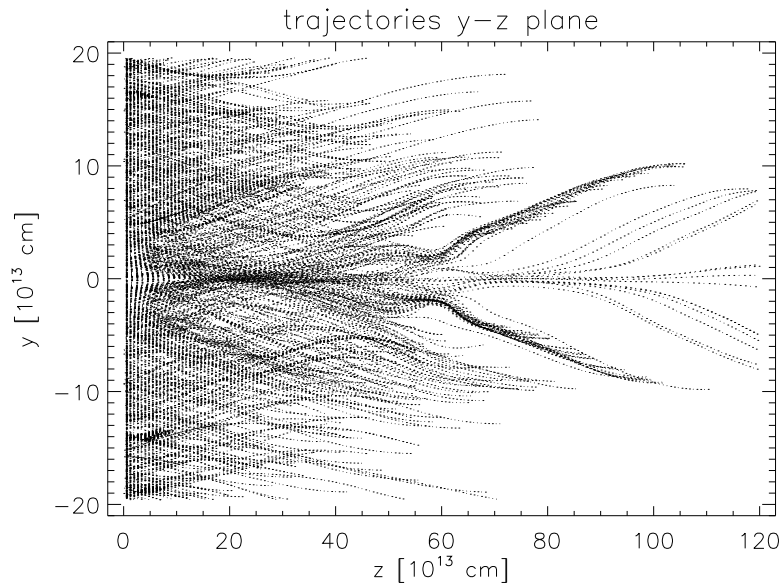


Figure 5.17: The trajectories of the relativistic run as a projection on the $y - z$ plane.

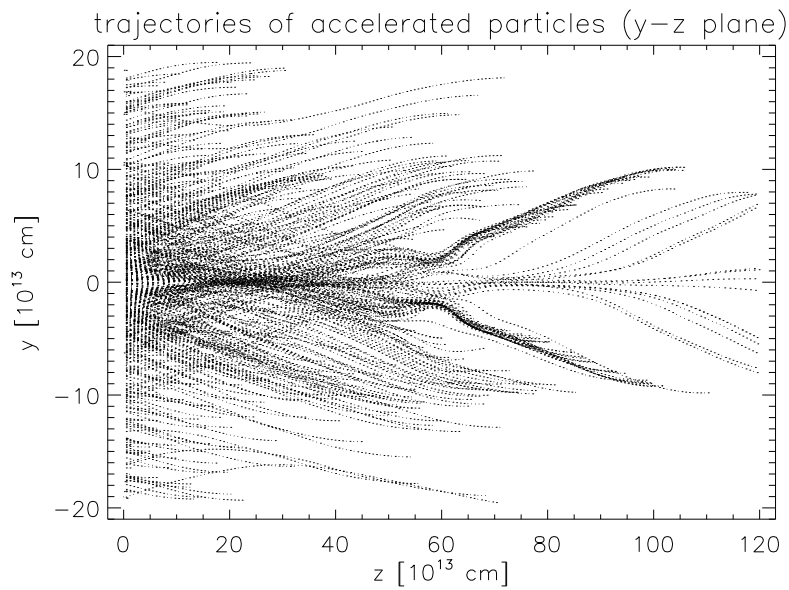


Figure 5.18: The trajectories of the accelerated electrons as projection on the $y - z$ plane.

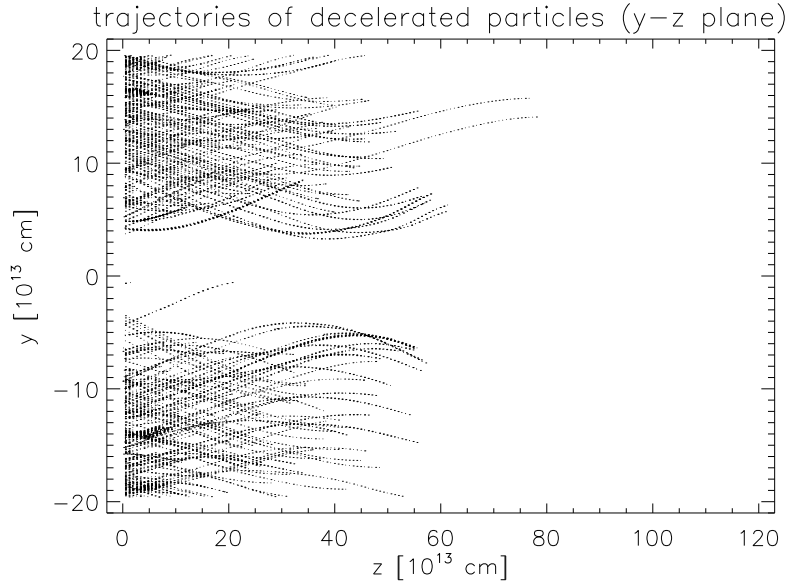


Figure 5.19: The trajectories of the decelerated electrons as projection on the $y-z$ plane.

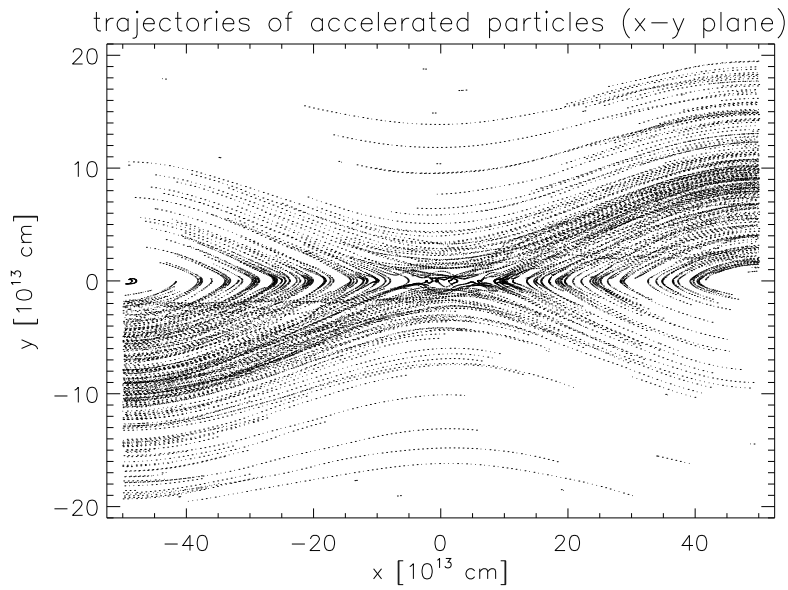


Figure 5.20: The trajectories of the accelerated electrons as projection on the $x-y$ plane.

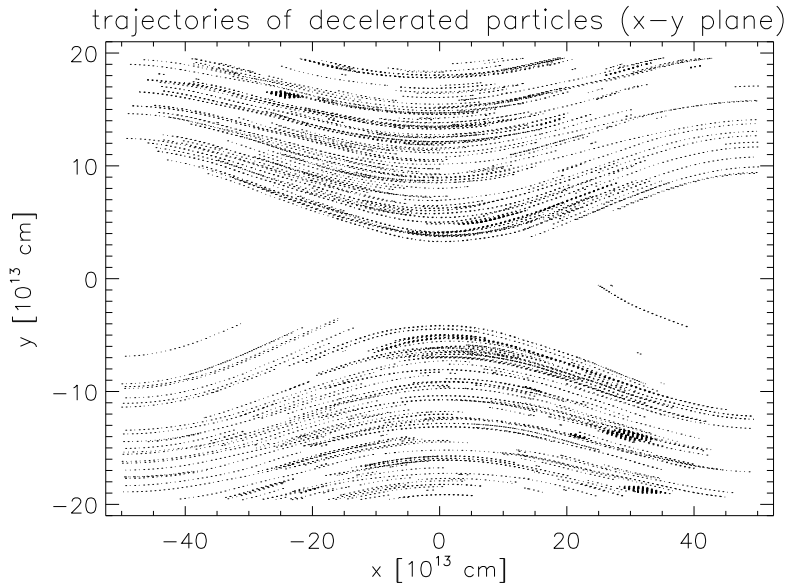


Figure 5.21: The trajectories of the decelerated electrons as projection on the $x - y$ plane.

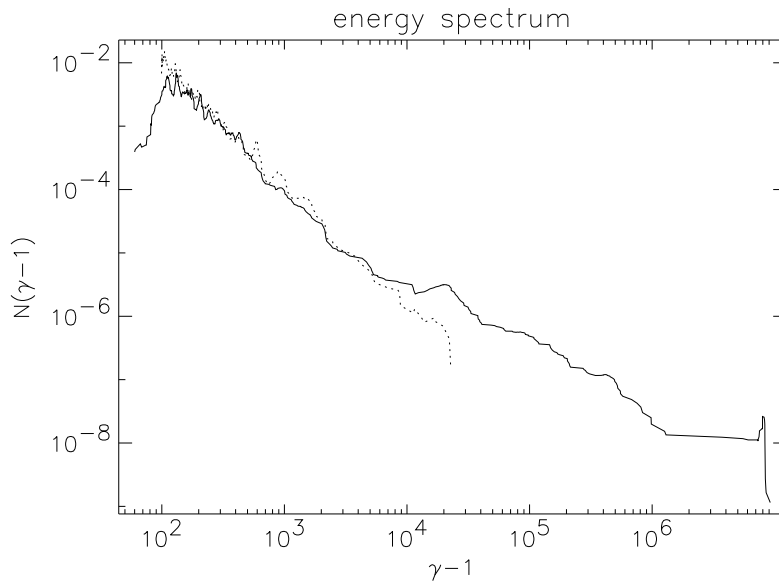


Figure 5.22: The energy spectrum of the second relativistic run. This simulation started with a power law (dotted line) of $N(\gamma - 1)d\gamma = (\gamma - 1)^{-2}d\gamma$. The final spectrum (normal line) shows a pile-up at $(\gamma - 1 \sim 8 \times 10^6)$.

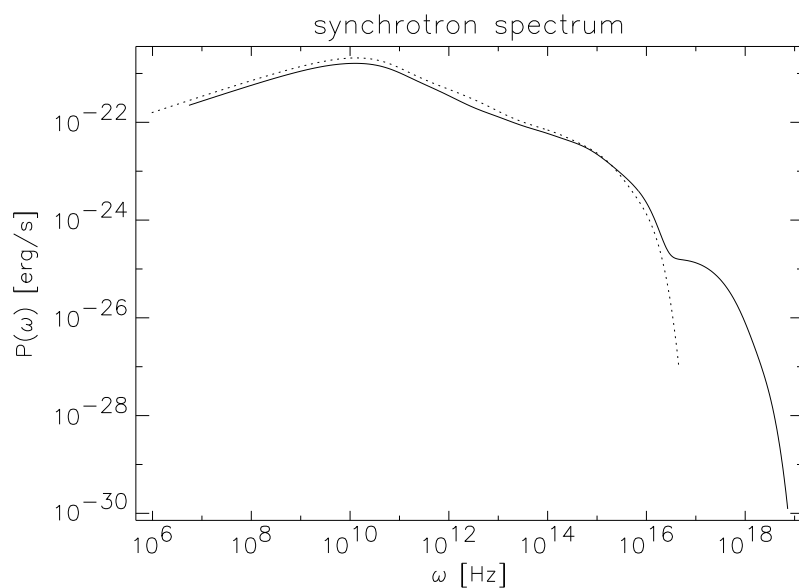


Figure 5.23: The synchrotron spectrum of the second relativistic run.

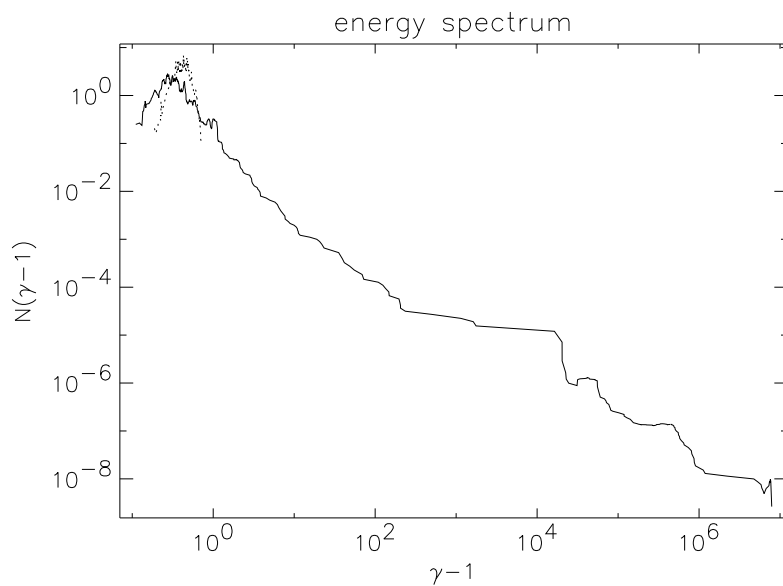


Figure 5.24: The energy spectrum of the third relativistic run that started with a power law (dotted line) of $N(\gamma - 1)d\gamma = (\gamma - 1)^{-2}d\gamma$.

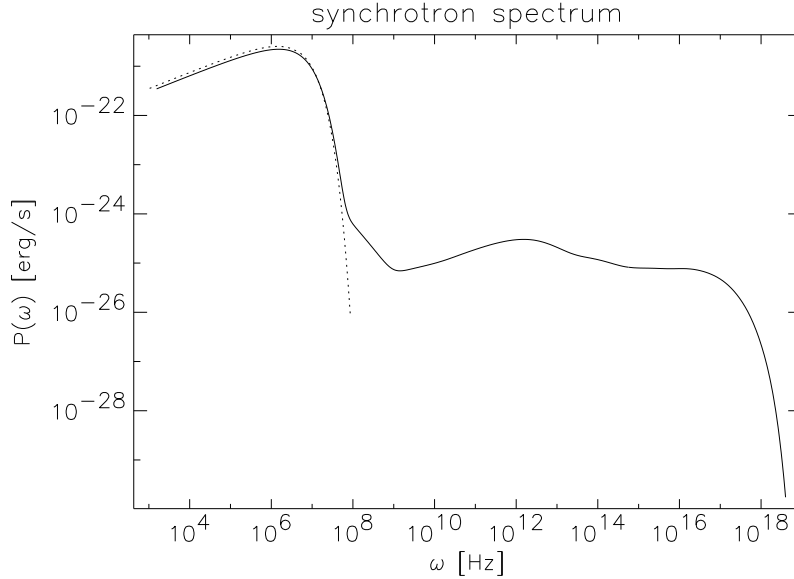


Figure 5.25: The synchrotron spectrum of the third relativistic run.

Such forces twist, shear and stretch field lines into configurations in which magnetic reconnection plays a dominant role either as relaxation mechanisms and/or as acceleration process. The tearing instability is known to be a generic configuration in such reconnection sites.

Thus, we studied the acceleration of non-relativistic and relativistic electron populations in three-dimensional tearing configurations. By means of test particle simulations performed within non-linearly evolved electromagnetic fields modeled by MHD simulations we could show that particles are effectively accelerated. Our simulations include nonthermal radiative losses like synchrotron radiation. Starting from a shifted Maxwellian distribution we carried out test particle simulations for three different ratios of the magnitudes of the initial magnetic field components parallel and perpendicular to the current sheet. For example, we have chosen physical parameters that are relevant for auroral acceleration zones. Our findings are, however, of general interest for particle acceleration in reconnecting current sheets. The degree of the pitch angle anisotropy of the accelerated particles depends on the strength of the guiding magnetic field component along the current sheet. A significant fraction of the initially injected electrons gains momentum. The level of energization is limited by the overall generalized electric potential $U = \int ds E_{\parallel}$.

The relativistic studies dealt with the fate of electrons that enter the reconnection region with a power law distribution. Such a situation is characteristic for flares in active galactic nuclei. Some fraction of the pre-accelerated particles is fast and efficiently energized in the three-dimensional tearing configuration. As in the runs that start from a Maxwellian distribution a high-energy bump forms in the final

distribution.

Our simulations prove the capability of magnetic reconnection to energize an electron population of a magnetized plasma under the influence of external electromagnetic fields onto which the accelerated leptons have no back reaction. For example, close to a black hole the differential rotation of the surrounding accretion disk which shears magnetic field lines is only determined by the mass of a central object but not influenced by the dissipation of magnetic energy in small current sheets. In other words, the external forces which stretch, fold and twist the magnetic field lines act on a much larger spatial scale than the size of the forming current sheets. This behavior is similar to what is known from turbulent plasmas, in which the energy input on large spatial scales is finally dissipated on considerably smaller length scales. Thus, the energy sources and energy sinks are completely disconnected from each other. Furthermore, the enormous strength of such global forces like differential rotation substantiates our test particle approach, which implicitly assumes no back reaction of the particles onto the electrodynamic structure of the plasma.

Our present studies do not include turbulent electromagnetic fields. Numerical studies of particle acceleration in MHD turbulent reconnection regions seem to be a promising task for the future.

Chapter 6

Discussion

This thesis addressed the acceleration of charged particles due to magnetic reconnection in the context of Pulsar Wind Nebulae. A Pulsar Wind Nebula can be understood as an expanding bubble of hot plasma which is powered by a central pulsar. The pulsar releases enormous amounts of magnetic energy in form of a strong plasma wind which is converted into kinetic energy of relativistic particles, and eventually into the synchrotron radiation that we observe. The radio emission from PWNe shows a remarkably flat power law spectrum $\sim \nu^{-\alpha}$ with spectral indices α from 0.0 to 0.3. The origin of this flat radio spectrum is still unclear as it requires a particle population with a very hard energy distribution which cannot be explained by current models.

We proposed that magnetic reconnection might be responsible for the in situ acceleration of particles in the nebula. We could show that the onset of a magnetic-field-aligned electric field inside the reconnection regions is capable to efficiently accelerate particles. With regard to PWNe, our results showed particle energy distributions that matched the distributions required to explain the very flat radio spectrum. In this context magnetic reconnection is produced by turbulent shear flows inside the nebula. The termination shock which represents the interaction region of the pulsar wind with the surrounding nebula, provides the large scale source of MHD turbulence. The energy that is released by the pulsar is transported by the wind, accumulates in the shock region and is redistributed to smaller scales by turbulence throughout the nebula. In the dissipative range the plasma locally allows for resistivity to set in, caused by microturbulent instabilities. This leads to the onset of magnetic reconnection and eventually to the acceleration of particles by parallel electric fields E_{\parallel} .

The steepening of the radio spectrum at locations of radio emitting filaments, as observed by Bandiera *et al.* (2002), could be reproduced in our simulations by a higher plasma particle density inside the filaments. The higher density leads to a decreased amplitude of the resistivity $\eta \approx m_e \omega_e / ne^2$, where $\omega_e = \sqrt{4\pi ne^2 / m_e}$ is the electron plasma frequency.

Our scenario is supported by several hybrid simulations that produced electrons

with power law energy distributions of $N(\gamma) = \gamma^{-s}$ with s ranging from 1.2 to 1.6. Such populations create power law synchrotron spectra with spectral index α being in the range 0.1 to 0.3 which perfectly fit the observed radio spectra. The hybrid simulations made use of a resistive compressible MHD code in combination with subsequent test particle simulations. These included the feedback of synchrotron radiation onto the particles' motion by introducing an additional term in the equation of motion that describes the losses by radiation. The synchrotron spectrum is obtained by integrating the proper spectral distributions for single particle emission and taking the individual pitch angles into account. The resulting pitch angle distributions of the non-thermal electrons showed a clear anisotropy, which is an expected effect as E_{\parallel} mainly enhances the component of the particles' momentum parallel to the magnetic field. Therefore, the calculated synchrotron spectra differ from the ones resulting from the standard synchrotron theory (section 3.1) which implies an isotropic pitch angle distribution.

The test particle approach surely is not as accurate as it would be preferable, but it is reasonable to assume that the feedback of the non-thermal synchrotron particles on the magnetic field is negligible as the magnetic and dynamic evolution of PWNe is dominated by the thermal plasma components. Several other simulations have shown that a thermal lepton and ion component is naturally produced by the termination shock (Gallant *et al.*, 1992; Hoshino *et al.*, 1992; Arons & Tavani, 1994). A self-consistent approach like in Particle-in-Cell Simulations would be much more desirable, however this imposes a great constraint on the size of the computational domain when performed in full 3D. The high Lorentz factors demand the use of very small simulation cells in order to cover the high energy radiation accurately, which enormously increases the computational effort. Hence, there is no way by current available computational power to simulate the presented turbulent problem in a fully self-consistent manner. This makes our hybrid approach a valuable tool to analyse large scale structures.

Our work was recently reviewed by Massaro *et al.* (2006) in the context of particle acceleration in blazars. They investigated the acceleration of particles by considering a statistical acceleration mechanism whose probability of acceleration depends on the particle energy. They verified that across sufficiently wide energy ranges, our spectra are represented well by a combination of a power law and a parabola with small curvature parameters. They concluded that the curvature probably depends on the distribution and size of the acceleration regions, thus our method might well be applied to other high energy astrophysical plasmas where turbulence is of importance.

Bibliography

- Ambrosiano, J., Matthaeus, W.H., Goldstein, M.L. & Plante, D. (1988). Test particle acceleration in turbulent reconnecting magnetic fields, *J. Geophys. Res.* **93**, 14383.
- Arons, J. (1992). Magnetospheric Structure and Emission Mechanics of Radio Pulsars, in *Proceedings of IAU Colloq. 128*, eds. Hankins, T.H., Rankin, J.M. & Gil, J.A., (Pedagogical Univ. Press, 1992), p. p.56.
- Arons, J., Tavani, M. (1994). Relativistic particle acceleration in Plerions, *Astrophys. J. Suppl. Series* **90**, 797.
- Arons, J. (1998). On the coupling of rotation powered pulsars to plerionic nebulae, *Mem. Soc. Astron. Ital.* **69**, 989.
- Atoyan, A.M. (1999). Radio spectrum of the Crab nebula as an evidence for fast initial spin of its pulsar, *Astron. Astrophys.* **346**, L49.
- Bandiera, R. (2002). Plerionic supernova remnants, *Mem. Soc. Astron. Ital.* **73**, 107.
- Bandiera, R., Neri, R. & Cesaroni, R. (2002). The Crab Nebula at 1.3 mm. Evidence for a new synchrotron component, *Astron. Astrophys.* **386**, 1044.
- Bentley, R.D. & Mariska, J.T. (eds.) (1996). *Magnetic Reconnection in the Solar Atmosphere*, Astron. Soc. Pacific Conf. Ser. **111**.
- Bietenholz, M.F. & Kronberg, P.P. (1992). Activity and radio spectral index variations near the center of the Crab nebula, *Astrophys. J.* **393**, 206.
- Bietenholz, M.F., Frail, D.A. & Hester, J.J. (2001). The Crab Nebula's Moving Wisps in Radio, *Astrophys. J.* **560**, 254.
- Birk, G.T. & Otto, A. (1997). Consequences of a resistive instability operating in the upper auroral ionosphere, *J. Atm. Terr. Phys.* **59**, 835.
- Birn, J., Thomsen, M.F., Borovsky, J.E., Reeves, G.D., McComas, D.J., Belian, R.D. & Hesse, M. (1998). Substorm electron injections: Geosynchronous observations and test particle simulations, *J. Geophys. Res.* **103**, 9235.

- Biskamp, D. (2000). *Magnetic Reconnection in Plasmas* (Cambridge University Press, Cambridge).
- Blackman, E.G. (1996). Reconnecting Magnetic Flux Tubes as a Source of In Situ Acceleration in Extragalactic Radio Sources, *Astrophys. J.* **456**, L87.
- Bolton, J.G., Stanley, G.J., Slee, O.B. (1949). Positions of three discrete sources of Galactic radio frequency radiation, *Nature* **164**, 191.
- Brogan, C.L., Gelfand, J.D., Gaensler, B.M., Kassim, N.E., Lazio, T.J.W. (2006). Discovery of 35 New Supernova Remnants in the Inner Galaxy, *Astrophys. J.* **639**, L25-L29.
- Bruhwyler, D.L. & Zweibel, E.G. (1992). Energy spectrum of particles accelerated near a magnetic X line, *J. Geophys. Res.* **97**, 10,825.
- Chevalier, R.A. & Gull, T.R. (1975). The outer structure of the Crab nebula, *Astrophys. J.* **200**, 399.
- Clark, D.H. *et al.* (1983). Three-dimensional structure of the Crab Nebula, *Mon. Not. Roy. Astron. Soc.* **204**, 415.
- Coroniti, F.V. (1990). Magnetically striped relativistic magnetohydrodynamic winds: The Crab nebula revisited, *Astrophys. J.* **349**, 538.
- Crusius-Wätzell, A. & Lesch, H. (1998). Relativistic electron beams in IDV blazars, *Astron. Astrophys.* **338**, 399.
- Crusius-Wätzell, A., Kunzl, T. & Lesch, H. (2001). Synchrotron Model for the Infrared, Optical, and X-Ray Emission of the Crab Pulsar, *Astrophys. J.* **546**, 401.
- Edwards, P.G., Giovannini, G., Cotton, W.D., Feretti, L., Fujisawa, K., Hirabayashi, H., Lara, L. & Venturi, T. (2000). A Spectral Index Map from VSOP Observations of Markarian 501, *Publ. Astron. Soc. Japan* **52**, 1015.
- Ellison, D.C., Jones, F.C. & Reynolds, S.P. (1990). First-order Fermi particle acceleration by relativistic shocks, *Astrophys. J.* **360**, 702.
- Elsasser, W.M. (1950). The Hydromagnetic Equations, *Phys. Rev.* **79**, 183.
- Fleishman, G.D. & Bietenholz, M.F. (2007). Diffusive synchrotron radioation from pulsar wind nebulae, *Mon. Not. Roy. Astron. Soc.* **376**, 625.
- Fulbright, M.S. & Reynolds, S.P. (1990). Bipolar Supernova Remnants and the Obliquity Dependence of Shock Acceleration, *Astrophys. J.* **357**, 591-601.
- Furth, H.P., Killeen, J. & Rosenbluth, M.N. (1963). Finite-resistivity instabilities of

- a sheet pinch, *Phys. Fluids* **6**, 459.
- Gaensler, B.M. & Frail, D.A. (2000). A large age for the pulsar B1757-24 from an upper limit on its proper motion, *Nature* **406**, 158-160.
- Gaensler, B.M. (2000). Perspectives on Radio Astronomy: Science with Large Antenna Arrays, in *Proceedings of the Conference held at the Royal Netherlands Academy of Arts and Sciences in Amsterdam on 7-9 April 1999*, eds. van Haarlem, M.P., (ASTRON, Dwingeloo), p. p.271.
- Gaidos, J.A., Akerlof, C.W., Biller, S.D. *et al.* (1996). Very Rapid and Energetic Bursts of TeV Photons from the Active Galaxy Markarian 421, *Nature* **383**, 319.
- Gallant, Y.A., Hoshino, M., Langdon, A.B., Arons, J. & Max, C.E. (1992). Relativistic perpendicular shocks in electron-positron plasmas, *Astrophys. J.* **391**, 73.
- Gallant, Y.A., Arons, J. (1994). Structure of relativistic shocks in pulsar winds: A model of the wisps in the Crab Nebula, *Astrophys. J.* **435**, 230.
- Ghisellini, G. (1999). Blazars: Recent Developments, in *BL Lac Phenomena*, eds. Takalo, L.O. & Sillanpää, A., *Astron. Soc. Pacific* **159**, 311.
- Goldreich, P. & Julian, W.H. (1969). Pulsar Electrodynamics, *Astrophys. J.* **157**, 869.
- Green, D.A. (1991). Limitations imposed on statistical studies of Galactic supernova remnants by observational selection effects, *Publ. Astron. Soc. Pacific* **103**, 209.
- Green, D.A., Scheuer, P.A.G. (1992). Upper limits on the infrared flux density of the 'filled-centre' supernova remnant 3C58, *Mon. Not. Roy. Astron. Soc.* **258**, 833.
- Green, D.A., Tuffs, R.J. & Popescu, C.C. (2004). Far-infrared and submillimetre observations of the Crab nebula, *Mon. Not. Roy. Astron. Soc.* **355**, 1315.
- Green, D.A. (2004). Galactic supernova remnants: an updated catalogue and some statistics, *Bull. Astron. Soc. India* **32**, 335-370.
- Harris, E.G. (1962). On a plasma sheath separating regions of oppositely-directed magnetic field, *Nuovo Cimento* **23**, 115.
- Hester, J.J. *et al.* (1996). WFPC2 Studies of the Crab Nebula. III. Magnetic Rayleigh-Taylor Instabilities and the Origin of the Filaments, *Astrophys. J.* **456**, 225.
- Horiuchi, R. & Sato, T. (1997). Particle simulation study of collisionless driven

- reconnection in a sheared magnetic field, *Phys. Plasmas* **4**, 277.
- Hoshino, M., Arons, J., Gallant, Y.A., Langdon, A.B. (1992). Relativistic magnetosonic shock waves in synchrotron sources: Shock structure and nonthermal acceleration of positrons, *Astrophys. J.* **390**, 454.
- Hussain, A.K.M.F. (1983). Coherent structures - Reality and myth, *Phys. Fluids* **26**, 2813.
- Hussain, A.K.M.F. (1986). Coherent structures and turbulence, *J. Fluid Mech.* **173**, 303.
- Iroshnikov, P. (1963). Turbulence of a conducting fluid in a strong magnetic field, *Sov. Astron.* **7**, 566.
- Jun, Byung-Il, Jones, T.W. (1999). Radio Emission from a Young Supernova Remnant Interacting with an Interstellar Cloud: Magnetohydrodynamic Simulation with Relativistic Electrons, *Astrophys. J.* **511**, 774-791.
- Kennel, C.F. & Coroniti, F.V. (1984a). Confinement of the Crab pulsar's wind by its supernova remnant, *Astrophys. J.* **283**, 694.
- Kennel, C.F., Coroniti, F.V. (1984b). Magnetohydrodynamic model of Crab nebula radiation, *Astrophys. J.* **283**, 710.
- Kirk, J.G., Skjæraasen, O. (2003). Dissipation in Poynting-flux-dominated flows: The σ -problem of the Crab pulsar wind, *Astrophys. J.* **591**, 366.
- Kliem, B. (1994). Particle orbits, trapping, and acceleration in a filamentary current sheet model, *Astrophys. J. Supp.* **90**, 719.
- Kolmogorov, A.N. (1941). The Local Structure of Turbulence in Incompressible Viscous Fluid for Very Large Reynolds Numbers, *Proc. Roy. Soc. London Ser. A* **434**, 9, reprinted in 1991.
- Kraichnan, R.H. (1959). The structure of isotropic turbulence at very high Reynolds numbers, *J. Fluid Mech.* **5**, 497.
- Kraichnan, R.H. (1965). Inertial-Range Spectrum of Hydromagnetic Turbulence, *Phys. Fluids* **8**, 1385.
- Kronberg, P.P., Lesch, H., Ortiz, P.F., Bietenholz, M.F. (1993). The Crab Nebula's Cosmic-Ray Acceleration Zone Revealed, *Astrophys. J.* **416**, 251.
- Lampland, C.O. (1921). Observed Changes in the Structure of the "Crab" Nebula (N. G. C. 1952), *Publ. Astron. Soc. Pacific* **33**, 79.

-
- Lazarian, A., Pogosyan, D. & Esquivel, A. (2002). Quest for HI Turbulence Statistics: New Techniques, in *Seeing through the dust*, eds. Taylor, R., Landecker, T. & Willis, A., (ASP Conference Proceedings, San Francisco), p. 276.
- Landau, L. D., Lifshitz, E. M. (1951). *The Classical Theory of Fields* (Addison-Wesley, Reading MA).
- Lesch, H. & Birk, G.T. (1997). Particle acceleration by magnetic field-aligned electric fields in active galactic nuclei, *Astron. Astrophys.* **324**, 461.
- Lesch, H. & Birk, G.T. (1998). On the Origin of Extended Nonthermal Optical Emission in Extragalactic Jets, *Astrophys. J.* **499**, 167.
- Lesch, H. (2000). Radiation and Reconnection in Active Galactic Nuclei, in *Proceedings of the 1999 Enrico-Fermi-School on Plasma Astrophysics*, eds. Coppi, B., B. Ferrari, A. & Sinodi, E., (IOS Press, Amsterdam), p. 395.
- Li, Z., Wheeler, J.C., Bash, F. & Jefferys, W.H. (1991). A Statistical Study of the Correlation of Galactic Supernova Remnants, *Astrophys. J.* **378**, 93-105.
- Lin, C.S. & Hoffmann, R.A. (1979). Characteristics of the inverted-V event, *J. Geophys. Res.* **84**, 1514.
- Litvinenko, Y.E. (1996). Particle Acceleration in Reconnecting Current Sheets with a Nonzero Magnetic Field, *Astrophys. J.* **462**, 997.
- Litvinenko, Y.E. (1997). Interpretation of particle acceleration in a simulation study of collisionless reconnection, *Phys. Plasmas* **4**, 3439.
- Lyubarsky, Y. & Kirk, J.G. (2001). Reconnection in a striped pulsar wind, *Astrophys. J.* **547**, 437.
- Lyubarsky, Y.E. (2003). The termination shock in a striped pulsar wind, *Mon. Not. Roy. Astron. Soc.* **345**, 153.
- Manchester, R.N., Kaspi, V.M., Johnston, S., Lyne, A.G. & D'Amico, N.D. (1991). PSR 1758-24 and G5.4-1.2, a remarkable pulsar-supernova remnant association, *Mon. Not. Roy. Astron. Soc.* **253**, 7p-10p.
- Massaro, E., Tramacere, A., Perri, M., Giommi, P. & Tosti, G. (2006). Log-parabolic spectra and particle acceleration in blazars, *Astron. Astrophys.* **448**, 861.
- Melrose, D.B. (1994). Kinetic Plasma Physics, in *Plasma Astrophysics*, eds. Benz, A.O. & Courvoisier, T.J.-L., (Springer, Berlin, New York), p. 113.
- Michel, F.C. (1969). Acceleration of relativistic particles in the Crab nebula, *Astrophys. J.* **157**, 1183.

- Moses, W., Finn, J.M. & Ling, K.M. (1993). Plasma heating by collisionless magnetic reconnection - Analysis and computation, *J. Geophys. Res.* **98**, 4013.
- Nodes, C., Birk, G.T., Lesch, H. & Schopper, R. (2003). Particle acceleration in three-dimensional tearing configurations, *Phys. Plasmas* **10**, 835.
- Nodes, C., Birk, G.T., Gritschneider, M. & Lesch, H. (2004). Radio emission and particle acceleration in plerionic supernova remnants, *Astron. Astrophys.* **423**, 13.
- Otto, A. (1990). 3D resistive MHD computations of magnetospheric physics, *Comput. Phys. Comm.* **59**, 185.
- Otto, A. & Birk, G.T. (1993). Formation of thin auroral arcs by current striation, *Geophys. Res. Lett.* **20**, 2833.
- Orszag, S.A. (1977). Lectures on the Statistical Theory of Turbulence, in *Fluid Dynamics*, eds. Balian, R. & Peube, J.-L., (Gordon and Breach, London), p. 236. (summer school lectures given at grenoble university, 1973)
- Orszag, S. A., Tang, C.-M. (1979). Small-scale structure of two-dimensional magneto-hydrodynamic turbulence, *J. Fluid Mech.* **90**, 129.
- Priest, E.R. & Forbes, T. (2000). The magnetic nature of solar flares, *Astron. Astrophys. Rev.* **10**, 313.
- Priest, E.R. & Forbes, T. (2000). *Magnetic reconnection: MHD theory and applications* (Cambridge University Press, New York).
- Rees, M.J., Gunn, J.E. (1974). The origin of the magnetic field and relativistic particles in the Crab nebula, *Mon. Not. Roy. Astron. Soc.* **167**, 1.
- Reynolds, S.P. (1988). Filamentary structure in Crab-like supernova remnants, *Astrophys. J.* **327**, 853.
- Rybicki, G. B., Lightman, A. P. (1979). *Radiative Processes in Astrophysics* (Wiley, New York), ch. 6.2.
- Salvati, M., Bandiera, R., Pacini, F., Woltjer, L. (1998). Evolution of plerions: are there two kinds?, *Mem. Soc. Astron. Ital.* **69**, 1023.
- Scargle, J.D. (1969). Activity in the Crab Nebula, *Astrophys. J.* **156**, 401.
- Schopper, R., Birk, G.T. & Lesch, H. (1999). Particle acceleration in three-dimensional reconnection regions: A new test particle approach, *Phys. Plasmas* **6**, 4318.

- Sedov, L. I. (1946). Propagation of strong shock waves, *Prikl. Mat. Mekh.* **10(2)**, 241.
- Simon, M. &, Axford, W.I. (1967). Thermal Instability Resulting from Synchrotron Radiation, *Astrophys. J.* **150**, 105.
- Swinbank, E. (1980). A study of the Crab Nebula - II. Radio emission from the filaments, *Mon. Not. Roy. Astron. Soc.* **193**, 451.
- Taylor, G. I. (1950). The formation of a blast wave by a very intense explosion, *Proc. Roy. Soc. A* **201**, 159.
- Toor, A., Seward, F. D. (1974). The Crab Nebula as a calibration source for X-ray astronomy, *Astron. J.* **79**, 995.
- Tosti, G., Fiorucci, M., Luciani, M. *et al.* (1998). Radio, optical and photopolarimetric observations of Markarian 421 around the great 1996-97 outburst, *Astron. Astrophys.* **339**, 41.
- Trimble, V. (1968). Motions and Structure of the Filamentary Envelope of the Crab Nebula, *Astron. J.* **73**, 535.
- Vasyliunas, V.M. (1975). Theoretical models of magnetic field line merging. I, *Geophys. Space Phys.* **13**, 303.
- Velusamy, T., Roshi, D. & Venugopal, V.R. (1992). Multifrequency VLY observations of the Crab Nebula at different epochs: expansion and radio spectra of filaments, *Mon. Not. Roy. Astron. Soc.* **255**, 210.
- Vekstein, G.E. & Browning, P.K. (1997). Electric-drift generated trajectories and particle acceleration in collisionless magnetic reconnection, *Phys. Plasmas* **4**, 2261.
- Verma, M.K. (1999). Mean magnetic field renormalization and Kolmogorov's energy spectrum in magnetohydrodynamic turbulence, *Phys. Plasmas* **6**, 1455.
- Wagner, J.S., Kan, J.R. & Akasofu, S.-I. (1979). Particle dynamics in the plasma sheet, *J. Geophys. Res.* **84**, 891.
- Wagner, J.S., Gray, P.C., Kan, J.R., Tajima, T. & Akasofu, S.-I. (1981). Particle dynamics in reconnection field configurations, *Planet. Space Sci.* **4**, 391.
- Weiler, K.W., Panagia, N. (1978). Are Crab-type Supernova Remnants (Plerions) Short-lived?, *Astron. Astrophys.* **70**, 419.
- Weiler, K.W., Shaver, P.A. (1978). Total Intensity and Polarization Structure of the Supernova Remnant G 74.9 + 1.2 at XX6,21, and 49 Centimeters, *Astron. As-*

trophys. **70**, 389.

Weiler, K.W. (1980). A correspondence between optical and radio emission in the Crab-type supernova remnant 3 C 58, *Astron. Astrophys.* **84**, 271.

Weiler, K.W. (1983). The Crab Nebula is not alone!, *Observatory* **103**, 85-106.

Wheeler, J.C. (2004). Three-dimensional explosions, in *Cosmic explosions in three dimensions: asymmetries in supernovae and gamma-ray bursts.*, eds. Hoflich, P., Kumar, P. & Wheeler, J.C., (Cambridge University Press, Cambridge), p. 373.

Woltjer, L. (1972). Supernova Remnants, *Ann. Rev. AA* **10**, 129.

Woltjer, L., Salvati, M., Pacini, F., Bandiera, R. (1997). Non Crab-like Plerions?, *Astron. Astrophys.* **325**, 295.

Danksagung

Mein größter Dank gilt Harald Lesch für die Betreuung meiner Arbeit. Bei einer theoretischen Arbeit, wie bei der vorliegenden, gerät man allzuoft in Gefahr, sich in mathematischen Problemen zu verstricken oder in numerischen Details zu verlieren. Deshalb war ich immer sehr dankbar für Haralds Kommentare und Anregungen, die halfen, den physikalischen Aspekt nicht völlig aus den Augen zu verlieren. Neben seiner fachlichen Unterstützung bedanke ich mich für die äußerst angenehme und humorvolle Atmosphäre, die er in unserer Gruppe schaffte. Nicht zuletzt danke ich ihm für die Geduld, die er zuletzt aufbringen musste.

Eine weitere wichtige Person im Verlauf meiner Arbeit war Guido Birk, der ein unglaubliches Talent hat, komplizierteste Zusammenhänge einfach zu erklären. Gerade in der Schlussphase hat er mich durch viele motivierende Gespräche darin bestätigt, auf dem richtigen Weg zu sein.

Großer Dank gilt auch meinem Bürokollegen Stefan Lieb für gegenseitige Motivation und gute Hinweise bei dem Erstellen der vorliegenden Arbeit. Weiterhin möchte ich meinen ehemaligen "Mitschülern" an der IMPRS, Claus Jaroschek und Tamara Repolust, für eine aufregende und äußerst angenehme Zeit danken. Auch meinen Bürokollegen an der USM, Rüdiger Schopper, Christian Konz, Thomas Kunzl und Matthias Gritschneider gilt mein Dank.

Für das Korrekturlesen möchte ich meiner Schwägerin Susi Schropp danken, die trotz genügend eigener Arbeit Zeit für das Korrigieren aufbrachte.

Oliver Kostinek und Andreas Schön bei der Firma 3points Software möchte ich für die kurzfristige Einrichtung des "Chair of Physics" danken, eines kleinen Büros, in dem ich große Teile meiner Arbeit verfasste.

Zu guter Letzt bin ich meiner Frau Katharina unermesslich dankbar, mich während des Aufschreibens meiner Arbeit moralisch unterstützt und ertragen zu haben.